# Graphene Quantum Capacitance Varactors

A Dissertation
SUBMITTED TO THE FACULTY OF
UNIVERSITY OF MINNESOTA
BY

Mona Abdulkhaleg Ebrish

IN PARTIAL FULFILLMENT OF THE REQUIREMENTS
FOR THE DEGREE OF
DOCTOR OF PHILOSOPHY

Adviser: Steven J. Koester

March, 2015

# Acknowledgements

First of all, praise to Allah, who has given me countless blessings and helped me stay strong and focused.

I would like to extend my deepest gratitude to my advisor Steven Koester whose guidance, support, and kindness during the course of this work was invaluable to me. I am privileged to be his first PhD graduate. I have learned from him almost everything: cleaning a wafer, taking a good set of measurements, temperature measurements, manuscript writing, and preparing presentations.

Special thanks to Prof. Paul Ruden. He has inspired me and many others to enjoy semiconductors physics and fundamentals. Deriving equations had never been fun until I took his class.

I am grateful to the MNC staff: Kevin Roberts, Tony Whipple, Mark Fisher, Terry Brough, Rich Macy, Lage von Dissen, Paul Kimani, Bashir Jama, and Sherri Quick for their training, assistance, and friendship.

I would like to thank Professors: Beth Stadler and Rhonda R. Franklin for their support and guidance. They always found the time to discuss and advise me on several things related to my research and time management.

I would like to thank Beth Stadler, Mo Li, and Phil Bulhamn for agreeing to be on my committee and reviewing my thesis.

I would like to thank the ECE and U of M staff, especially Linda Jagerson and Gabi Schmiegel. Thanks to them I never had to worry about any administrative issues. They were a great help in to accommodating my forgetfulness and last minute urgencies. I would like to especially thank librarian Jan Fransen for helping me with my thesis formatting.

I would like to thank all my friends who made the Twin Cities a happy home for me, especially my studying buddy Forrest, my best friend, and all my new diverse family members at Masjid Al-Iman.

I would like to express my deepest gratitude to the members in my family overseas who supported me along this journey, and did what they can within their means to make me feel loved and missed.

Last but not least, I would like to thank AMIDEAST and the Fulbright programs for giving me the fellowship that started this journey. They gave me not just financial support, but provided a great opportunity for personal growth, and introduced me to a wonderful group of intellectual new friends. The Fulbright program and fellowship did not just give me the chance to obtain a master's degree from one of the best universities in the states, but also included me in one big diverse family.

*This dissertation is dedicated to the memories of my Father (Abdulkhaleg), Uncle (Hamid), and Grandmother (Anisa)*

*And to all my teachers*

# Graphene Quantum Capacitance Varactors

# by Mona Ebrish


## Abstract

Graphene is an attractive material for sensing applications due to its large surface-to-volume ratio and high electrical conductivity. The concentration-dependent density of states in graphene allows the capacitance in metal-oxide-graphene structures to be tunable with carrier concentration. This feature allows graphene to act as a variable capacitor (varactor). These devices have a multitude of applications, particularly for biosensing, where the small size and wireless readout are attractive features for in vivo usage. The operation of multi-finger graphene quantum capacitance varactors fabricated using a planarized local bottom gate electrode, $HfO_2$ gate dielectric, is described. The devices show a capacitance tuning range of 1.6:1 at room-temperature, over a voltage range of ±2 V.

A characterization methodology was developed to serves as a diagnostic process to ascertain graphene varactor limitations and capabilities. Since functionalization of graphene is needed to sense variety of target analytes, the material and electrical properties of graphene functionalized with glucose oxidase (GOx) was studied. The device characteristics were explored at each step of functionalization with the end goal of realizing wireless graphene glucose sensors. Finally the effect of water vapor was explored, with a demonstration of stable and reproducible wireless humidity sensor.

# Table of Contents

# Chapter 1
# Introduction

*"Mother of all graphitic forms, Graphene is a 2D building material for carbon materials of all other dimensionalities. It can be wrapped up into 0D buckyballs, rolled into 1D nanotubes or stacked into 3D" A. K. Geim. Nat. Mater, vol. 6, no. 2007, 3, pp. 183–91.*

## 1.1 Graphene

### *1.1.1 History*

Graphene is a two-dimensional (2D) $sp^2$-bonded allotrope of carbon. It is the first 2D material that has been shown to be stable under ambient conditions. Graphene is not a new material; it has been studied theoretically for years as the base material for graphite and graphitic allotropes of carbon. Before the actual isolation of graphene flakes, graphene was theoretically predicated. The first work on this system was done by P. R Wallace in 1947 [1]. In this paper, a nearest neighbor, tight-binding model was used to determine an analytical expression for the electronic band structure pertaining to the π-bonds of monolayer graphite. In subsequent years from the work of Wallace, single-layer graphene was considered to be thermodynamically unstable for sizes <24000 atoms (or <20 nm); after that, it was expected to start forming islands of carbon which is by definition 3D material [2], [3].

The first intensive study of isolated graphene flakes, exfoliated from bulk crystals, was performed by K. Novoselov, *et al*., and this work showed unambiguously that graphene was indeed stable in a monolayer form. The basic field-effect was demonstrated, as well as confirming the monolayer material thickness using optical absorption contrast and

atomic force microscopy (AFM) [4], [5]. Figure 1-1 shows the first flake of a few layers of graphene optically and by an AFM scan on Si/$SiO_2$ substrate. This figure is taken from reference [4].

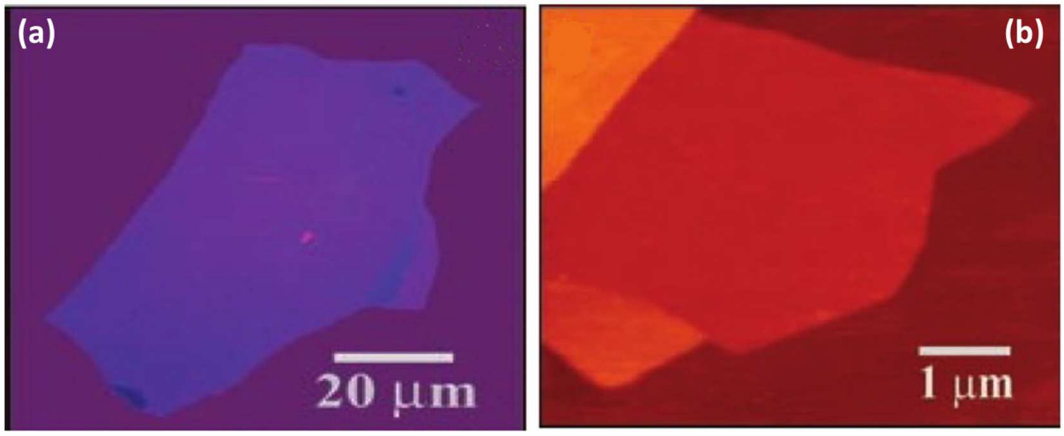


Figure 1-1: (a) few-layer graphene flake observed by an optical image, (b) an AFM image of single- and multi-layer graphene on a $SiO_2$/Si substrate [4].

Since the pioneering work of Geim and Novosolev, graphene has been studied intensively by numerous groups around the world. All the early experiments have proven that graphene is an interesting material for electronic and spintronics device applications [3], [6], [7]. Graphene has a very unique band structure, not just because it is a gapless semiconductor, but for the linear energy dispersion in the k-space or in reciprocal lattice space near the neutrality point (NP). At this point the conduction cone and the valence cone meet. This unusual energy structure opens the door for many interesting quantum mechanical phenomena to be studied such as Klein tunneling. As expected the electrons near the neutrality point or so called the Dirac point can be considered massless fermions and that sets a new class for a material in which electrons approach the speed of light in their motion. In graphene electrons moves in Fermi velocity which is ~ $10^6$ m/sec. Because of this speed and the crystalline structure, theoretically the mobility in graphene can reach 100,000 $cm^2$/V.sec [2], [3]. This theoretical limit assumes no scattering, which can be achieved once the large crystalline sheets of graphene can be synthesized. Though

other materials such as InSb have very high mobility, it decreases drastically once they are doped. Graphene preserves its high mobility even with the carrier concentration higher than $10^{12}$. This is the truly exceptional feature of the graphene mobility, which is less sensitive to electro static doping as well as chemical doping.

### 1.1.2 Energy band structure

Graphene crystal lattice is a honeycomb with two atoms in its unit cell. Each carbon atom has three bonds, those bonds are superposition of $p_x$,$p_y$ and $s$ orbitals, which hybridize to form the sigma bonds (σ). The strength of the σ-bonds defines the mechanical properties of graphene. Furthermore, the $p_z$ orbitals hybridize with each other to form the π-bonds which are the most relevant for graphene's electronic properties. Though the π-electrons are out of plane (vertically), they are responsible for all the interesting graphene's electrical properties. Since graphene lattice structure is a hexagon (honeycomb) as in Figure 1-2, both Bravis lattice and the reciprocal lattice are also hexagon. The first Brillouin zone of graphene is shown in Figure 1-2.

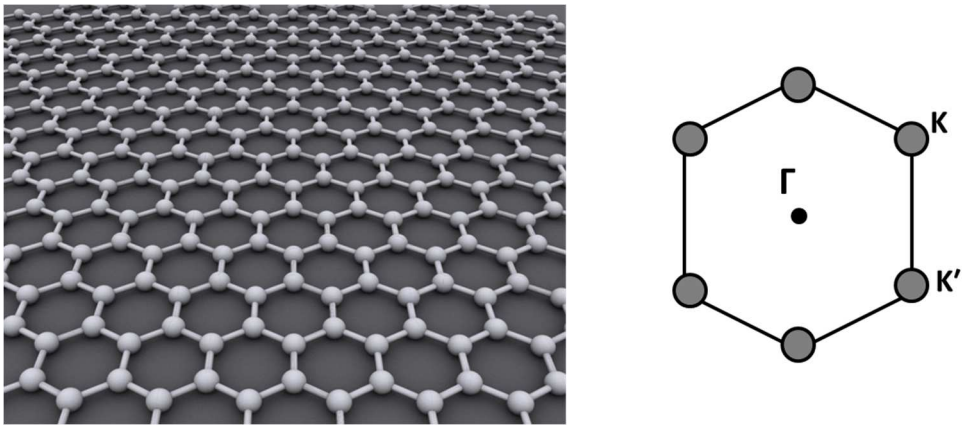


Figure 1-2: (Left) graphene honeycomb crystal lattice (source: Wiki-commons), (Right) graphene first Brillouin zone with the center (Γ) and the corners K, K′ of different symmetry.

In the reciprocal lattice the K and K′ are not exactly equivalent, they have different symmetry; therefore one can't use one of the primitive translation vector to move from K to K′. The energy band structure in Figure 1-3 from reference [8], was calculated with both *ab intio* and nearest-neighbor tight-binding methods for the first Brillouin zone. Figure 1-3 shows only π-bonds without considering the σ-bonds. The zero line is not a band, it was marked to distinguish the upper bands which are the empty state conduction bands from the lower full valence bands [8]. At the K point where the upper valance band touches the lowest conduction band, which indicates the absence of energy gap in graphene. By focusing more on the K point where the two bands touch, one might also notice that there is no curvature, in other words there is no second derivative for energy to respect the k; therefore this material has zero effective mass. Some publications refer to the graphene-electrons as massless Dirac fermions [9].

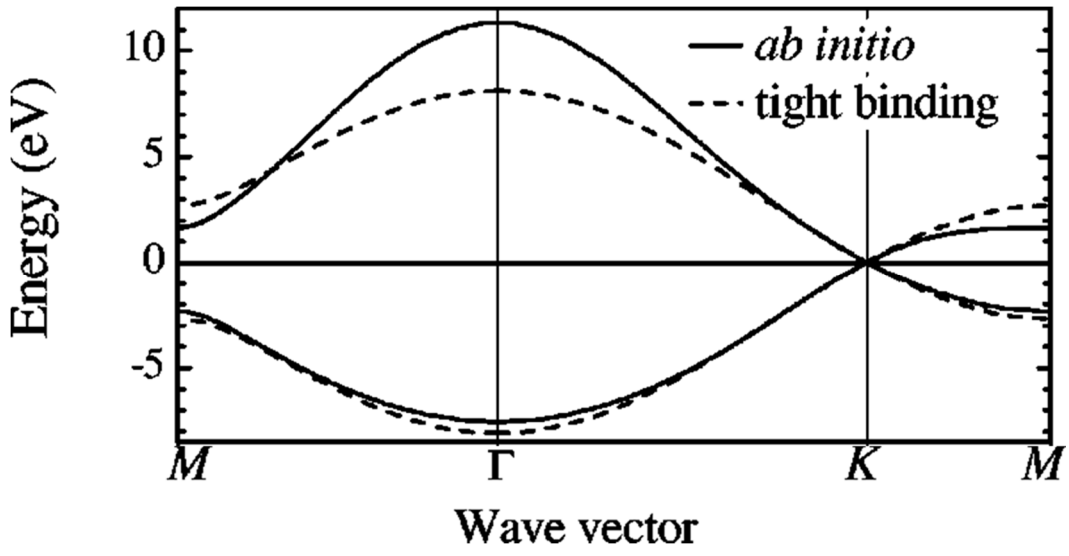


Figure 1-3: *ab initio* and nearest-neighbor tight-binding dispersions of graphene. The converged ab initio calculation of the graphene π and π* electronic bands is shown by the full lines. The dashed lines represent the tight-binding dispersion [8].

Graphene has many unique electronic properties such as carrier ambipolar nature, zero band gap, and linear energy bands dispersion. The absence of a band gap is a hurdle that

prevents graphene from contributing to digital electronics [10][3]. However, the linear energy-k dispersion around the K point provides a different set of unique properties that can be advantageous in optic, spin and electronic applications. The linear dispersion can be expressed as

$$E(k) = \pm\hbar v_F|k|\,, \qquad 1\text{-}1$$

where $\hbar$ is reduced Planck constant, $v_F$ is the Fermi velocity for the carriers ($10^6$ m/sec), (±) are for the conduction and valence bands respectively, and $|k|$ is the wave vector in the x-y plane in a graphene sheet where the point at k=0 is defined as Dirac point [11]. The energy linear dispersion in k-space is the very reason the density of states (DOS) vanishes in pristine graphene at the Dirac point (k=0) [12]–[14] as shown Figure 1-4. The zero states at the Dirac point leads to a small quantum capacitance in the vicinity of the Dirac point, and even smaller quantum capacitance at the Dirac point. More on observing the quantum capacitance in graphene will be explained in the coming section.

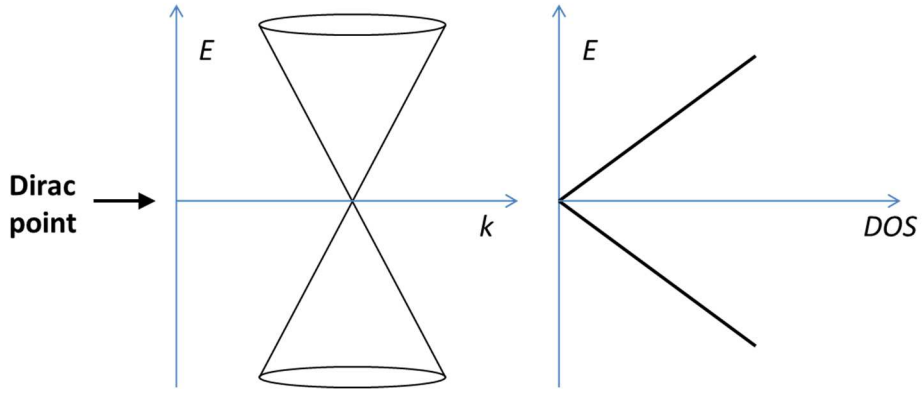


Figure 1-4: Plot of the graphene energy cone around the K point and the resulting DOS around the same point.

### 1.1.3 Quantum capacitance in graphene

All materials have an extra capacitance which reduces the overall capacitance of the system because it is in series with the geometric capacitance [15], but in most cases it does not cause much change due to the fact that it has a large value within the bias window of most systems. The quantum capacitance ($C_q$) effect is especially prominent in graphene due to its very low density states, as shown in Figure 1-5. This property has been studied by numerous groups [11]–[13], [16]–[21]. A small change in the Fermi level causes a significant change in the quantum capacitance because the quantum capacitance is defined as the variation in the charge relative to the chemical potential (Fermi-level) as in

$$C_q = \frac{dQ}{dE_F}, \qquad 1\text{-}2$$

where $Q$ is the total charge in the system. As the Fermi level moves towards Dirac point, the quantum capacitance becomes very small and it dominates the system. Though the small quantum capacitance is not very desirable in the CMOS world, it gives graphene an advantage in sensing applications [22], [23]. The power of the Fermi level ease of moving is not only limited to applying a bias. Fermi level in graphene can be moved by chemically doping the graphene. This doping does not have to be permanent, temporary doping is possible as long as the doping species do not form a strong bond (covalent or ionic) with the graphene. This topic will be discussed in detail later. Quantum capacitance can be tuned in graphene by tuning Fermi-level. This property has been studied in several graphene field effect device configurations. The quantum capacitance in graphene have been observed in Si back gated FET configuration [13], top gated FET configuration [16]; while others have used scanning probe microscopy SPM [20], or an ionic liquid electrolytes [24].

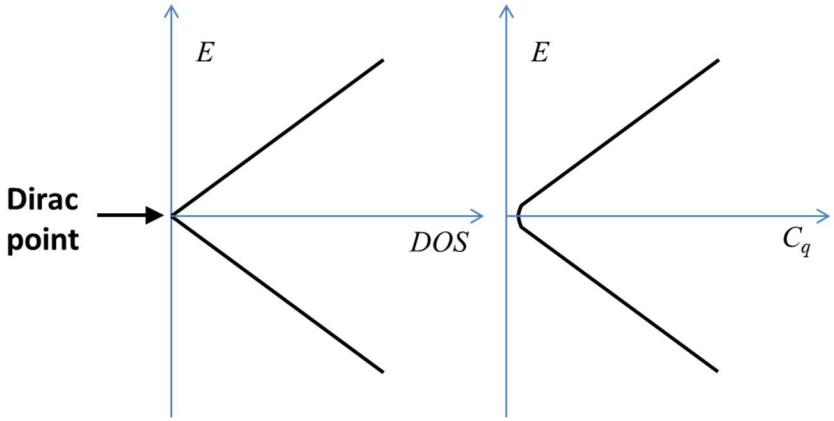


Figure 1-5: Plot of the graphene DOS versus energy at the K point and the resulting quantum capacitance at the same point.

### 1.1.4 Raman signature

Raman spectroscopy has been historically used to identify graphite materials, so it is intuitive to think of it as a tool to learn more about graphene. Before the vast use of Raman spectroscopy in the graphene community, atomic force microscopy (AFM) was the only way to identify single layer from few layers. AFM however, is not the perfect method for that task because of its inherent limitations. For example wrinkles or folds on the graphene surface can be interpreted incorrectly as multilayers [25].

Raman spectroscopy is a non-destructive method to learn more about the graphene. It is a very capable tool to see the graphene from a different angle and literally in a different light (wave length). The two carbon atoms in graphene's primitive unit cell (A and B) give rise to six phonon dispersion bands at the high symmetry ΓM and ΓK directions, those modes are a mix of longitudinal and transverse optical phonons (LO,TO) and longitudinal and transverse acoustic phonons (LA,TA) both in-plane and out-of-plane namely: LO, iTO, oTO, LA, iTA, and oTA. The phonon modes around the K point are especially important, since both D and 2D peaks are related to phonon modes in the vicinity of the K point as shown in Figure 1-6. The 2D-peak is also known as G′.

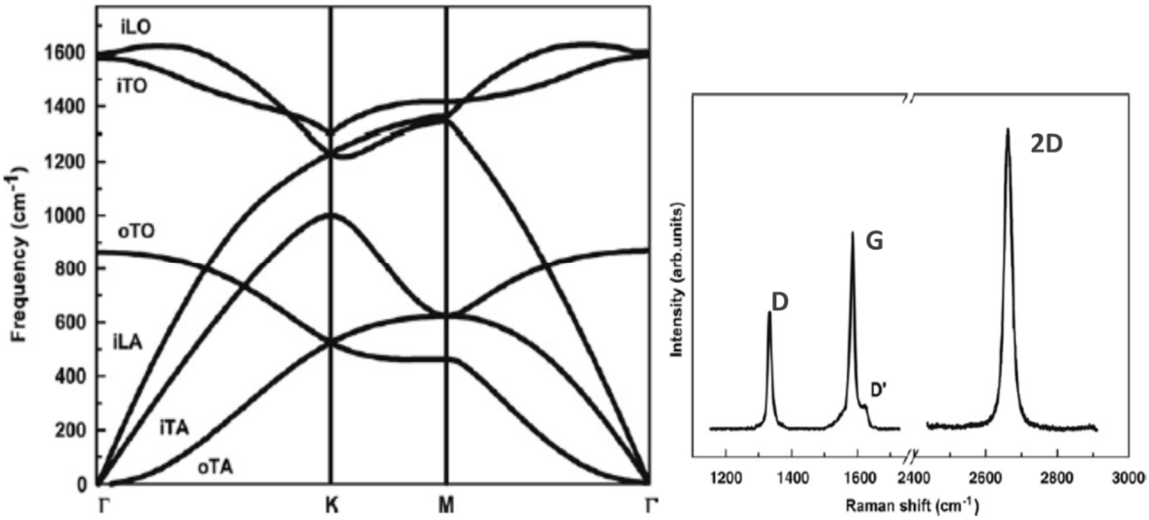


Figure 1-6: (Left) phonon dispersion in the graphene reciprocal lattice. (Right) Raman spectroscopy signal on a single layer graphene that corresponds to the phonon dispersion [25].

D-peak in graphene's Raman spectrum is a measure of defects. If the D-peak amplitude is too low or absent, it means that the graphene is either pristine or has a small number of defects. D-peak is at ~1380 $cm^{-1}$, and it is usually large at the edges because the non-satisfied un-covalent-bond acts as a defect site. And it is a result of TO phonon, intervalley scattering near the K-point, there must be a defect site for the D-peak to rise and its intensity does not change with the graphene number of layers, but rather to the amount of defects. Figure 1-7 explains the evolution of each peak in the graphene Raman signature, starting with inelastic scattering even for the G-peak. The G′ (2D ) is intervalley double resonance (DR) process that involves two elastic phonon scattering, unlike the D-peak which is also DR process, but involves one elastic scattering and one inelastic scattering from a defect site [25], [26].

The G-peak appears at ~1580 $cm^{-1}$, and its intensity and shape is almost the same in graphene and graphite, but it should be mentioned that in graphene the G-peak position is shifted to a higher wave length by 3-5 $cm^{-1}$. In bulk graphite the 2D peak, historically known as (G′), has two components and is about half or less the amplitude of the G-peak.

In monolayer graphene, however, the 2D peak is one sharp peak and it is twice or more the intensity of the G peak as shown in Figure 1-8(a). One can see that this feature is an easy way to distinguish monolayer from multilayer or bulk form of graphene [26]–[28].

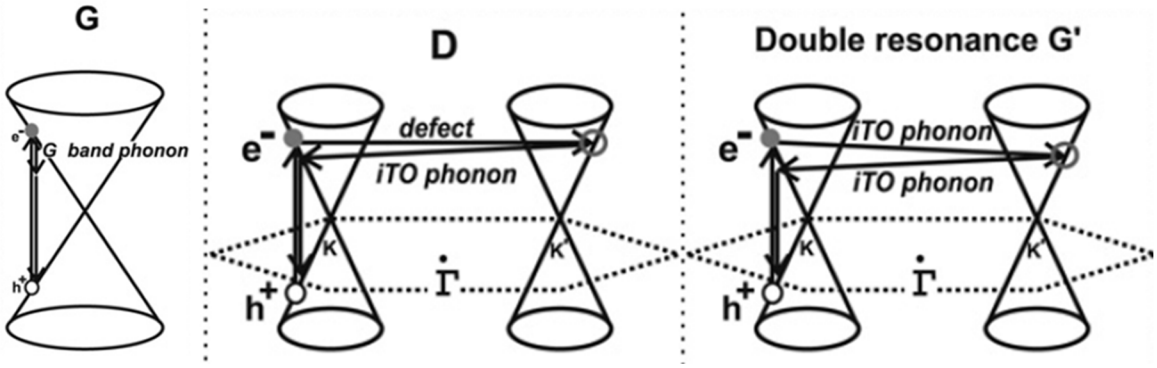


Figure 1-7: (Left) First-order G-band process; (Center) one-phonon second-order DR process for the D-band (intervalley process); (right) two-phonon second-order resonance Raman spectral processes for the double resonance G′ process [25].

Both the D and 2D (G′) peaks shifts up in frequency proportional to the laser (excitation) energy, as one can see in Figure 1-8 (b, c). Finally, Graphene has a unique Raman signal in which the features of its peaks, such as width, position and shape, can reveal several properties about the graphene, such as number of layers, level of defects and doping level [29].

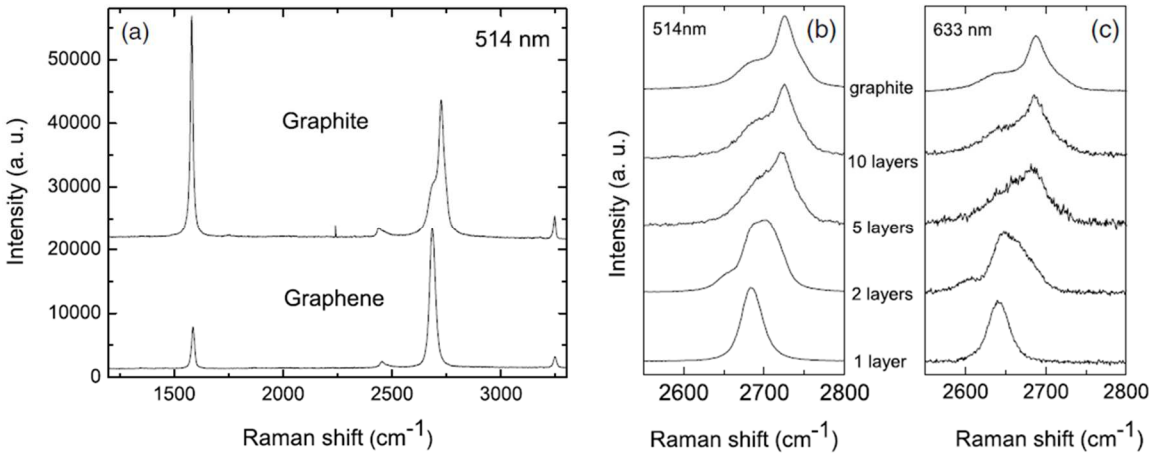


Figure 1-8: (a) Comparison of Raman spectra at 514 nm for bulk graphite and graphene (the 2D peak is scalled to fit in the comparison); (b) Evolution of the spectra at 514 nm with the number of layers. (c) Evolution of the Raman spectra at 633 nm with the number of layers [29].

### 1.1.5 Graphene growth

From 2004 until mid-2009, graphene films were mainly produced by exfoliating the bulk graphite with scotch tape. Though this method gives high quality graphene flakes, they are very small in size to make several devices using the same flake. The largest monolayer graphene flakes were few tens of microns. Furthermore, locating those flakes on the substrate is a tedious job. Some other groups had synthesized the graphene on SiC substrate by desorbing silicon from SiC single-crystal surfaces, which yields a multilayered graphene [30], [31]. Others utilized surface precipitation process of carbon in some transition metals. In all those cases the size of monolayer graphene was not very sufficient, and it was not possible to transfer the graphene successfully to another substrate [32], [33]. In mid-2009, the first paper on large area chemical vapor deposition (CVD) graphene was presented in Xuesong Li. et.al. [34]. Unlike epitaxial growth on SiC, CVD graphene provides large areas that can be transferred to any desired substrate by etching away the catalyst foil. In CVD graphene a metal foil such as copper or nickel can be used as a catalyst while the main gases to form the graphene material are hydrogen

and methane. Single layers of graphene can only be obtained on copper foil as the formation process does not terminate on nickel. To obtain a monolayer of CVD graphene, usually a copper foil with ~ 25μm thickness copper foil is annealed in a furnace to ~ 1000 ºC in low pressure, followed by flowing a mix of hydrogen and methane at low pressures [34]. Figure 1-9 shows an illustrative cartoon for a typical CVD graphene production system.

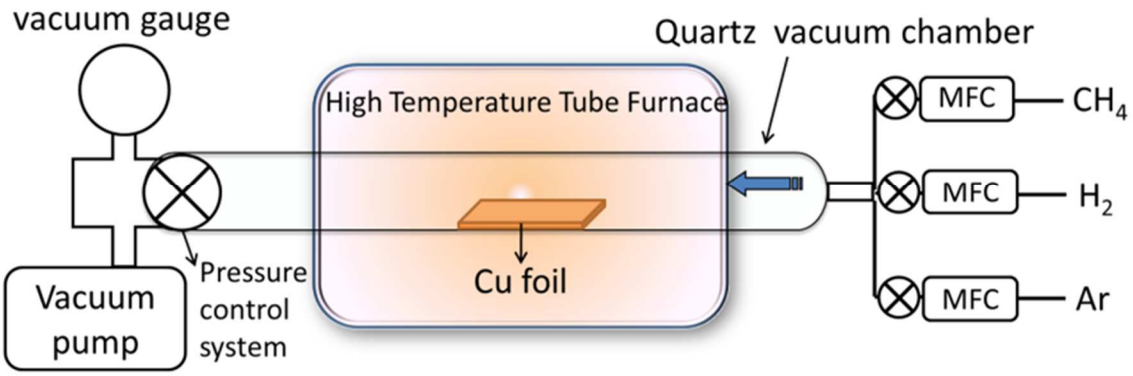


Figure 1-9: Schematic diagram of graphene CVD growth system, with three mass flow controllers (MFC) for methan, hydrogen and argon[1].

The sample then is cooled down. The cooling rate plays an important role for the quality of the grown graphene. Next, the graphene can be transferred to any substrate by wet etching the copper foil. $H_2$ to $CH_4$ ratio and the duration of the growth play a significant role in the quality of the graphene [35]–[37]. Though all the devices are made of CVD graphene on copper foil, this thesis does not address the CVD graphene growth procedure. Large-area synthesis of graphene is particularly desired for various practical applications.

[1] Designed by Brian Olmsted.

## 1.2 Graphene sensors

### 1.2.1 Resistive graphene sensors

One of the most promising areas for graphene is sensing applications. Graphene as a gapless semiconductor or semimetal has several challenges to be incorporated into the digital electronic world. The low dimensionality in graphene, however, provides large surface to volume ratio that makes it almost an ideal material for sensing applications. Furthermore, graphene's high mobility and inert nature can also be advantageous traits in sensing applications. In 2007, a paper by F. Schedin *et al*. showed the first change in non-functionalized graphene's free carrier concentration relative to various gases concentrations as shown in Figure 1-10 [38]. Despite the incomplete understating of the sensing mechanism, this paper has triggered a wave of publications that intensively studied graphene's response to various species [39]–[46]. The majority of those applications required functionalizing the graphene surface. Functionalization schemes can be covalent or non-covalent; in chapter five, one of the non-covalent schemes will studied in detail. Functionalizing graphene's surface is important due to its inert nature. The organic residuals on its surface can hinder the ability and consistency of sensing [47]. Aside from the sensing mechanism and sensitivity level, most if not all sensing applications for graphene are resistive based. The resistive based sensors depend on changing the conductivity in graphene as the concentration of the sensing analyte changes, which requires passing a current through the device to measure the change in the resistance. Passive wireless graphene based sensors cannot be achieved through resistance or conductance change [48], [49]. A key premise of this thesis is to utilize the change in capacitance that arises due to the quantum capacitance effect to realize a new type of sensor. This transduction technique has advantages over the resistive sensors described above because it could allow the realization of passive, wireless sensors. The

next section will address the realization and the advantages of quantum capacitance based sensors.

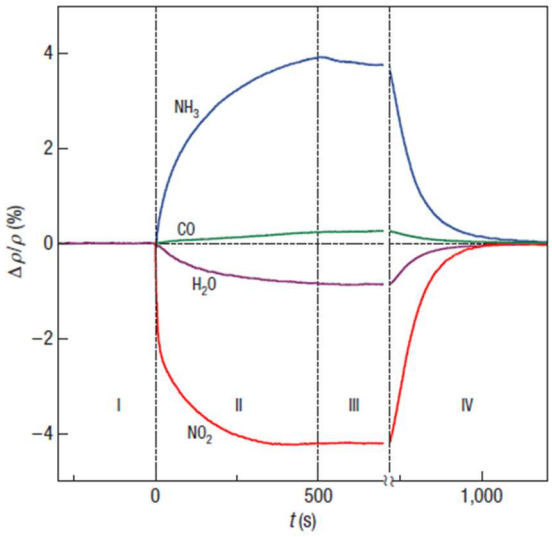


Figure 1-10: Changes in resistivity caused by graphene's exposure to various gases diluted in concentration to 1 ppm [38].

### 1.2.2 Quantum capacitance based sensors

In section 1.1.3 the quantum capacitance concept was introduced. Here however, the observation of quantum capacitance in simple two terminal devices is presented. Capacitance in a metal-oxide-graphene capacitor (MOG) is a series combination of oxide and quantum capacitances as shown in Figure 1-11. In reference [23], the first metal-oxide-graphene capacitor was proposed that could be utilized as the variable capacitor in a passive LC sensing circuit. The high mobility in graphene would enable high quality factors (Q) to be achieved. Such sensors have the potential to be much smaller (about 100 times smaller) than micro-electro-mechanical systems (MEMS) resonators based due to the larger capacitance per unit area. In addition to this prominent application, the quantum capacitance in the previously described structures can be utilized to probe fundamental properties of graphene [23], [50].

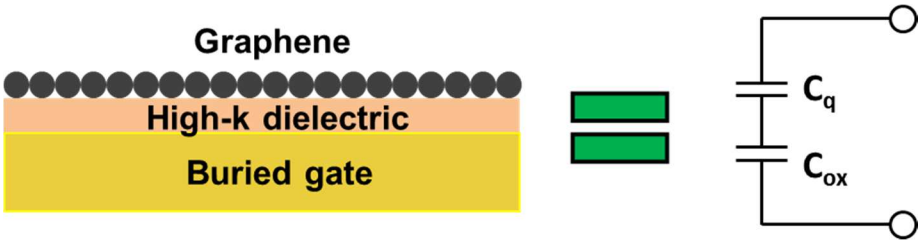


Figure 1-11: Cartoon shows the cross-sectional varactor structure and its equivalent circuit.

The idea of probing the graphene electronic properties through the MOG structures comes from the strong relationship between the quantum capacitance and the density of states [13], [14], [50]. Furthermore, the MOG structures can be utilized to function as variable capacitors in which surface adsorbed molecules can modulate the quantum capacitance effect in graphene. If incorporated in capacitor geometry (with thin high-k dielectric) and integrated with an inductor, then graphene can enable a new type of wireless sensor.

The detected molecules will cause a change to the overall capacitance of the device through changing the graphene quantum capacitance, therefore moving Fermi-level. This change in the total capacitance of the device will cause a change in the resonance frequency. Figure 1-12 depicts the basic idea of the passive wireless graphene sensor. In chapter 6 more details on this particular subject will be discussed.

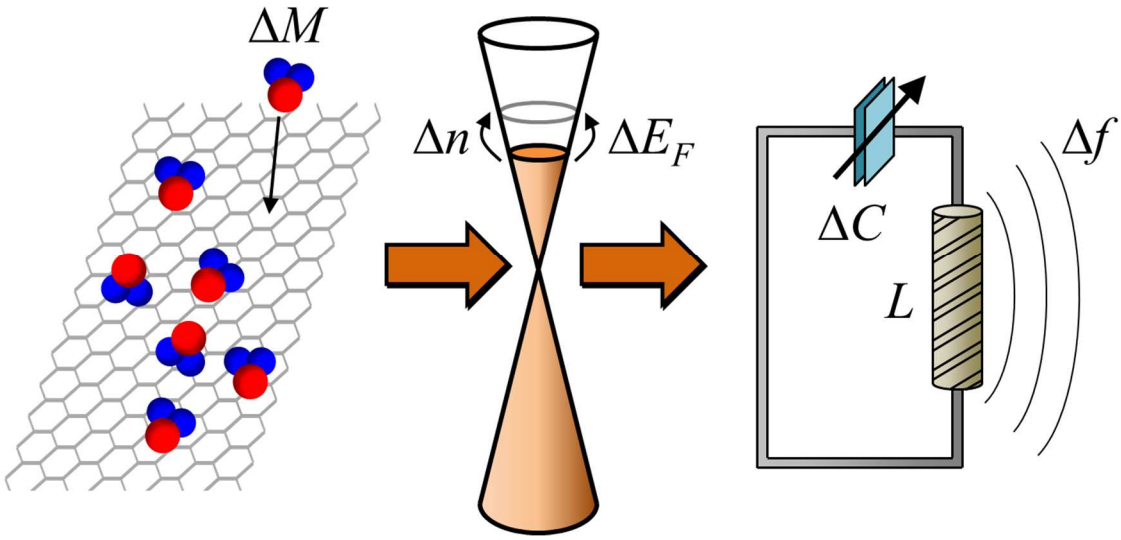


Figure 1-12: Illustrative cartoon for graphene varactor wireless sensing mechanism.

## 1.3 Outline of chapters

This thesis focuses on the graphene based variable capacitors (varactors). This dissertation is organized into the following chapters; each contains a significant portion of the research work. The contribution from others are acknowledged in this section

- Chapter 2 discusses in detail the fabrication process for the varactors and the techniques used to characterize the devices. The associated publications and contributions for this chapter are as follows:

  - M. A. Ebrish, H. Shao, and S. J. Koester, "Operation of multi-finger graphene quantum capacitance varactors using planarized local bottom gate electrodes," *Appl. Phys. Lett.*, vol. 100, no. 14, p. 143102, 2012.

- Chapter 3 focuses on the non-idealities of the device performance and demonstrates the effect of each one of them on the capacitance vs. voltage curve. The associated publications and contributions for this chapter are as follows:

  - M. A. Ebrish, H. Shao, and S. J. Koester, "Operation of multi-finger graphene quantum capacitance varactors using planarized local bottom gate electrodes," *Appl. Phys. Lett.,* vol. 100, no. 14, p. 143102, 2012.

  - M. A. Ebrish and S. J. Koester, "Dielectric thickness dependence of quantum capacitance in graphene varactors with local metal back gates," in 70th Device Research Conference, 2012, pp. 105–106.

- Chapter 4 continues the discussion on the non-idealities by addressing the border traps in $HfO_2$ and extracting their density. The associated publications and contributions for this chapter are as follows:

  - M. A. Ebrish, D. A. Deen, and S. J. Koester, "Border trap characterization in metal-oxide-graphene capacitors with $HfO_2$ dielectrics," in 71st Device Research Conference, 2013, pp. 37–38.

- Chapter 5 focuses on the effect of one of glucose oxidase functionalization on the graphene varactors characteristics. The associated publications and contributions for this chapter are as follows:

  - M. A. Ebrish, E. J. Olson, and S. J. Koester, "Effect of Noncovalent Basal Plane Functionalization on the Quantum Capacitance in Graphene" *ACS Appl. Mater. Interfaces*, vol. 6, pp. 10296−10303, 2014.

  - Part one of this work was a joint effort by this author and Eric Olson who carried out the chemiluminescence and AFM measurements. Special thanks to Yoska Anugrah for preparing the exfoliated graphene samples for this

work. And to Prof. Narayana R. Aluru for providing us with the DFT and MD results.

- Chapter 6 explores the effect of humidity on graphene varactors. The associated publications and contributions for this chapter are as follows:

  - D. A. Deen, E. J. Olson, M. A. Ebrish, and S. J. Koester, "Graphene-Based Quantum Capacitance Wireless Vapor Sensors" *IEEE Sensors Journal*, vol. 14, pp. 1459-1466, 2014.

  - E. J Eric, R. Ma, T. Sun, M. A. Ebrish, N. Haratipour, K. Min, N. R. Aluru, and S. J. Koester, "Capacitive Sensing of Intercalated Molecules Using Graphene" *Submitted*, 2015

  - Part one of this work was a joint effort by this author and David Deen, and Eric Olson who carried out the wireless measurements. Part two was a joint effort by this author, Eric Olson, and Rui Ma, who carried out the vapor wires measurements. In addition, Prof. Narayana R. Aluru for providing us with the DFT and MD results.

- Chapter 7 summarizes the work, and provides recommendations for future work.

  - The in-house CVD graphene was grown by Jing Li and Qun Su.

# Chapter 2 :
# Device Fabrication and Measurement

*"The synthesis and transfer techniques can be scaled, and it appears as if there are no limitations on the size of the graphene films except for the dimensions of the substrate and growth system."*
*Xuesong Li.et al ACS, Nano Lett., 2009, 9 (12), pp 4359–4363.*

## 2.1 Device fabrication

### *2.1.1 Back gate process*

Graphene field effect transistors (GFET) have been made in both top gated and bottom gated configurations. Most of the bottom-gated GFETs used Si as the back gate. Another way to create local back gates with graphene was described in [51]. In that work, GFET devices using exfoliated hexagonal boron nitride (h-BN) dielectric were fabricated by embedding h-BN in a mechanically flexible polyimide (PI) film and then flipped and transferred to another substrate to create a local back gate. Utilizing a local back gate is not a simple process to fabricate due to the roughness that can be introduced by the buried gate to the system. CMP can be used in this case to mitigate the roughness as in [52], however the dielectric itself can introduce some level of roughness depending on the way it was deposited. In this research a combination of dry etch and wet etch were utilized to achieve the best anisotropic trench for the gate. Why is the back gate process necessary for graphene varactor sensors? The back gate configuration provides several advantages over the top gate. First of all, the sensor design requires the sensing electrode to be fully exposed to the desired agent. Secondly, due to the inert nature of graphene, growing or depositing any type of oxide on top requires functionalizing the graphene [53]. However, this functionalization could lead to several issues, such as changing the

graphene electronic structure [54], particularly if covalent functionalization is used. In addition, growing the dielectric on top without functionalization could result in nucleation only on defect sites and edges which will not guarantee a continuous layer of the dielectric [55]. On the other hand, the back gate configuration can provide a high-quality continuous dielectric since the atomic layer deposition initiates on a metallic layer. However, there are some challenges with this configuration. For one, this configuration is very sensitive to the gate electrode topography, and the gate must be recessed and planarized to the surrounding dielectric. If the gate edges are rough, then the graphene on top of it could break at those rough edges. As shown in Figure 2-1(a) the multi-finger configuration can also be seen as a multi-edge configuration, hence, if the edges are not flattened they will cause tears to the graphene sheet. In this work, throughout making that device it was found that the best anisotropic profile can be achieved by mixing the wet etching process with a dry etching one (see Appendix A).

The fabrication started by growing a relatively thick thermal $SiO_2$ (~980nm) on a lightly-doped p-type Si wafer, in order to mitigate parasitic capacitance. In some other devices an insulating fused quartz wafer was used (details are in Appendix A). The gate electrode was patterned using optical lithography, and a combination of dry and wet etching was used to form the recess 50 nm in the insulating layer of the substrate for the gate electrode, followed by evaporation and lift-off of Ti/Pd (10/40 nm). The resulting planarized gate electrode is shown in Figure 2-1.

### 2.1.2 Dielectric growth or transfer

Quantum capacitance was previously characterized in graphene using a top-gate configuration [56]. In addition to the difficulty of achieving a thin layer of an insulator on top of graphene due to its inert properties [57], varactors using top-gated geometries are not well-suited for sensing applications. In our back-gated graphene devices hafnium

dioxide ($HfO_2$), is used as a high-k dielectric which is needed to obtain a high oxide capacitance, so that the quantum capacitance will dominate close to the Dirac point [23], [50]. The desired thickness of the $HfO_2$ is deposited by atomic layer deposition (ALD) and afterward the sample is annealed at 400 ºC for 5 minutes; this step is believed to reduce the disorder in the $HfO_2$ which shows as a reduction in the hysteresis [58]. It is difficult to determine the physical thickness of the oxide due to the fact that it is grown on buried gate thus conventional ellipsometry techniques cannot be used to determine the thickness on the metal gate itself. However, it is the equivalent oxide thickness (EOT) that is the most relevant parameter. The EOT is related to the dielectric constant and the physical thickness by

$$EOT = \frac{3.9 \times t}{\varepsilon_r}, \qquad 2\text{-}1$$

where $t$ is the oxide thickness and $\varepsilon_r$ is the relative permittivity.

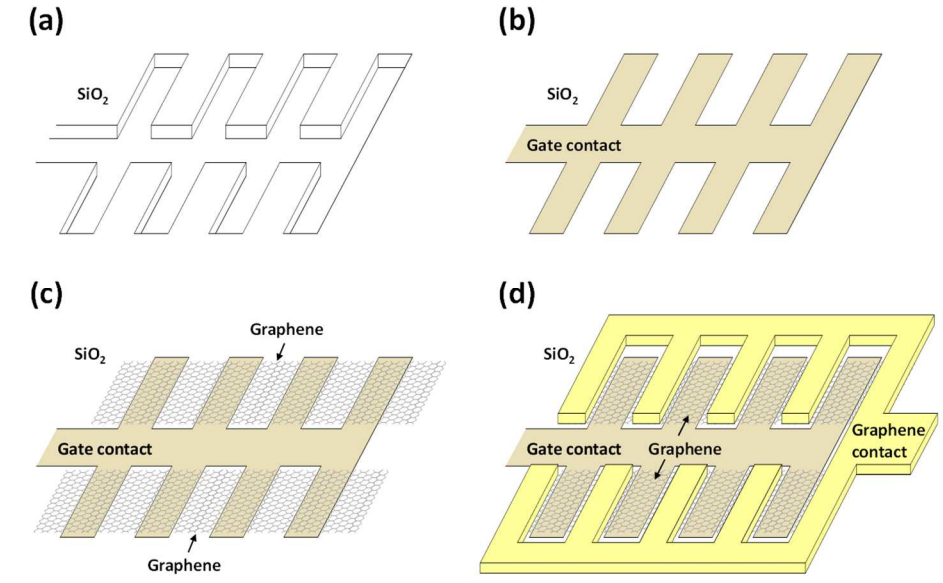


Figure 2-1: Fabrication sequence: (a) Gate recess etch. (b) Gate metal and high-k dielectric. (c) Transfer and pattern graphene. (d) Contact metallization.

The ALD system works in binary pulses. Starting with one pulse of water for 15 ms, followed by a pulse of tetrakis(dimethylamido)hafnium for 400 ms [59]. The procedure and the steps are shown in Figure 2-2(a). The end of the two pulses defines one a loop. The number of loops is related to the deposited thickness. The recipe that is used here produces a growth rate of 0.95Å per loop. However both the witness sample and the resulted EOT from the device suggest a fluctuation in the deposition rate. Figure 2-2(b) shows a statistical plot of EOT versus the number of loops across several samples. Ideally the relationship should be linear; however the decrease in the number of loops does not necessarily show a proportional decrease in the EOT. The plot suggests inconsistency in the thickness results; one of the reasons for the inconsistency could be the quality of the $HfO_2$ itself from one run to another. In other words, the dielectric constant could change from one run to another thus the EOT is higher for the same physical thickness. Another dielectric was also explored in order to compare it with the $HfO_2$. CVD h-BN was analyzed due to its similar crystal structure to graphene. Many research groups have reported achieving GFETs with higher mobility using exfoliated h-BN [60], [61]. However, in this work, CVD h-BN was utilized to determine if the same benefits could be achieved.

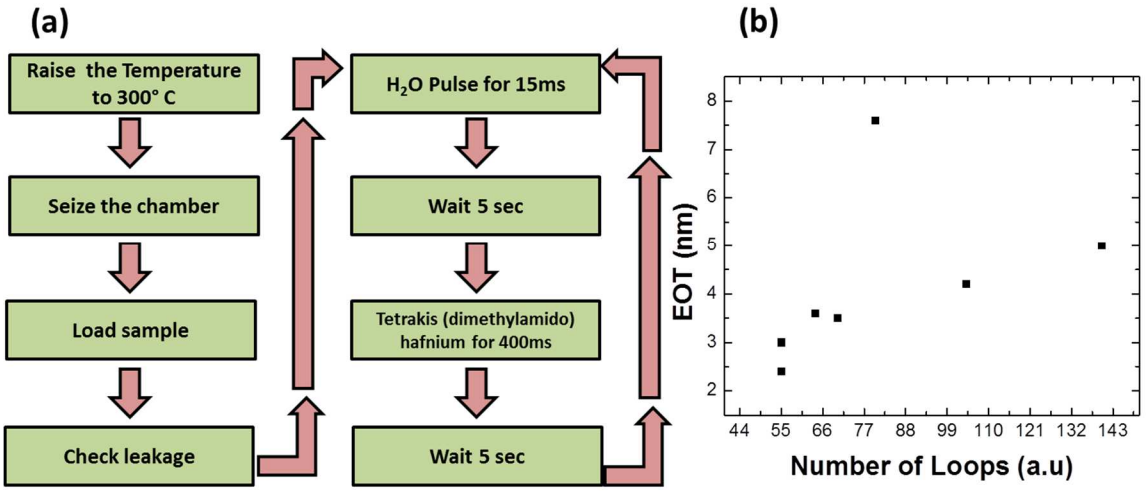


Figure 2-2: (a) The steps for the ALD process. (b) Relationship between the number of loops and the $HfO_2$ EOT.

### 2.1.3 Graphene growth and transfer

Exfoliated graphene does not come in large pieces that can be easily transferred to any substrate, but rather in small flakes (few microns) scattered in random places. Therefore significant focus in the graphene community has been dedicated to large area synthesis that can also be transferable to any substrate. Reference [34] presented the first large area CVD graphene, which has been commercially available since 2010. Our first vendor was Graphene Supermarket; however in 2012 our group started producing our own homegrown graphene. Single-layer graphene was grown on a Cu foil, and then coated with polymethyl methacrylate (PMMA) as a mechanical support. The Cu was removed using an etchant solution such as ($Fe_2Cl_3$ or $(NH_4)_2S_2O_8$). The graphene was then transferred onto the wafer with the local bottom gate electrode using an aqueous transfer process, and the PMMA removed using a solvent cleaning as shown in Figure 2-3 [62]. The graphene was then patterned and etched using $O_2$ plasma. Finally, contact electrodes to the graphene consisting of Cr/Au (10 / 90 nm) were patterned via photolithography, and liftoff was done to complete the fabrication process Figure 2-1.

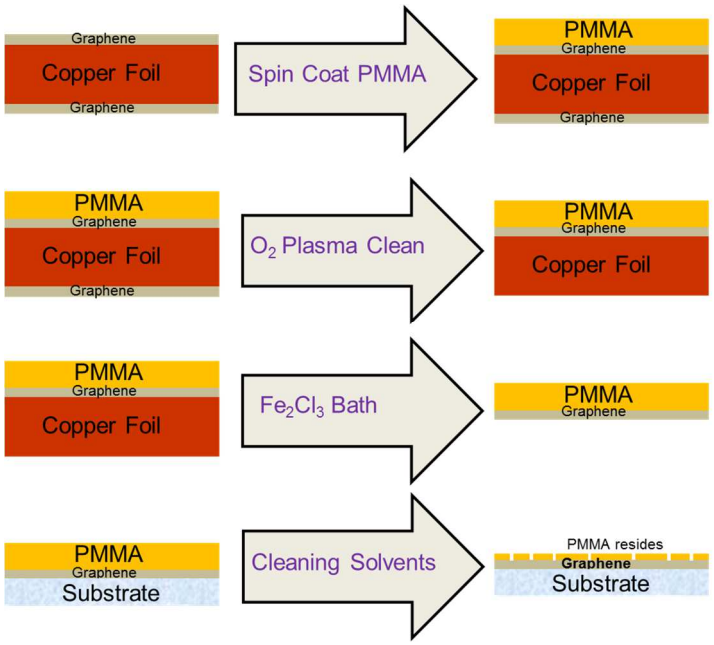


Figure 2-3: CVD graphene aqueous transfer process with PMMA as a support layer.

In addition to the aqueous transfer process that is widely used in the CVD graphene community, an electrochemical delamination process has also been described, though this process still requires a mechanical support such as PMMA for graphene. However, rather than etching the copper in an etchant, the copper can be delaminated from the graphene in a electrochemical process [63]. There may be advantages associated with this new method however, it is still manual and does not reduce the residues. Furthermore, one still needs to rinse the graphene using DI water beakers which will put the graphene film through the same stress as in the aqueous process. We have tried this process and did not notice any improvement in terms of tears and breaks or residues. This process was slower and more time consuming so it was not adapted as our main method of transfer.

In addition to the varactors, standard three-terminal field-effect transistors were also fabricated, as well as metal-insulator-metal (MIM) capacitors, the latter of which were used to calibrate the capacitance arising from the $HfO_2$ dielectric. An optical micrograph

of completed devices is shown in Figure 2-4. The Raman spectrum of the transferred single-layer graphene taken immediately after transfer is shown in Figure 2-5(a).

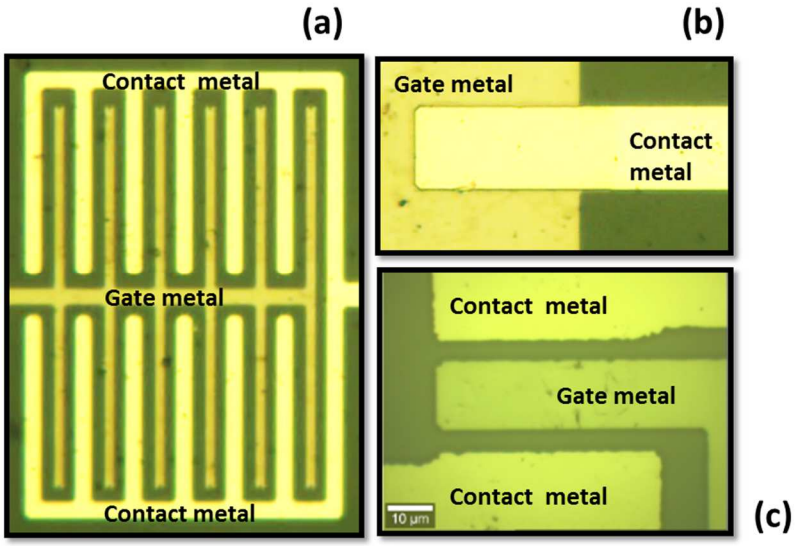


Figure 2-4: Micrographic images of the final devices. (a) Multi-finger varactors. (b) Metal-Insulator- Metal MIM. (c) Graphene field effect transistor.

The graphene transfer efficiency was not always high, thus estimating the actual device area has been a real challenge. Graphene is a transparent material and hard to see with an optical microscope; in addition the PMMA residues do not just hinder observing the graphene but also hinder taking a good AFM scan. The roughness of the $HfO_2$ surface is also another factor that makes the AFM not a very useful tool when it comes to defining the graphene area. Two other techniques can be used to estimate the area; one is very time consuming and laborious while the other is very tricky and potentially misleading. Raman mapping is the time consuming technique, but it is the most accurate technique to estimate the area with minimum error. Scanning electron microscopy (SEM) can be misleading because the graphene appears as shadow in which small tears can be hard to spot. The PMMA residues sometimes can be counted as graphene. As was mentioned in chapter 1, graphene has a distinct Raman signature that made using Raman spectroscopy

to identify graphene properties such as number of layers, doping, and quality very common methodology. Raman mapping is another useful tool to map out a large area of graphene. That can give an estimate of the real device area, or in other words the transfer efficiency. Figure 2-5(b-c) shows some images of the mapping and SEM.

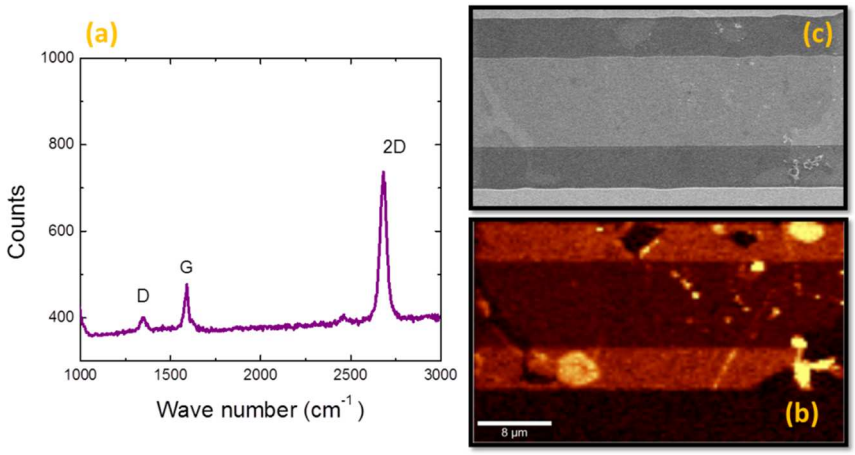


Figure 2-5: (a) Graphene point Raman signature taking upon transfer. (b) 2D peak Raman mapping on GFET. (c) SEM images on the GFET.

### 2.1.4 Contacting the graphene

The contact resistance is a concern in any device. When it comes to graphene devices however, the contact resistance is a complicated issue due to many factors: the difference in dimensionality between graphene (2D) and metal-contact materials (3D), graphene aqueous transfer process, lithography residues, and finally the work function differences [64]–[66]. Since graphene is a gapless semiconductor, no Schottky barrier exists, but a tunneling contact can still form that increases the contact resistance. However, it is still important to adjust the work function properly in order to minimize the interfacial resistance. Since CVD-graphene is typically p-type doped, higher metal work functions are preferred to form ohmic contacts. Pd with a work function of (~5.6 eV) is a good candidate as a graphene contact metal. Since Pd has poor adhesion to graphene, an

adhesion layer of Ti (~1.5nm) was evaporated before the Pd [67]. More recently, L. Wang, *et al*. in [66] pointed out that Cr is a better metal contact because it forms a stronger coupling with graphene and it has a similar work function (~0.16 eV difference) according to DFT calculations. Thus, Cr/Au was used as the standard metal contact in all recent devices. Graphene's high mobility as a channel material is not the overall device mobility because the contact resistance is dominating the electron transport [64], [65], [68], [69]. Extracting the contact resistance can be performed using the transfer length method (TLM) which is a valid approach for any non-ballistic device, where the channel length is much longer than the mean free path of the electrons. However, TLM measurements can be difficult in CVD graphene due to delamination and tears in the graphene which can cause the channel width to vary. In addition, residues from the transfer process can cause variability in the contact resistance. Figure 2-6(a) shows a schematic diagram of typical two-terminal TLM devices used in this work. Obtaining a constant value of the contact resistance was not possible in the initial work; however after changing the contact metal to Cr/Au instead of Pd/Ti/Au stack, more consistent TLM measurements were obtained. Figure 2-6(b) shows typical plot of resistance versus the distance between the two contacts. The points linearly fit with 0.08 error and the intercept with the y-axis represents double the contact resistance, therefore the contact resistance can be extracted as

$$R_C = \frac{Intercept}{2} \times width, \qquad 2\text{-}2$$

Where $R_C$ is contact resistance and width in this case is 10μm. The sheet resistance is another parameter that can be extracted from the TLM measurements. The variations in the sheet resistance values are usually a function of the CVD growth parameters. Sheet resistance depends on the slope of the linear fit, and it can be defined as

$$R_{sheet} = Slope \times width. \qquad 2\text{-}3$$

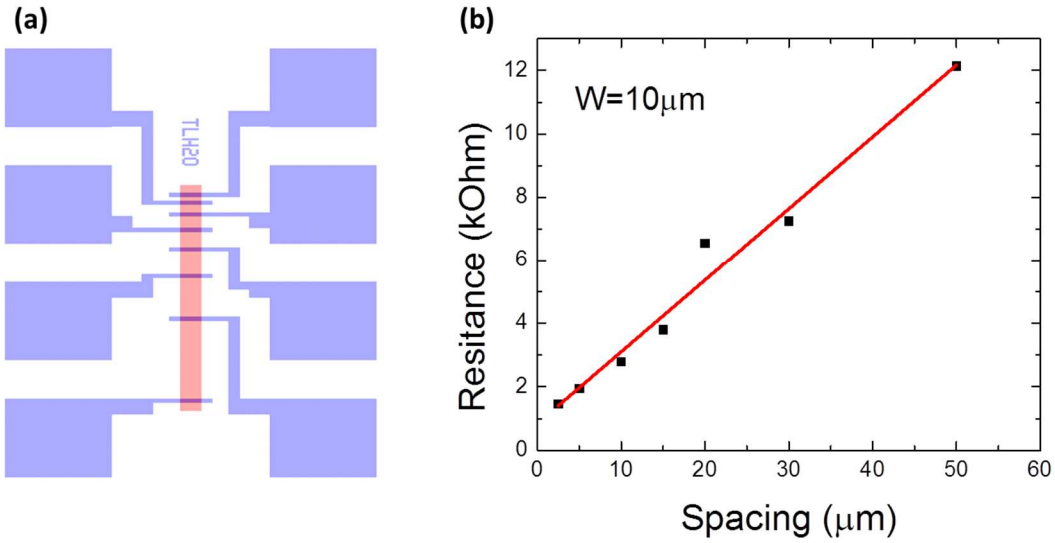


Figure 2-6: (a) Schematic of the TLM structure. (b) TLM measurement for graphene sheet $R_C$ is 4.15Ω.mm; and the $R_{sheet}$ is 2000 Ω/square, with standard error of 0.08.

The values shown in Figure 2-6(b) namely ($R_C$= 4.15Ω.mm and $R_{sheet}$=2000Ω/square) could be considered high compared to typical FET devices; however for the purpose of this study and as varactor device those values are not a major concern.

Aside from the work function matching and the quality of the graphene, the contact resistance suffers mainly from the residues on the graphene sheet. The source of those residues can be remains of the PMMA and the organic lithography residues. Unlike other materials graphene can be etched in $O_2$ plasma which makes cleaning its surface from organic residues more difficult. Numerous reports have described methods to clean the graphene surface after transfer [67], [70]–[72]. The method in [67] was tired on one sample. The basic idea of the method is to reduce the organic residues from the lithography by depositing a sacrificial layer that can be easily etched away. Starting after patterning and etching of the graphene in $O_2$ plasma, 2nm of Al was deposited and oxides as a sacrificial layer to reduce the contact resistance, then the contact metal stack

of Ti, Pd, and Au (1.5/45/100 nm) was deposited and lifted. The contact resistance in this particular sample has not improved much; therefore this procedure was not tried again.

### 2.1.5 Pads layer and the isolation scheme

One of the ultimate goals in this research is to make glucose sensors. Therefore, a different mask set was designed to allow measurement of varactors in an electrolyte solution. In addition, a more complex process was needed to ensure that the devices could be probed on a standard probe station. That requires performing measurements in an aqueous set up. The electrolyte solution (drop of liquid on the device active area) as in Figure 2.11(a) changes the dynamics of probing the device. The probing has to be away from the active device area. Therefore long metal pads are needed to connect the device to the probes as in Figure 2-7(b). Since the device contacts are made of metal, an isolation scheme is needed to avoid disturbing the measurements with the noise in the contacts. Those conditions led to more sophisticated mask design that included long contact pads (Length of 150mm) which allows probing the device without jeopardizing the measurements by submerging the probes into the aqueous solution. With this addition to the mask came the need to eliminate any parasitic capacitance that is associated with the metal pads. Insulator substrate such as quartz are more favorable, or Si substrate with a very thick layer of $SiO_2$ (980nm). The isolation scheme is based on the idea of having a reasonably thick layer (~1μm) of an insulator everywhere except on the device's active area (the graphene surface). This insulator should be sustainable and must not decay or react with DI water, PBS or any other electrolyte that could be used in future experiments. The first candidate tried was plasma-enhanced chemical vapor deposition (PECVD) $SiO_2$. It starts with depositing a thick layer of $SiO_2$ by PECVD and then opens up the graphene device window by etching down the $SiO_2$; however this method has damaged the device. The overall device performance has been affected by this method. Some of those devices with this process were characterized and utilized for initial sensing

demonstrations, which will be described in chapter 6. The isolation scheme process however remains under development, and additional steps could be needed to ensure device isolation in an electrolyte setup.

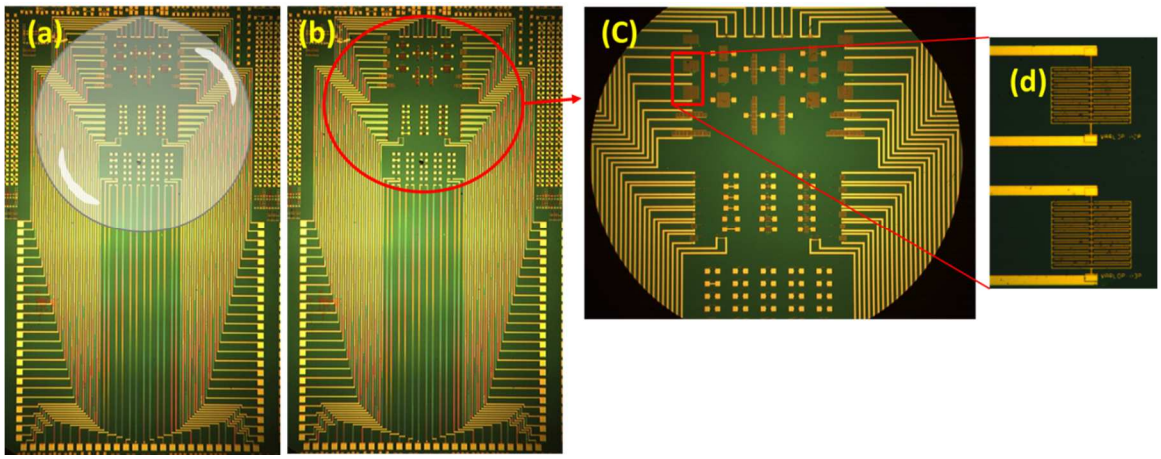


Figure 2-7: Sensor mask layout (a-b) shows the active sensor region (c-d) zoom in the main sensors area

## 2.2 Device measurements and characterization

### 2.2.1 Measurements environment

Graphene is sensitive to ambient conditions, therefore measuring graphene devices in vacuum guarantees stability and consistency in the results. The typical measurement procedure for the graphene varactors was as follows. The devices were loaded into the chamber, and a pre-bake was performed in vacuum for an extended time (typically 15-30 hours at 380 K) in order to desorb moisture from above and below the graphene surface. Much of this moisture is a result of the aqueous transfer process. However, devices were also tested in other environments as well as part of investigations to determine the effect of the ambient conditions on the device performance. Temperature-dependent measurements were also performed as a way to probe the density of states and disorder in

graphene. Both liquid helium and liquid nitrogen were used to perform measurements with base temperatures of 4.2 K and 77 K, respectively as shown in Figure 2-8.

### 2.2.2 C-V and Temperature-dependent measurements

Different devices require different measurement set up. For instance Field effect transistors were measured in DC set up while the varactors devices were measured in AC and DC setting, in which the local back gated devices are swept with DC voltage (-2 to 2 V) while applying a small ac signal 50 rms, with wide range of frequencies from 5kHz to 500kHz. Figure 2-9(a) shows typical C-V curves at multiple frequencies. The circuit model at the B1500A end is assumed to be Cs-Rs model as shown in Figure 2-9(b). At low temperatures the quantum capacitance has a small value. Thus the C-V curve is steeper at lower temperatures. In addition the low temperature measurements can help in studying the disorder as will be demonstrated in detail in the next two chapters. In general the temperature dependence measurements are important to monitor the device behavior at different conditions. The Laskshore system has the capabilities to run those measurements with either liquid helium or liquid nitrogen depending on the desired temperature to reach. The high-vacuum chamber from lakeshore is also open-cryogenic system that can accommodate both liquid helium and nitrogen depending on the lowest temperature needed. For those experiments a dower is needed in order to transfer the liquid cryogenic to the chamber. A transfer line will be inserted slowly into the dower till it reaches the bottom. The dower is pressurized with helium gas (in the case of using liquid helium) to maintain a steady cryogenic flow to the system. Once the base temperature (4.2K) is reached at both the stage that holds the sample and the magnet the measurement can start. Then the temperature can be raised using our temperature controller. It is capable of operating in the temperature range of 4.2 to 380 K. Also, the sample is anchored to the stage using silver paint. The liquid helium is transferred into the cryostat through a transfer line by pressurizing the helium Dewar. The sample holder

is cooled down by a continuous liquid helium flow through cryostat and the helium gas exhaust comes out of the exhaust port. Typically, cool down from 300 K to 10 K takes about 100 minutes. To reach the base temperature 4.2K the system consumes about 15 liters. After that the helium consumption is about 1.5 liters/hr.

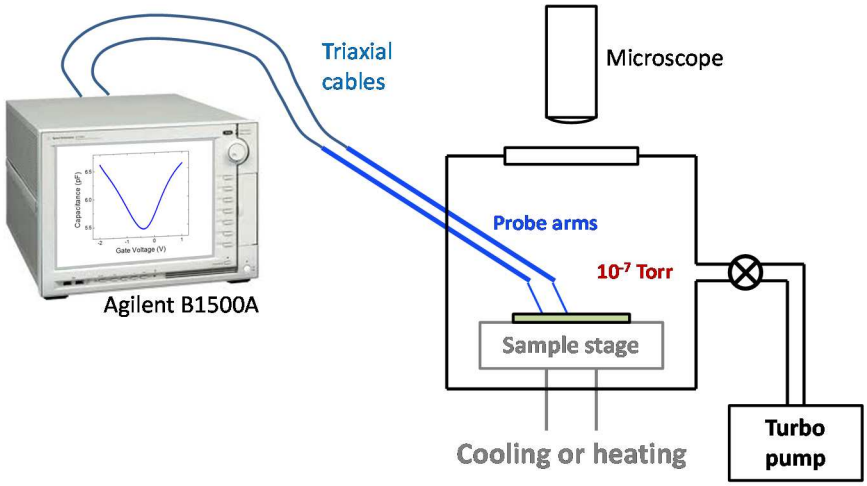


Figure 2-8: I-V and C-V measurements were performed using an Agilent B1500A in vacuum using a cryogenic probe station

Measurement works as a probing mechanism to probe those non-idealities and trace them back to the disorder in graphene. Because of the direct relationship between the quantum capacitance and density of state and Fermi level in graphene as in

$$C_q \approx q^2 DOS, \qquad 2\text{-}4$$

where $C_q$ is the quantum capacitance, $q$ is electron charge, and DOS stands for density of states.

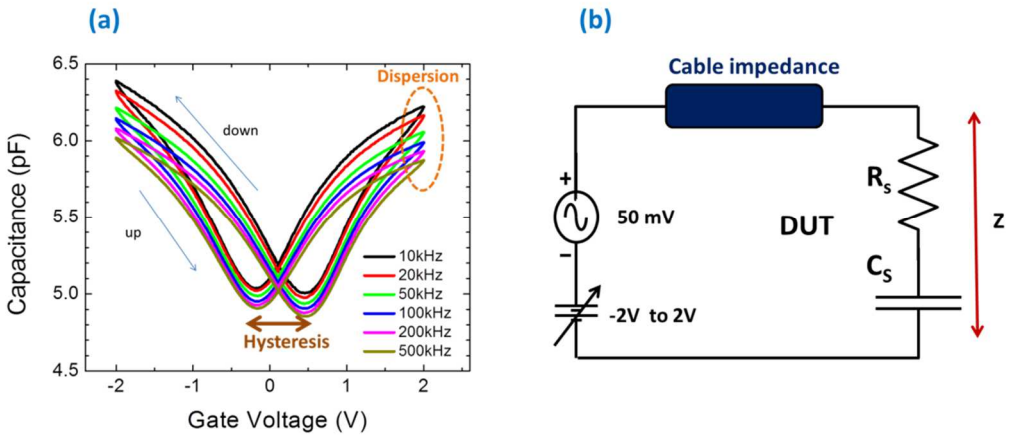


Figure 2-9: (a) Typical C-V curve for the graphene varactors. (b) The equivalent circuit of the C-V measurements.

### 2.2.3 I-V measurement

Single finger geometry have two contacts that can be considered drain and source hence one can apply FET I-V measurements on them in order to observe certain parameters such as Dirac point , transconductance, mobility and saturation behavior. Mobility is the most challenging parameter to extract due to the tears and breakages in the graphene sheet and low transfer efficiency. Thus the real device width is hard to estimate in other words the device geometry can be considered unknown. This particular problem is persistent still, the Raman mapping was found to be a useful tool to give a decent estimate for the area; however it is a laborious techniques that consumes a large amount of time per device. The current-voltage (I-V) measurement was mainly performed to confirm the Dirac point value, and observe the device modulation. Typically the Dirac point voltage (neutrality point) is the same in both the C-V and I-V measurement and it depends on the type of insulator that is used. As will be shown later the h-BN has much more p-type doing effect than the $HfO_2$ which can be partially explained with the band structure differences but still the positive shift is more than expected largely due the oxygen vaccines in the oxide which will be explained later in chapter 4. Figure 2-10

shows the typical drain current versus drain voltage ($I_D$-$V_D$), and drain current versus gate voltage ($I_D$-$V_G$) for GFET with $HfO_2$ as gate dielectric.

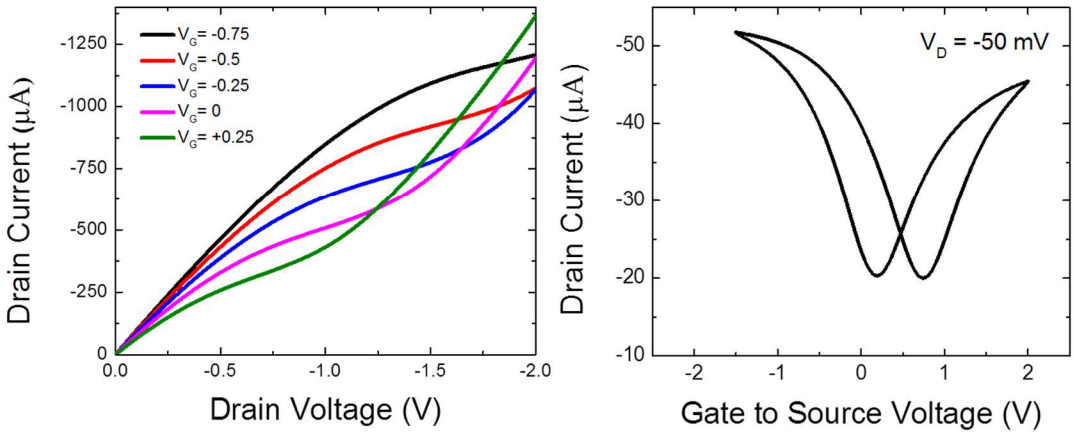


Figure 2-10: $I_D$-$V_G$ and $I_D$-$V_D$ characteristics for a long channel GFET with $HfO_2$ as gate dielectric.

# Chapter 3 :
# Graphene Varactor Non-Idealities

*"The electronic structure of graphene causes its charge carriers to behave like relativistic particles. For a perfect graphene sheet free from impurities and disorder, the Fermi energy lies at the so-called 'Dirac point', where the density of electronic states vanishes. But in the inevitable presence of disorder, theory predicts that equally probable regions of electron-rich and hole-rich puddles will arise." J. Martin et al. Nature physics, 2008. 4.2, 144-148.*

## 3.1 Introduction

### *3.1.1 Ideal vs non-ideal*

Quantum capacitance is an electrostatic property in all devices. For most field-effect transistors, the quantum capacitance is seen as a negative, as it can degrade the device performance because it reduces the overall device capacitance. Graphene, however, offers the possibility to utilize the quantum capacitance as a means to make a varactor whose capacitance can be tuned easily by changing the carrier concentration. Quantum capacitance has also been used as a direct measurement of the density of states in many materials systems, including carbon nanotubes as well as graphene [13], [14]. Utilizing the quantum capacitance to probe the density of states is a successful methodology to understand graphene electronic properties. Quantum capacitance phenomenon in graphene has been measured in graphene based varactors. This chapter focuses on how various types of non-idealities affect the performance of graphene varactors. In order to understand the variable capacitance in graphene and utilize it in advanced applications one must understand the effect of all the non-idealities that are associated with either the nature of the materials themselves (graphene and $HfO_2$), or the fabrication process. Each non-ideality can have a significant impact on the total capacitance versus applied voltage

curve. Figure 3-1 shows how various non-idealities can decrease the capacitance tuning observed in graphene varactors. The ideal capacitance versus voltage (C-V) curve is in black, and the effect of each of the non-idealities has a different C-V curve on the same plot. In Figure 3-1 the random potential fluctuations, which is the measure of the disorder in the graphene, smears out the curve around the Dirac point but it does not have much of an effect far away from it. The interfacial layer on the other hand affects the overall shape of the C-V curve. It decreases the total capacitance and the overall capacitance tuning. The hysteresis on the other hand shifts the Dirac point of the second sweep, and they also affect the shape of the single sweep curve by adding additional stretch-out. Finally the area loss works as a scaling factor for the total capacitance. All the non-idealities in Figure 3-1 can be observed at any applied frequency in the C-V measurements. Moreover those non-idealities are analyzed at one frequency. The non-ideality that is related to frequency dispersion (multiple-frequencies) will be discussed in the next chapter.

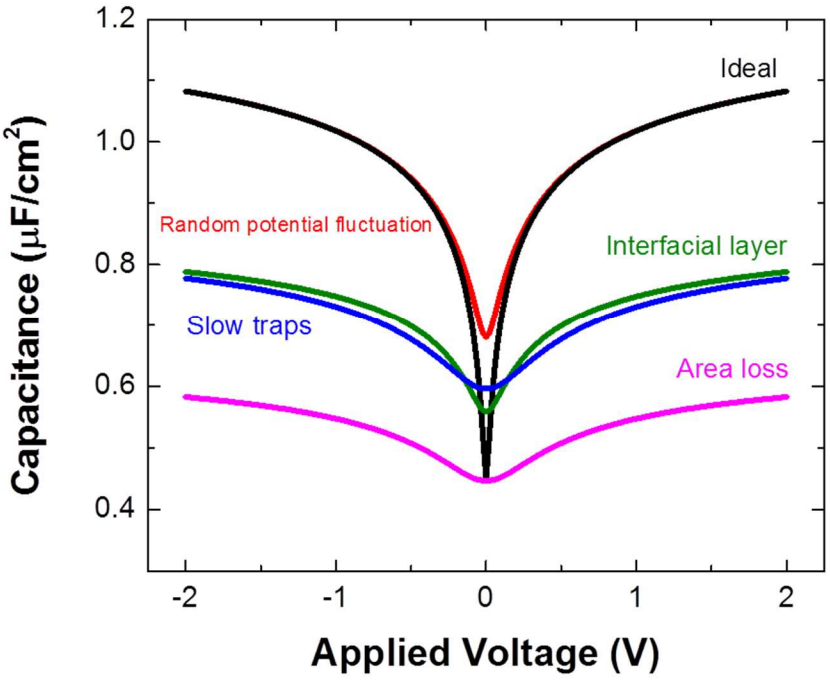


Figure 3-1: Theoretical capacitance vs. gate voltage for graphene varactors assuming various degrees of non-idealities. Ideal case (black), including random potential fluctuations (red), including interfacial layer (green) , including slow traps (blue) and including area loss (magenta).

## 3.2 Random potential fluctuations

### *3.2.1 Background*

Random potential fluctuations play an important role in shaping the quantum capacitance in graphene. In this section, both the origins of these fluctuations and the way they can be mathematically modeled will be explored. Random potential variations can arise due to a disorder in the graphene as well as the adjacent substrate. However distinguishing these two sources from each other can be difficult. Previous experiments conducted using scanning tunneling microscopy (STM) showed that the disorder induces electron-

hole "puddles," which arise from substrate defects in a close proximity to the graphene [73], [74]. The fact that electrons in suspended exfoliated graphene show nearly ballistic transport with a mobility of ~120,000 $cm^2/Vs$ highlights the strong role the substrate plays in the electronic properties of graphene [75]. Substrate random charges give rise to a random electrostatic potential across the graphene sheet. If those charges are uniformly distributed then they will dope the graphene i.e. shift the minimal conductivity to a non-zero voltage without affecting the average band structure. In the case of inhomogeneity, the charges will affect the minimal density of states value, inhibiting it from being zero, and thus it will smear the C-V curve. The charge disorder in the substrate acts as an extra potential applied at a particular spot. The standard deviation of the all those potentials can represent the random potential fluctuation across the whole sample. It is important to notice that the sum of the total charges (considering their sign) could be zero. Therefore the Dirac point is still at zero, but the density of states is not zero. One must distinguish between the electrons or holes added for doping and the ones that cause disorder. In the case of doping $N_{net} = p\text{-}n$, where $N_{net}$ is the total number of free charges in the sample, $p$,$n$ are the number of holes and electrons respectively. However in the case of disorder the number of charges can be considered the sum of all carriers ($N_{disorder} = n+p$). Hence even if there is net effect of zero charge i.e. no doping, that does not necessarily mean that there are no residual charges that have smeared the quantum capacitance. Reference [73] studied in detail the spatial density and voltage fluctuation across a flake of graphene monolayer on $Si/SiO_2$ substrate. Their results, shown in Figure 3-2(a), show a 2D map of the density variations in graphene at the Dirac point (net carrier density of zero). The blue and red areas represent holes and electrons respectively. The existence of these electron-hole puddles at zero bias is a strong indication of potential fluctuations in the graphene. Figure 3-2(b) summaries the density fluctuations where the standard deviation was found to be ($\Delta n = \pm 3.9 \times 10^{10}\ cm^{-2}$) [73].

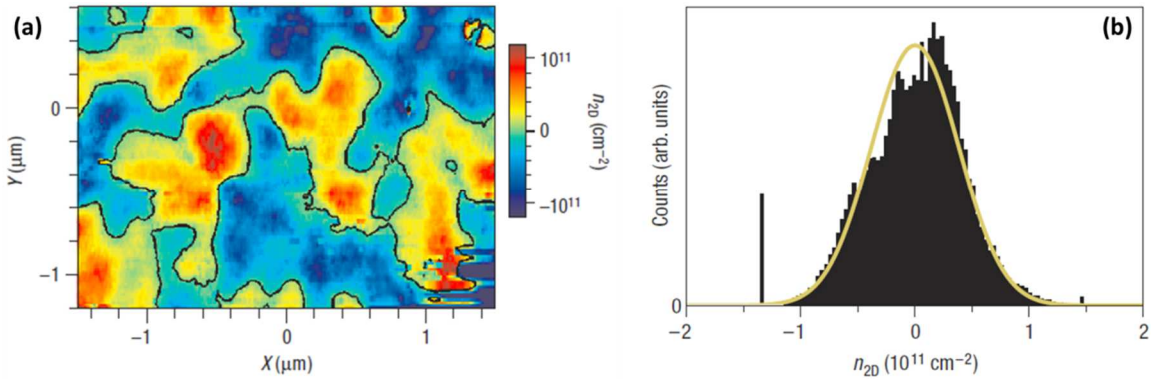


Figure 3-2: (a) Color map of the spatial density variations in the graphene flake extracted from surface potential measurements at high density and when the average carrier density is zero. The blue regions correspond to holes and the red regions to electrons. The black line marks the zero density contour. (b) Histogram of the density distribution in (a) [73].

Furthermore some of the graphene disorder is highly related to the way the graphene is made, as exfoliated graphene can have different disorder from epitaxially grown (EG) graphene and CVD graphene. Some studies on exfoliated graphene showed minimal intrinsic structural lattice defects in comparison to CVD and EG graphene [75]. Other studies show that the mobility in exfoliated graphene on $SiO_2$ at room temperature is four times higher than it is in CVD graphene on $SiO_2$ [34], [76]. These examples and more show the importance of the graphene source to the electronic properties and the disorder.

### 3.2.2 Random fluctuation models

In this section, the effect of random potential fluctuations on the shape of the graphene varactor C-V curve is described theoretically. In this analysis, the charge screening effect from the substrate will not be addressed. Instead, a simple statistical model is utilized. This model is based on dividing the sample into small pieces, each with a random potential shift, and then summing up the contribution of the different regions, determining the average carrier density that results and then fitting to the experimental data. This is not a rigorous microscopic model but will be shown later to fit the

experimental data very well. For CVD graphene laid on high-k dielectric the electron–hole puddles result in a rise in the density of state at the neutrality point. Due to those new states created by those residual charges in the vicinity of the Dirac point; the quantum capacitance effect at neutrality point (NP) is not as sharp, but smears quite a bit depending on the amount of those charges [11].

In order to model the effect of random potential fluctuations, we start with the quantum capacitance equation for pristine graphene:

$$C_q = \frac{2q^2 k_B T}{\pi(\hbar v_f)^2} \ln\left[2 + 2\cosh\left(\frac{V_{CH}}{kT}\right)\right], \qquad 3\text{-}1$$

where $V_{CH}$ is the applied potential relative to the Dirac point energy, $q$ is the electronic charge, $k_B$ is Boltzmann's constant, $\hbar$ is the reduced Planck's constant, $\nu_f = 10^8$ cm/s is the Fermi velocity in graphene, and $T$ is the measurement temperature. An analytical model inspired by the model in [16] was utilized used in both [50], [77] to compare the results to theoretical expectations. In this model, the gate-voltage dependence of the gate capacitance, $C(V_G)$ was calculated as

$$C(V_G) = \frac{C_{ox} * C_q}{C_{ox} + C_q}, \qquad 3\text{-}2$$

where $C_q$ is the quantum capacitance, and it can be defined as

$$C_q = \frac{\partial \rho}{\partial V_{CH}} * A, \qquad 3\text{-}3$$

and $C_{ox}$ is the oxide capacitance, and it can be written as

$$C_{ox} = 3.9 * A * \frac{\varepsilon_0}{EOT}, \qquad 3\text{-}4$$

where $A$ is the capacitor area, $\varepsilon_0$ is the permittivity of free space, and EOT is the effective oxide thickness from equation 2-1. The graphene sheet charge density, $\rho$, is determined assuming a random potential variation model, where the "unit charge density", $\rho_i$, in a specific region of the device is given by

$$\rho_i = -e * \frac{2}{\pi}\left(\frac{kT}{\hbar v_F}\right) * [\Im_1(+\xi_i) - \Im_1(-\xi_i)], \qquad 3\text{-}5$$

where

$$\Im_j(\xi_i) = \frac{1}{\Gamma(j+1)} * \int_0^\infty \frac{u^j}{1+e^{u-\xi_i}}, \qquad 3\text{-}6$$

$k$ is Boltzmann's constant, $\hbar$ is the reduced Planck's constant, $v_F = 10^8$ cm/sec is the Fermi velocity in graphene, T is the temperature, and $\xi$ can be defined as

$$\xi_i = \frac{e}{kT}(V_{CH} + \delta V_i), \qquad 3\text{-}7$$

where $V_{CH}$ is the applied voltage on the graphene that can be obtained from the voltage divider rule for two capacitance in series as:

$$V_{CH} = \frac{C_{ox}}{C_{ox} + C_q} * V_G. \qquad 3\text{-}8$$

A random potential variation, $\delta Vi$, is added to the channel potential, $V_{CH}$, assuming a Gaussian distribution with mean value of 0 and standard deviation of $\sigma$. The charge density in the graphene is then averaged over $m$ = 1000 random samples to obtain the final charge distribution:

$$\rho = \frac{1}{N}\sum_{i=N}^{N} \rho_i \,. \qquad 3\text{-}9$$

Equations 3-2 to 1-2 are solved iteratively by using EOT, σ, and $A$ as fitting parameters, and fitting the results to the experimental data as shown in Figure 3-3. In this case the graphene sheet has to be divided into small areas in which each has a uniform voltage distribution. So instead of the ideal case where 0V will be at the NP now the NP shifted to a value $\delta V$ so that $|\delta V| > 0$V. In other words the density of states is not zero at NP. Both EOT and the device area can be estimated in different ways, methods of estimating these parameters will be explored in detail in the coming sections.

The model described has been fitted to experimental data and the results are shown in Figure 3-3. The fitting was performed at different temperatures to enhance the accuracy. As will be explained later in detail, the graphene varactor devices have several unknowns: the EOT, the area and $\delta V$, and therefore having several temperatures improves the fit accuracy. The experimental data at each temperature were shifted such that $V_{Dirac} = 0$, and the capacitance was normalized to the value at $V_G - V_{Dirac} = +2$ V, in order to account for the change in the maximum overall capacitance vs. temperature, which is otherwise not accounted for in the model. Though the C-V plots in Figure 3-3(b) is steeper than it in Figure 3-3(a) due to the difference in the EOT, the steepness of the C-V curve at each curve does increase as the temperature decreases. This increase in the steepness is expected because the quantum capacitance is temperature dependent as in equation 3-1. The random potential fluctuation $\delta V$ versus the counts forms a Gaussian distribution in which σ parameter is basically the standard deviation of that. The EOT values were estimated from the metal-insulator-metal (MIM) devices. Generally this model appears to fit the experimental data at lower temperature with lesser error than it is at higher temperatures, probably because it does not account for other thermionic effects at higher temperatures.

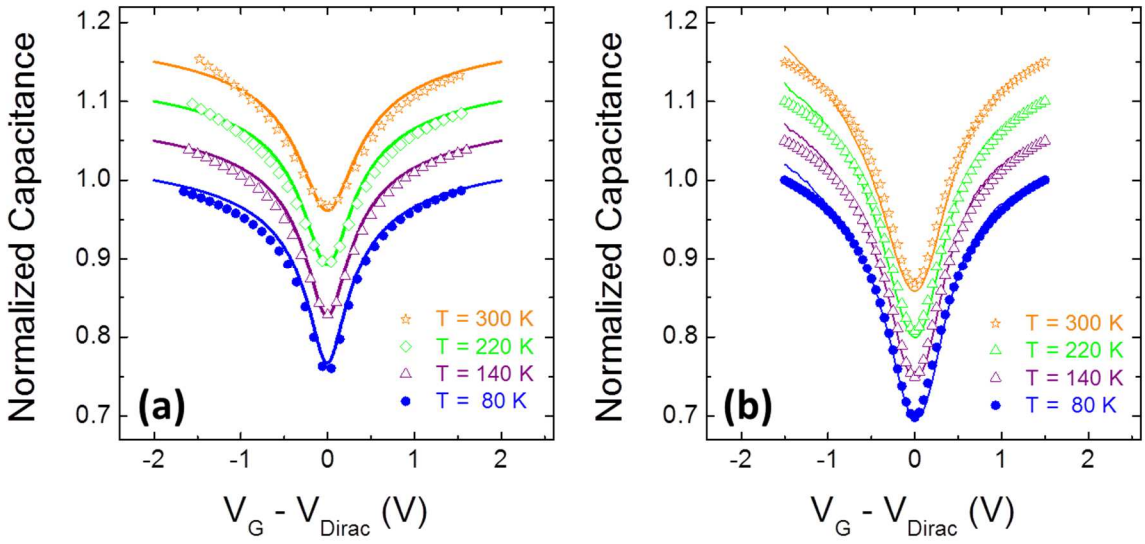


Figure 3-3: (a) MIM EOT = 4.1 nm, extracted EOT = 6.8 nm, σ = 65 mV. (b) MIM EOT = 2.7 nm, extracted EOT = 2.7 nm, σ = 105 mV. The curves have been shifted along the y-axis for clarity.

One of the difficulties of the model presented above is that it requires a numerical solution and therefore the fitting procedure to the data is computationally intensive. A simpler model was presented in [78] that utilizes a single effective temperature to represent the average disorder in the graphene. The quantum capacitance equation with the new effective temperature model can be written as

$$C_q = \frac{2q^2 k_B T_{eff}}{\pi(\hbar v_f)^2} ln\left[2 + 2\cosh\left(\frac{E_f}{kT_{eff}}\right)\right], \qquad 3\text{-}10$$

$E_f$ is the Fermi energy relative to the Dirac point energy. $q$, $k_B$, $\hbar$, and $v_f$ are as in equation 3-1. The term in the hyperbolic function has two variables; each can represent the disorder in two different but very similar perspectives. Previously the disorder was considered as an extra voltage that related to an extra charge on a microscopic level. In here however it is considered as an increase in the temperature. This equation in 3-10 is

that same as the ideal quantum capacitance relationship in equation 3-1, except that an effective temperature ($T_{eff}$) parameter is introduced, and it can be defined as

$$T_{eff} = \sqrt{T_0^2 + T^2}\,, \qquad 3\text{-}11$$

where $T_0$ is a parameter that represents the magnitude of random disorder in the graphene. This method of representing the random disorder in graphene is equivalent to previous descriptions in the literature [16], [50]. $T_0$ and EOT were fit by sum of squares optimization in MATLAB. A range of $T_0$ values are assumed then the program plots all the possible gate capacitance ($C_g$) versus gate voltage ($V_G$). The program also calculates the error per EOT and per $T_0$ as in Figure 3-4. The program chooses the EOT and $T_0$ where the smallest error occurs.

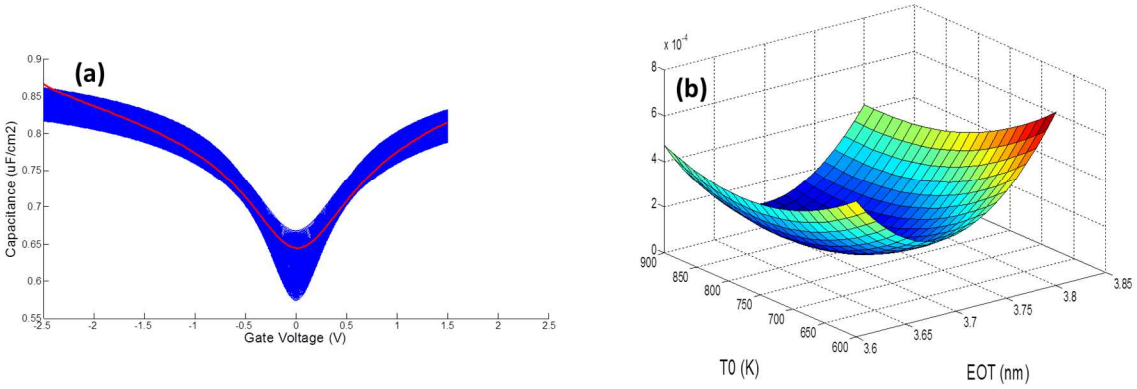


Figure 3-4: (a) C-V curves for experimental data (red line) plot along with all the possible C-V curves from $T_0$ and EOT matrixes (blue lines). (b) 3D plot for the fitting error versus all the possible $T_0$ and EOT.

An example of the fit is shown in Figure 3-5(a), where values of EOT = 4.9 nm, and $T_0$ = 500 K were extracted for a varactor measured in vacuum chamber at 4.2 K. The effective temperature model is mostly effective in the vicinity of the Dirac point. Because away from the Dirac point the quantum capacitance is quite large, and a small change to the

Fermi-level by the potential fluctuation does not cause a noticeable effect on the quantum capacitance. Figure 3-5(b) illustrates the effective temperature effect at quantum capacitance versus Fermi level plot.

The temperature effective model is equivalent to the statistical random potential fluctuations model that was presented earlier. Figure 3-6 shows the matched calculated quantum capacitance ($C_q$), versus Fermi energy ($E_f$), the plots show calculations of $C_q$ vs. $E_f$ for various values of $T_0$. This corresponds essentially identically to the $C_q$ vs. channel potential, $V_{CH}$. Assuming a corresponding conversion factor of $T_0$ (K) = $\delta V$(mV)/0.15, where the scaling factor of 0.15 was determined empirically. The C-V characteristics are nearly identical in all cases. However a slight mismatch at higher disorder is observed, probably due to the stochastic nature of the calculation method in the random potential fluctuations as at higher disorder it is expected to not follow the Gaussian distribution any further and rather move to lognormal distribution [74], [78].

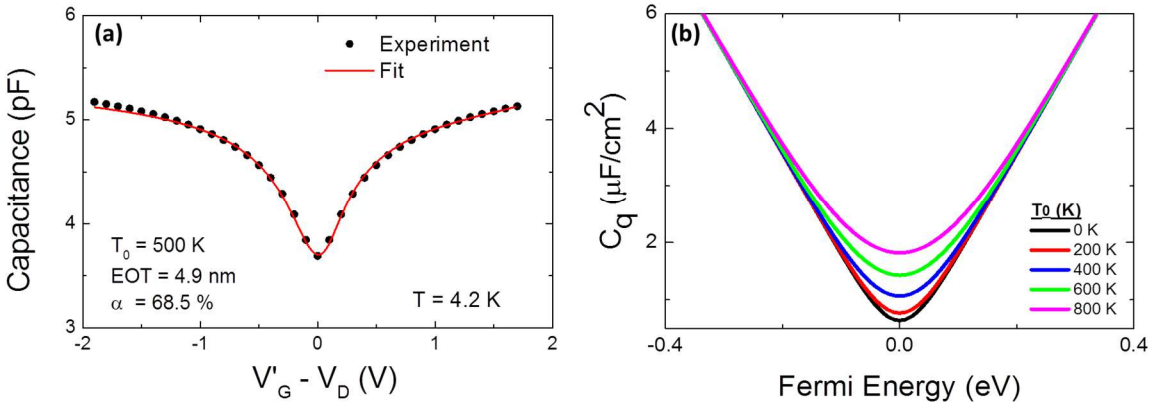


Figure 3-5: Random potential fluctuation model: (a) Fitting results of C-V curve at 4.2K, $T_0$ (random potential fluctuation parameter), α (area efficiency parameter) and EOT as are free fit parameters. (b) Quantum capacitance per unit area versus Fermi level at different effective temperatures ($T_0$).

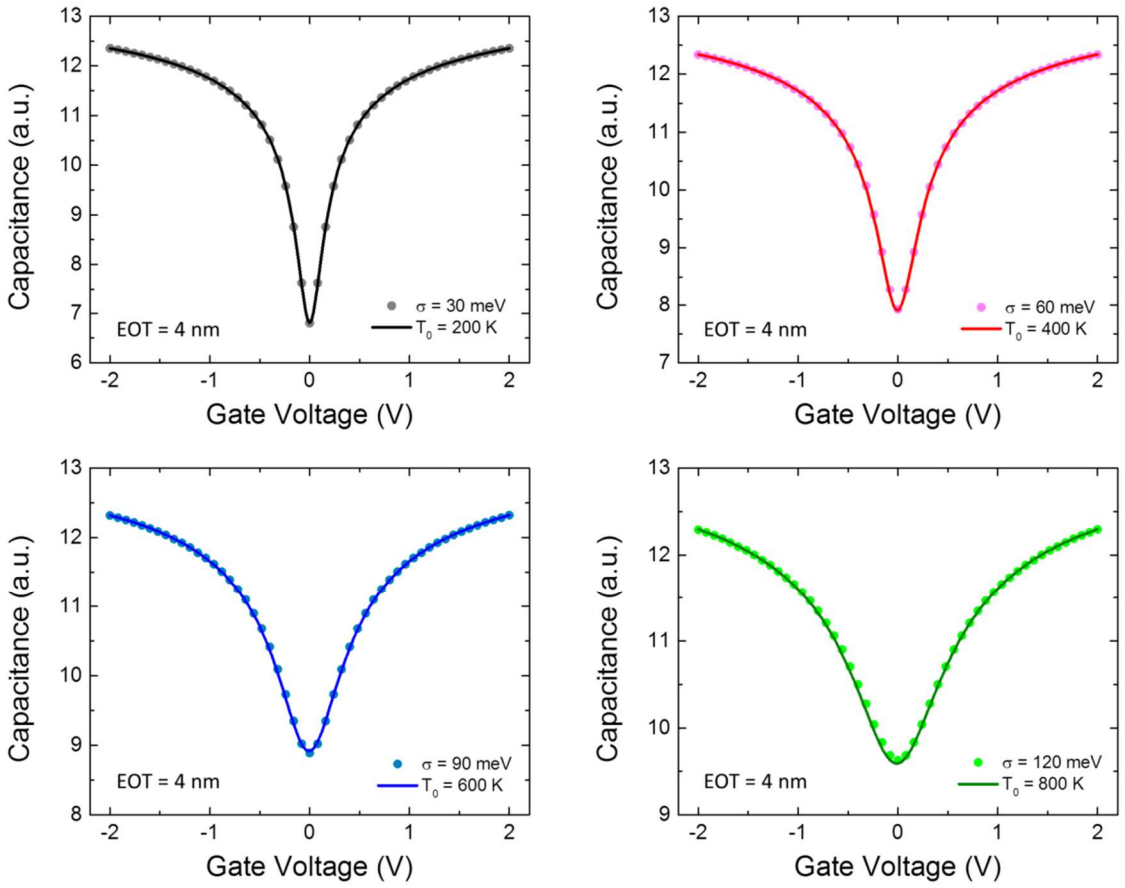


Figure 3-6: Plot of gate capacitance vs. gate voltage for metal-oxide-graphene capacitors with EOT = 4 nm at $T$ = 300 K. The plots compare the C-V characteristics using the effective temperature model where $T_0$ = 200 K, 400 K, 600 K, and 800 K, to the random potential fluctuation model for values of σ = 30 meV, 60 meV, 90 meV, and 120 meV.

### *3.2.3 Disorder in varactors with h-BN dielectrics*

In order to fully understand the effect of substrate roughness on the level of disorder in graphene, varactors with $HfO_2$ and h-BN gate dielectrics were compared. The motivation behind this study was inspired by the previous publications that described extremely-high motilities in graphene on exfoliated h-BN, which arises due to its crystalline nature and the low lattice mismatch between h-BN and graphene (only 1.8%) [79]–[81]. Since it is

difficult to obtain a large sheet of exfoliated h-BN, and align it on a back gated device, CVD h-BN was explored instead. The device fabrication process is similar to the ones used for $HfO_2$ devices. The CVD h-BN comes as a multi-layers (~13nm thickness) on a copper foil; therefore similar transfer process to the one used to transfer the graphene layer is used to transfer h-BN. Figure 3-7(a) shows a cross sectional cartoon of h-BN graphene field effect transistor (GFET) device. Figure 3-7(b) shows the measured gate capacitance versus gate voltage. The sweep window in the h-BN GFET shifted to more positive value in order to observe the Dirac point which occurs around 2.25V. The total capacitance and the capacitance tuning is less than they are in the $HfO_2$ because of the larger physical thickness of h-BN and lower dielectric constant.

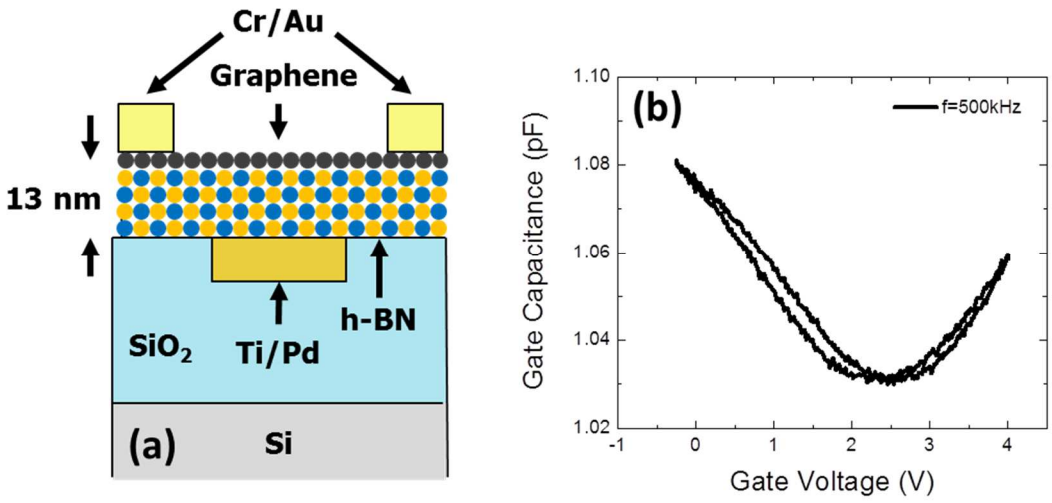


Figure 3-7: (a) Cross-sectional cartoon of h-BN back gated graphene device. (b) C-V plot for the device at 500 kHz and room temperature.

The CVD h-BN quality however, did not rise to the level of the exfoliated one. Figure 3-8(a) shows the h-BN has a short and long range roughness compared to $HfO_2$. The effect of the roughness on the disorder is quite noticeable. In Figure 3-8(b) shows how the level of disorder has almost doubled in the case of h-BN. Thus the overall roughness of the graphene form the way it conforms to the substrate surface [82]. The disorder

parameter, $T_0$, is higher in h-BN samples compared to $HfO_2$. This is probably strongly related to the higher roughness and crystalline defects in h-BN.

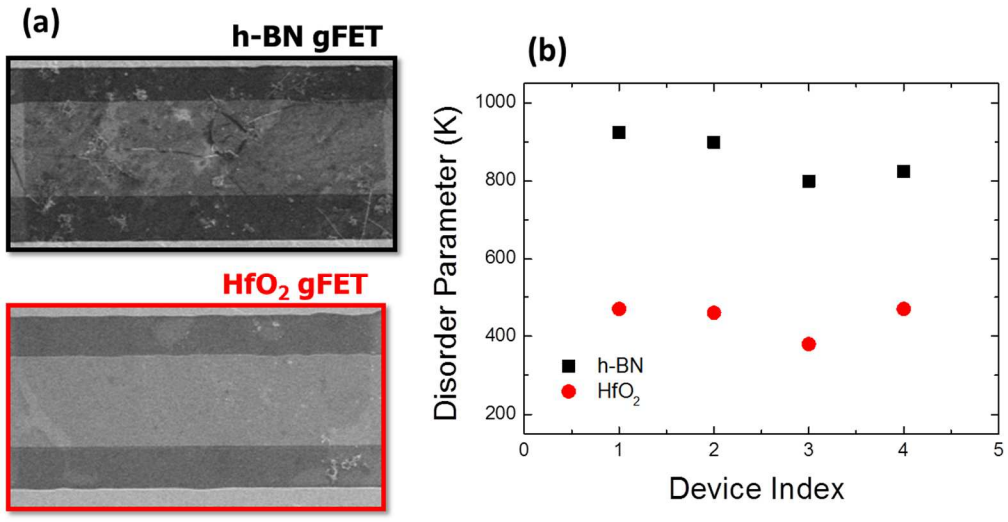


Figure 3-8: (a) SEM images for h-BN GFET (black), $HfO_2$ GFET (red). (b) Disorder comparison between h-BN and $HfO_2$.

Finally the random disorder effect in graphene can be represented as a voltage or as a rise in the effective temperature in the graphene sheet. Average density of state was predicated to increase in disordered graphene[82]–[84]. Some however has argued that the disordered graphene does not have higher quantum capacitance at the Dirac point [12], our finding contradict that. By comparing two samples (h-BN, $HfO_2$) in which the former has a rougher surface than the latter, showed that the rougher wrinkled surface has a higher disorder and a higher quantum capacitance than the smoother surface.

## 3.3 Area loss

### 3.3.1 Area loss

Transferring a single-atom-thick sheet of carbon onto a relatively rough surface is a challenging mission. In addition to the substrate roughness, the transfer process itself puts the graphene layer through a stressful process by "scooping" it from one beaker to another. At the final stage the graphene layer has to lay perfectly flat on the device buried gate. These stressful processes result in creating tears and breaks in the graphene sheet. Those tears and breaks make estimating the actual area of the devices harder than it is in traditional devices. Figure 3-9 shows the capacitance per unit area versus the applied voltage for several devices on the same sample. Ideally all the devices C-V curves should lie over each other. A non-negligible variation in the capacitance per unit area, however, is observed. This dispersion indicates that the area efficiency varies across the sample. Knowing the area is important for any further analysis needed on the system.

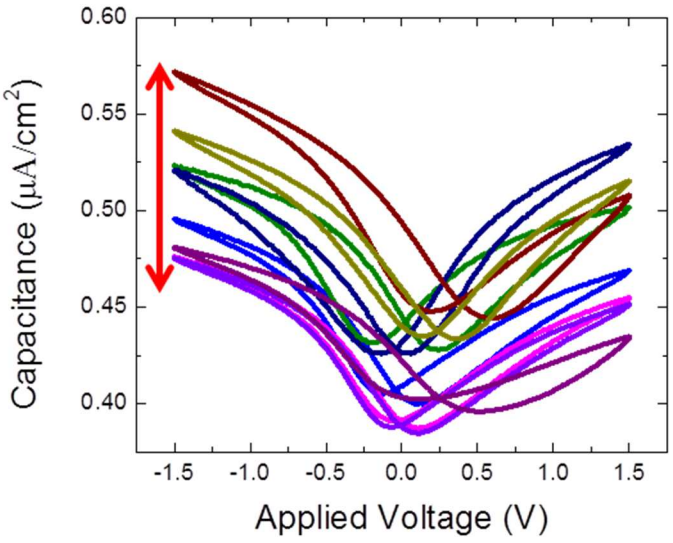


Figure 3-9: The C-V curves of several devices on the same sample plotted to show the area efficiency. The capacitance is scaled to the layout area.

Area efficiency was first obtained as a free fitting parameter in the random potential fluctuation model. Figure 3-10 shows the parameter α that represents the area efficiency. Later we found that we can better estimate the area by utilizing Raman mapping and taking SEM. The first method is time consuming method. The second method contains the risk of charging the oxide and therefore damaging it.

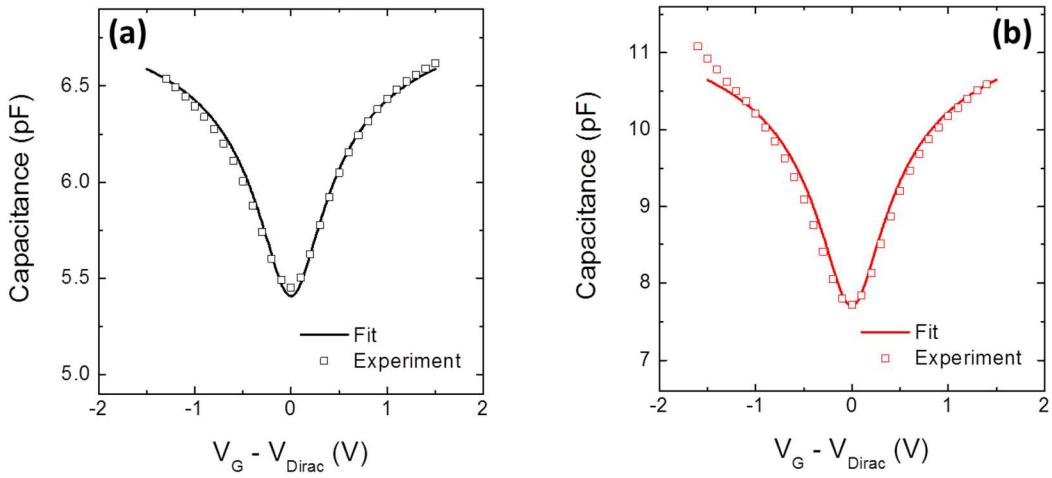


Figure 3-10: (a) Area Scaling Factor = 0.89, MIM EOT = 4.1 nm. (b) Area Scaling Factor = 0.60 MIM EOT = 2.7 nm.

### 3.3.2 SEM images

In order to estimate the effective graphene area in the devices, we used SEM to image the graphene sheet on the gate area. Imaging graphene in SEM can be difficult because it is very thin and has low *Z*, and generally low contrast. However we have found that cold field emission gun SEM (FEGSEM), with secondary electron detectors (one above the objective lens, the other below) is capable of taking clear images. Figure 3-11(a) and (b) shows two images taken on two GFETs with identical layout area. The sample was scanned at 2.5kV; the choice of the electron beam energy was based on clarity and the least risk of damaging the oxide. In the images shown in Figure 3-11(a) and (b), the graphene appears darker than the surrounding regions. One can see that the graphene

sheet is not continuous and the tears and breaks are obvious. Figure 3-11(c-d) plots the drain current ($I_D$) versus the gate voltage ($V_G$) for two GFET on the same sample. Though the FETs have the same channel length ($L$), and width ($W$), their drain currents values are quite different. The drain current in Figure 3-11(d) is roughly an order of magnitude higher than it is in Figure 3-11(c), and that is simply because the graphene area in Figure 3-11(b) appears to cover more than it is in Figure 3-11(a).

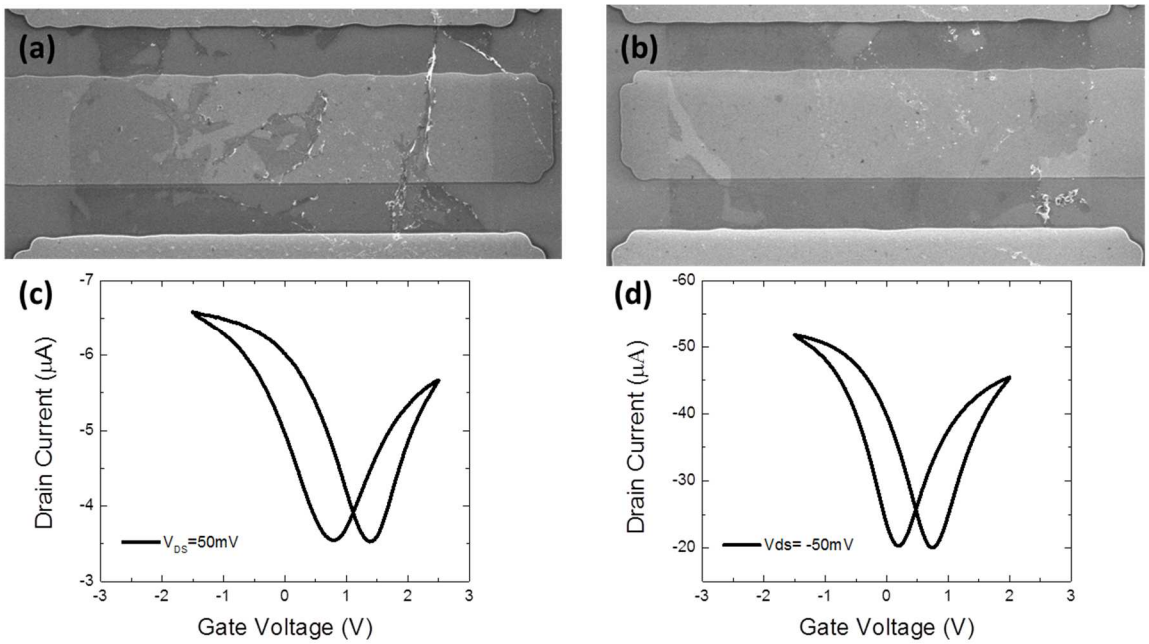


Figure 3-11: (a) and (b) SEM images for GFETs with the layout dimensions of $L$ = 10μm, $W$ = 40 μm. The images were taken at magnification on both images were 2000x. (c) is the $I_D$-$V_G$ for GFETs in (a), and (d) is the $I_D$-$V_G$ for the GFET in (b). Both devices are on the same wafer.

The field effect transistor performance can be affected by the reduction in the area, especially if the reduction occurs in the channel width. Tears that reduce the width of the device increase the access resistance which will lower the drain current, and degrade the overall FET performance. Furthermore, the uncertainty in the effective width of the device, makes the mobility extraction is rather difficult. Though the total area defines the total capacitance, the mobility is defined by the width. In other words, if the graphene

sheet at the edges of the gate is narrow, the access resistance will increase which will reduce the apparent mobility.

### 3.3.3 Raman Mapping

Raman mapping is used in order to make sure that the SEM has given us a clear idea of the graphene and in order to make sure of the graphene quality. As was shown in chapter 1 Raman spectroscopy in graphene has peaks that correspond to the sample properties. In Raman mapping, the microscope allows collection of a full spectrum at each spatial location in a matter of minutes. Thus complex spectral fingerprints can be rendered in images. The two distinct peaks for graphene namely the 2D peak occurring at~2700 $cm^{-1}$, and the G peak (1550 $cm^{-1}$) are plotted separately in an image that shows the points where those peaks are with significant counts [25], [29], [85]. The sample is divided into pixels and the scan spends 0.3 sec on each pixel (integration time). The scan can take from 40 to 120 minutes depending on the device layout area. The scan takes 3 points per 1μm and spends 0.3 sec per point. As can be seen in Figure 3-12, Raman mapping provides an excellent technique to determine the regions where graphene is intact versus regions where voids exist.

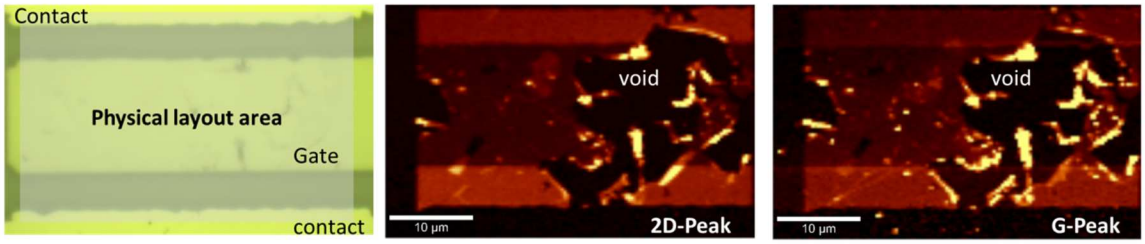


Figure 3-12: micrographic image of the device, Raman mapping to the 2D-peak and Raman mapping to the G-peak

## 3.4 Interfacial layer

### 3.4.1 EOT extraction

As seen from the random potential fluctuation section, knowing the EOT in these devices is crucial factor for modeling the graphene varactors. Ideally the oxide capacitance of the metal-oxide–graphene (MOG) device should dominate away from the Dirac point and thus the EOT can be estimated by assuming that the maximum capacitance is indeed the oxide capacitance. This assumption should be reasonable as long as the maximum capacitance is measured away from the Dirac point and normalized to the correct area. As our methodology is based on utilizing a local back gate design, in which the MIM devices have *the same dielectric* as the MOG devices. Thus the extracted EOT from the MIM by utilizing equation 3-4 for a fixed area of (1000μm$^2$) should match perfectly with the one extracted from the MOG on the same sample. It does not match, however, even after taking the area loss into account. Figure 3-13 shows the difference between the two devices is significant and beyond the measurement error margin.

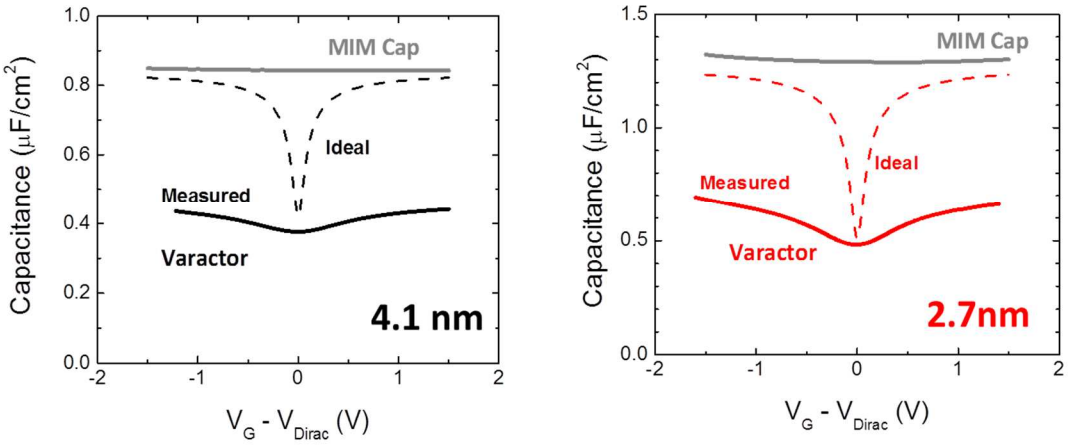


Figure 3-13: Comparison of the varactors capacitance per unit layout area to the MIMs capacitance per unit area in two different samples with EOT values of 4.1 nm and 2.7 nm (extracted from MIM capacitors).

Figure 3-13 shows the capacitance per unit area for measured varactors compared to both the ideal varactor and the MIMs devices. This disparity in the EOT was puzzling. Moreover the difference between the extracted EOT from the MIM and the varactors varies from one sample to another. A residual interfacial layer in the MOG devices was doubted to be the reason behind the disparity. CVD Graphene goes through manual aqueous transferring process in which the chance of having residues is possible. Residues such as copper from the copper foil or $Fe_2Cl_3$ from the etchant solution could be found after the transfer. By utilizing both EDS and Auger spectroscopy, no unexpected elements were detected. Figure 3-14 shows some EDS results and Auger spectroscopy. Those results indicated that if there was some residual from the transfer process it is not a continuous layer that has a significant thickness.

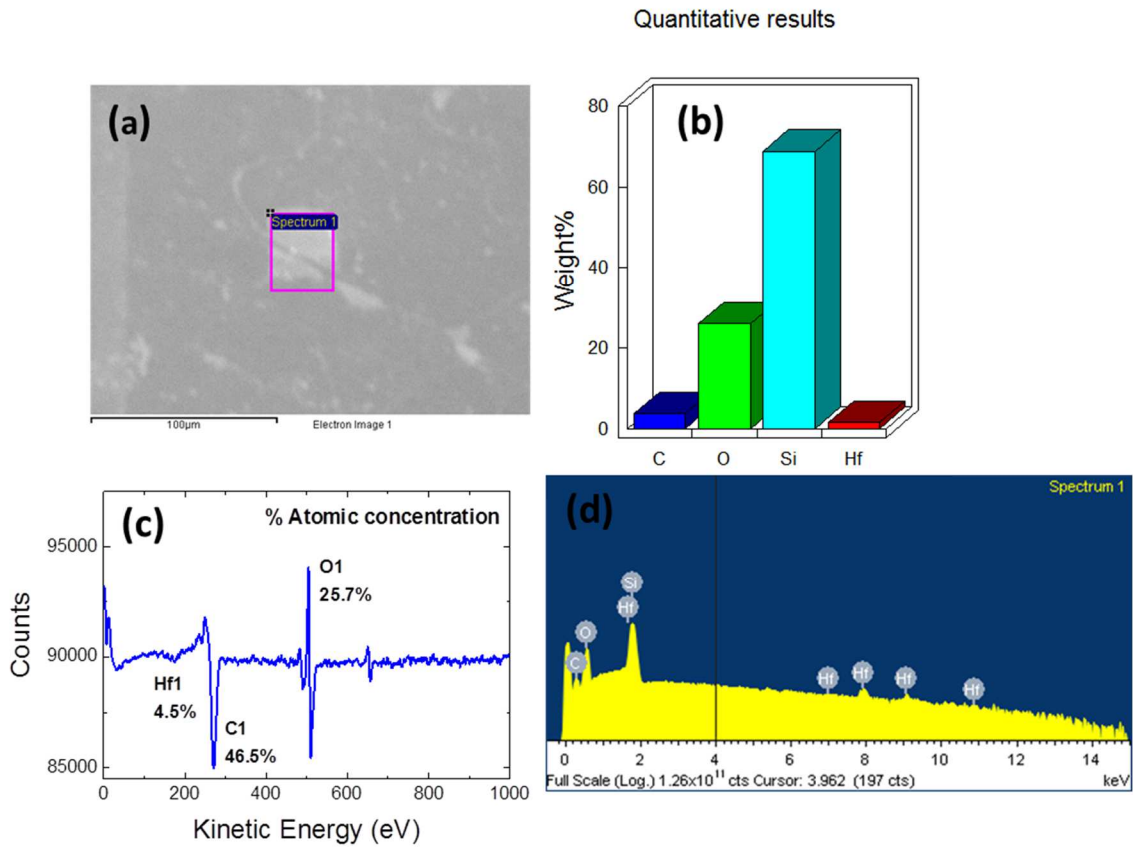


Figure 3-14: (a) SEM image of transferred graphene on $HfO_2$ gate oxide. (b&d) EDS counts for the atoms on the surface. (c) Auger spectroscopy result on the same sample.

The use of scanning tunneling microscopy (STM) imaging by other groups indicates a spatially dependent perturbation in the graphene sheet that is laying on a dielectric surface. As was described before, graphene has a non-uniform charges density distribution as a result of the graphene conformation to the surface terrain. These non-uniform charges have more effects than random potential fluctuation. In other words non-uniform surface potential distributions will perturb the graphene interaction with the substrate. That interaction could manifest itself in either attraction or repulsion based on the distribution of charges on both sides. As those charges affect the mobility, they with no surprise affect the distance between the graphene and the substrate [86], [87].

Reference [87] reveals through theoretical work based on an ab initio investigation on graphene/$HfO_2$ system, a gap between an amorphous pristine $HfO_2$ and graphene sheet as Figure 3-15(b) depicts. The distance between the two should be 3.29 Å with adsorption energy of 23 meV/ $Å^2$. However in the case of oxygen vacancies the distance reduces to 3 Å with an increase of the adsorption energy to 33 meV/ $Å^2$. Those values are slightly smaller than it is in $SiO_2$ case which shows that the graphene is more attracted to the $HfO_2$ than it is to the $SiO_2$. The most interesting case in here is the oxygen vacancies case, as it is probably more challenging to obtain a pristine $HfO_2$. The results presented in reference [87], agrees with our observations. It is hard to experimentally define the number of oxygen vacancies; however their doping effect is very prominent. The graphene on $HfO_2$ with oxygen vacancies is expected to appear n-type [78], [87]. The theoretical study on the graphene/$HfO_2$ interface showed that their intrinsic electronic structure was left unchanged. Therefore and despite the stronger interaction with $HfO_2$, the graphene only bonded to the $HfO_2$ via Van der Waals. This lack of a strong bond between graphene and the oxide such as $HfO_2$, and the Van der Waals bonds dictate certain distance between the two. Although this distance is physically ~3Å, but in terms of EOT it is more than 1 nm since the vacuum dielectric constant is about 1. That means the difference between the MOG and MIM devices are not just the replacement of the top metal electrode with graphene, but also the dielectric between the two electrodes. As we learned from the beginning of this chapter, the effect of area loss and the EOT values could be confused together; so when we scale the capacitance per unit area the choice of that area might affect our estimation of the EOT differences. Therefore in order to empirically extract the EOT difference, only devices with high area efficiency were considered. Figure 3-15(a) shows a plot of EOT values extracted from both MIMs and MOG versus the expected EOT from the physical thickness of the oxide. MIMs EOT pretty much match the expected EOT. However in the case of MOG there is quite a difference. The red straight line is drawn just beneath the ones that have the lowest EOT.

The devices that are located away from the red line have a high apparent EOT due to their low area efficiency. The intercept of the red line with the y axis is the estimated gap and it is about 1.1 nm which matches perfectly with the expected vacuum of physical thickness of 0.33nm.

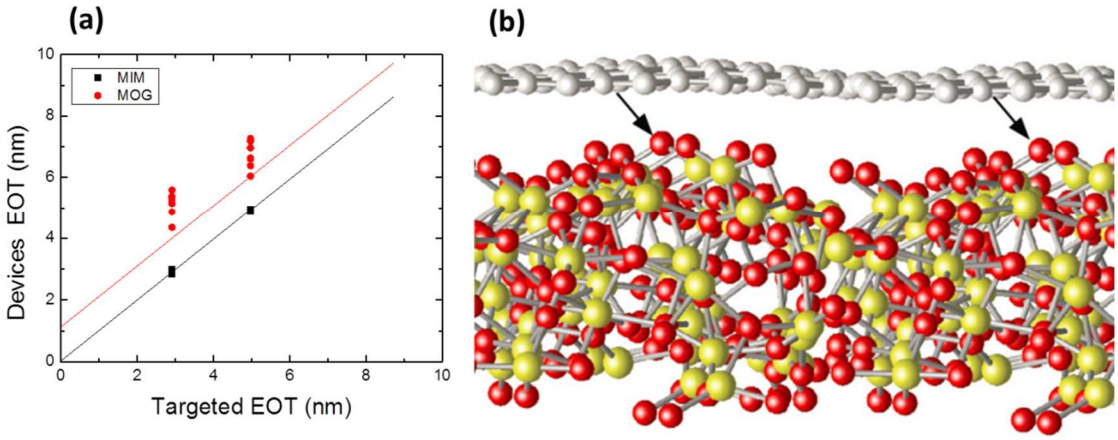


Figure 3-15: EOT disparity (a) experimental data that empirically extract the gap. (b) The relaxed atomic structure of graphene adsorbed on the $HfO_2$ surface G/$HfO_2$. The gray, red, and yellow spheres represent the atomic species C, O, and Hf, respectively [87].

### *3.4.2 Tuning range*

The tuning range (TR) can be simply defined as the ratio between the maximum capacitance (away from the Dirac point) to the value of the minimum capacitance (at the Dirac point) in C-V curve at certain frequency. Because the MOG devices are fabricated for the purpose of being variable capacitors (varactors), the tuning range value is a crucial factor. It is a measure of the device quality, and a reflection of both the disorder and the EOT. It is a reflection of the disorder because the minimum capacitance is dominated by the quantum capacitance, while the EOT defines the maximum capacitance. Increasing the TR can be achieved by decreasing the quantum capacitance (the minimum), increasing the value of the oxide capacitance (the maximum), or both. The former is related to reducing the disorder which will help in diminishing the density of state thus

the quantum capacitance reaches a finite minimum [11], [13], [16], [88]. Since the disorder comes from various sources, it is hard to control it [11], [74], [88]. The latter option is to increase the oxide capacitance which can be achieved by decreasing the oxide thickness or in other words reducing the EOT. It was theoretically determined before that a high capacitance tuning ratio in metal-dielectric-graphene capacitors needs an effective oxide thickness (EOT) values ~ 1 nm. The high capacitance tuning, also called the tuning range, is the ratio of the maximum capacitance to the minimum. As the tuning range increases the slope of the C-V curve increases; this slope is crucial for the success of the passive wireless sensor. The effect of the oxide thickness on the steepness of the C-V curve has been explored. The theory expects the tuning range to increase as the EOT decreases. A comparison of the normalized C-V curves for both samples at room temperature is shown in Figure 3-16 (a) where the varactor normalized total capacitance plotted versus applied voltage for three samples with three different oxide thicknesses. The oxide thickness was estimated based on metal-insulator-metal structures (MIMs). The gap was not accounted for because of the difficulty in estimating it from one sample to another [87]. The results show that the capacitance tuning range increases as $HfO_2$ thicknesses decreases, as expected. The EOT scaling study resulted in tuning range increase from 1.22-to-1 to 1.50-to-1 by scaling EOT from 4.1 nm to 1.9 nm [77]. The leakage current in all the samples was negligible; therefore the maximum capacitance increase is not a result of leakage increase. The measurement of the leakage is important because our capacitance measurement model is Cs-Rs and that assumes a negligible leakage. Therefore Figure 3-16(b) assures a confidence in that assumption. However both the tuning range and the total capacitance were less than expected based EOT values determined from MIM-capacitors [77]. The increase in the tuning range (TR) does not mirror the decrease in the EOT. The question that pertains *is what is the relationship between the EOT of the system and the tuning range?* Ideally the tuning range should increase linearly with the decrease of the EOT ($TR$ α $\frac{1}{EOT}$ ) assuming everything else is

the same between the two compared samples. That however is not the case as shown in Figure 3-17 the scaling does not seem to follow a linear trend. TR is a complicated issue. It does not depend only on the EOT scaling but also on the graphene quality. The strayed data points in Figure 3-17(a) are the ones from two different patches of graphene and the oxide was deposited at different times. Therefore the samples are not expected to follow the same trend because they are not from the same run. The graphene quality for the most part will affect the minimum capacitance. On the other hand since the $HfO_2$ was deposited at different times, the oxygen vacancies density could also be different and that will affect the EOT in the MOG devices only.

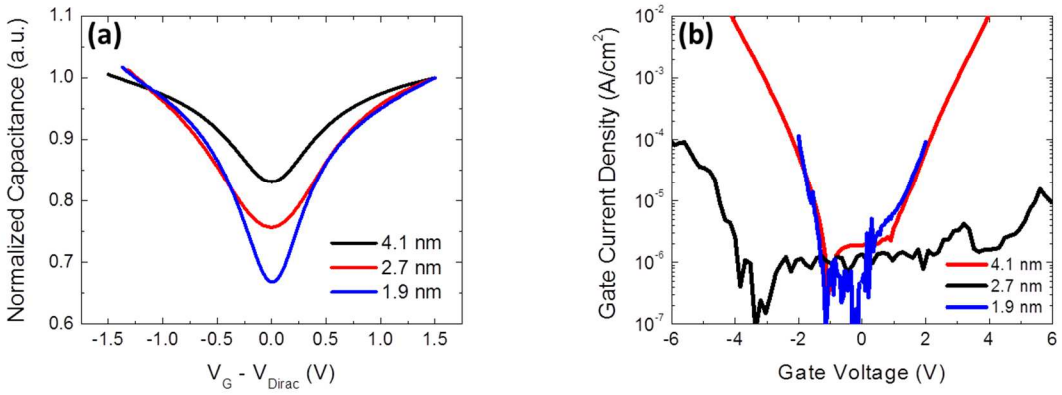


Figure 3-16: (a) Tuning range increases with the EOT scaling. (b) The leakage current measured in all the samples.

Furthermore Figure 3-17(b) shows statistics across several devices on three different samples that have the same graphene and were fabricated at the same time. The TR seems to follow sort of a linear trend in this case. The statistics across multiple samples reveal that the relationship between the TR and the EOT is far more complex than what was anticipated. In another words the decrease in the EOT does not necessarily increase the tuning range by the same factor. These observations lead to an empirical belief that the actual effective dielectric thickness in the MOG systems are somehow different from the

effective oxide thickness in the MIMs which will explain that reducing the physical thickness of the $HfO_2$ ($<EOT_{MIM}$) does not result in smaller $EOT_{MOG}$.

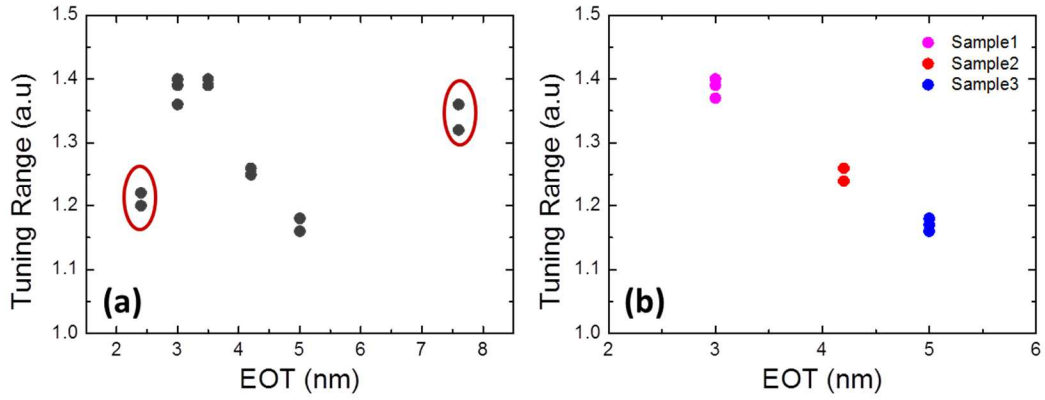


Figure 3-17: Tuning range versus EOT. (a) Devices with graphene sheets from different sources. (b) Three different devices with graphene sheets from the same source.

## 3.5 Slow traps

### 3.5.1 Hysteresis

Slow traps are traps DC charged or accessible traps in the oxide. They get charged through tunneling during the DC sweep and they cause a shift to the Dirac point in the case of the graphene device, but in MOS case they cause a shift in the threshold voltage which will lead to the hysteretic effect. As the back sweep or down sweep will start from a different Dirac point the whole curve is shifted to the right or the left depending on the type of the traps. It is known that $HfO_2$ is a hysteric dielectric and many treatment methods were proposed to treat this behavior. The sources of those traps are defects in the dielectric from the growth process [89], [90]. In both varactors and GFETs the hysteresis is measured in volts ($\Delta V$) as the difference between the two Dirac points in the C-V and $I_D$-$V_G$ respectively. At GFETs the hysteresis value in both curves are identical as shown

in Figure 3-18. The hysteresis value depends on several variables, such as the growth conditions of the oxide, the type of the oxide, the sweep window and the temperature. However the latter is not a typical variable for hysteresis. To further understand the system Figure 3-19(a) shows a plot for several devices MIMs and MOGs on different samples, where each color refers to different devices on the same sample.

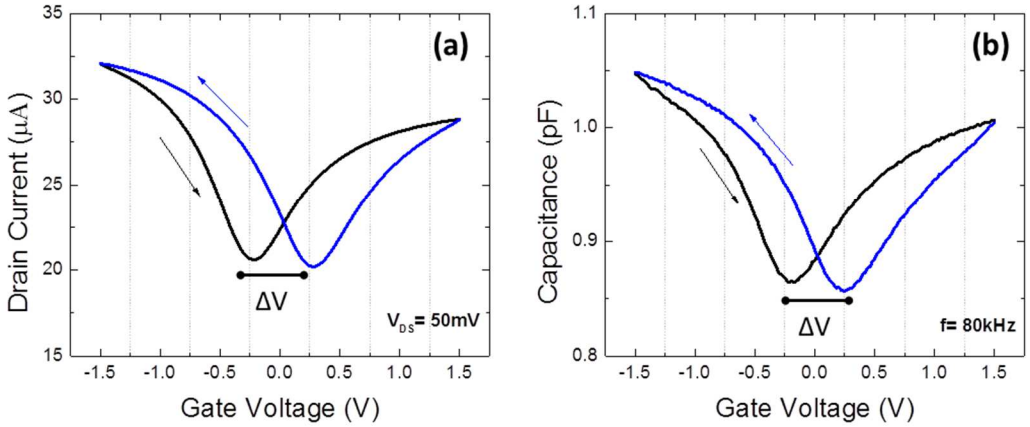


Figure 3-18: The hysteresis value in the $I_D$-$V_G$ curve is very similar to the one in the $C_G$-$V_G$ curve. (a) The $I_D$-$V_G$ curve is taken at $V_{DS}$ = 50mV. (b) The $C_G$-$V_G$ curve is taken at f = 80 kHz.

The plot in Figure 3-19(a) shows the hysteresis pattern as the EOT increases in both MIM and MOG devices from several samples. The MIMs devices with different oxide thicknesses follow the intuitive trend of increasing the hysteresis as the oxide thickness increases. The MOGs devices data on the other hand seems to be more scattered. The non-linear trend in the MOG data is probably because the MIM oxide and the MOG oxide do not have the exact same dielectric though they are on the same sample. The gap between the graphene and the $HfO_2$ is the main difference. It is very likely that this gap will affect the hysteresis. In addition the hysteresis values are mostly higher in the MOG than they are in MIM devices. Even when the hysteresis value is zero in MIM device, the MOG is not on the same sample that means this particular hysteresis value is related to the vacuum gap in the graphene devices. Moreover the hysteresis by definition is

temperature independent since it is a DC electrostatic affect that depends on the number of states in the oxide and the sweep window. Figure 3-19(b) shows the MIM hysteresis relative independent however, the hysteresis in MOG devices shows a temperature dependence. The hysteresis in the MOG devices increases as the temperature increases. The drop in the hysteresis in MIM2 is probably due to a slight increase in the leakage.

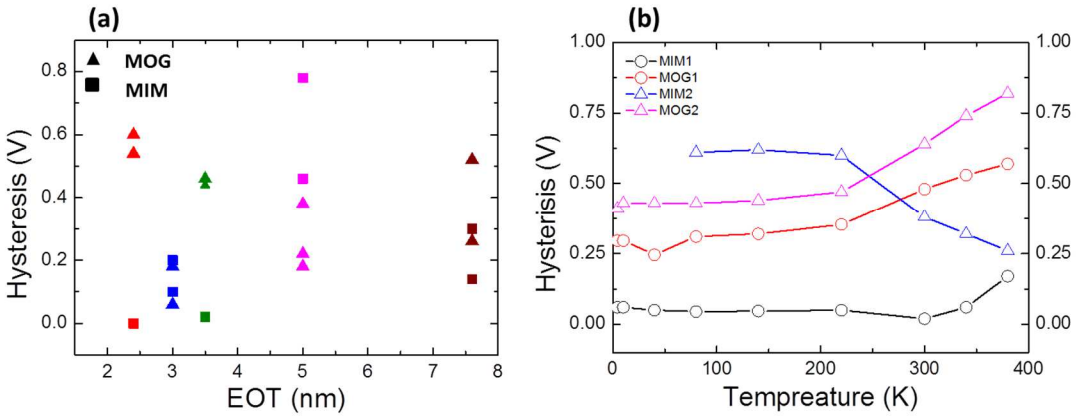


Figure 3-19: Hysteresis comparison between MIM and MOG devices. (a) Hysteresis versus EOT distribution across several samples. (b) Hysteresis in both MOG and MIM devices versus temperature for two different samples.

In conclusion the difference in the hysteresis behavior between MIM and MOG devices is an indicative of the fundamental difference between the two systems rather than the graphene sheet addition. Graphene is semi-metal and it is not a hysteric material as it does not trap any charges. The fundamental different however comes from the gap between $HfO_2$ and graphene.

# Chapter 4 :
# Border Traps

*"All materials (including conductors) possess the so-called quantum capacitance, which is present in series with the traditional geometric (electrostatic) capacitance. It is usually a large positive quantity and therefore irrelevant for most materials except for nanostructures." Y. Hanlumyuang et.al The Minerals, Metals & Materials Society Quantum, 2014.*

## 4.1 Introduction

### 4.1.1 Traps background

Recent advances in the fabrication of graphene devices have led the need to understand its interfacial properties. One of the most important interfaces is the graphene-dielectric interface. The challenge of growing a dielectric with defect-free interface is well known. Oxide semiconductor interfaces such as $Si/SiO_2$ or III-Vs $/HfO_2$ have been intensively studied in the past [91]–[96]. The main conclusions of that work can be summarized as follows. (1) Oxides can have various types of defects such as structural defects, oxidation process defects, or metal impurities. (2) Those defects can act as trap sites in the oxide band gap that could be negatively or positively charged. Some of the traps that are close to the surface (surface traps) can be treated by post annealing in an inert gas. The deeper ones however are harder to treat and they mostly remain and degrade the performance. The trap sites are spatially distributed in energy. The closer they are to the edge of a band the faster in responding to the applied potential by charging and discharging. For instance mid-gap traps are the slowest while band edge traps are the fastest [89], [97], [98]. The interface trap density in Si and other bulk semiconductors can analyzed with conventional methods such as Terman method or the conductance method. The Terman method relies upon analysis of the "stretch-out" of the C-V characteristic, while the conductance

method analyzes the magnitude and time constant of dissipation caused by the trapping/detrapping process [99]. Gapless two-dimensional material with low density of states such as graphene are more challenging to fit into these conventional models [100]–[103]. Though the bottom gate configuration in MOG devices provides a better quality dielectric than top-gated configuration, the dielectric ($HfO_2$) is still imperfect and some level of defects remains [57]. The nucleation on top of graphene is inherently problematic due to its inert nature process. In GFET devices the density of interface traps (*Dit*) extraction was performed using a technique similar to the Terman method [99], where the stretch out of C-V curve relative to the ideal case is used to determine the interface state density. This approach was applied in reference [52] on a back gated GFET with $HfO_2$ as a gate oxide at only one frequency (100kHz). The difference between the measured C-V curve and the ideal is considered $C_{it;}$ as shown in Figure 4-1, this extra interface capacitance is modeled to be in parallel with the quantum capacitance. In addition to the fact the approach in [52] did not investigate the C-V curve at multiple frequencies, the reference did not address the way the ideal C-V is calculated. The ideal C-V curve in graphene devices depends on far more parameters than just interface states as was demonstrated in the previous chapter. Conventional "stretch-out" techniques such as Terman method work somewhat well for MOS caps because the transition always goes between two *well-known* values ($C_{ox}$ to $C_{min}$). However for graphene, other non-idealities could also affect the minimum capacitance, therefore the conventional stretch-out techniques do not work well. Furthermore, the inert nature of graphene makes it lack dangling bonds; therefore the possibility of having interface traps at graphene/$HfO_2$ interface is very low. Border traps however are expected to be the dominant traps that affect the C-V characteristic. Therefore the rest of the chapter will focus on border traps analysis.

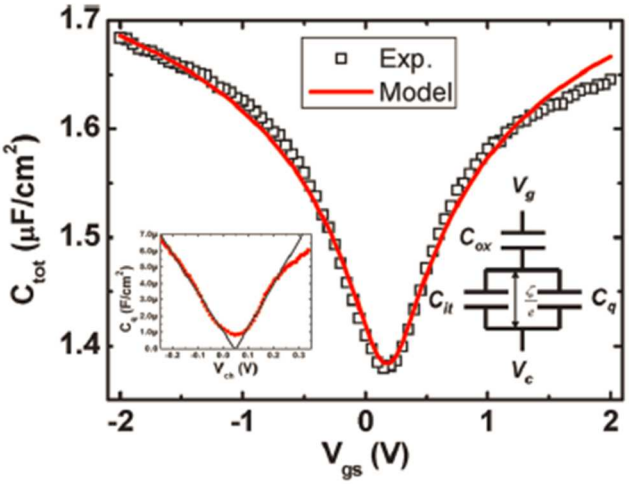


Figure 4-1: Total capacitance as a function of gate voltage. The inset shows extracted $C_q$ as a function of the graphene channel potential ($V_{ch}$), and the circuit model of the system [52].

### 4.1.2 $HfO_2$ border traps

$HfO_2$ is considered the best candidate for further scaling of the MOSFET technology due to its high K-dielectric constant that guarantees lower leakage than $SiO_2$, while maintaining a low EOT value. In our varactor applications still the very high K-dielectric constant is a desirable trait for another purpose, namely to increase the capacitance tuning without increasing the leakage. $HfO_2$ however is also known for having traps. Those traps were observed before in C-V and pulsed $I_D$-$V_G$ measurements [94], [95]. It was demonstrated previously that there is a tunneling mechanism occurs between the Si and $HfO_2$ in MOSFETs [104]. The exchange of charge occurs between the charges at the silicon interface and the traps in the $HfO_2$. A charge pumping technique study on Si/$HfO_2$ boundary showed that the transient time for charging and discharging can be observed at wide range from $10^{-8}$ to $10^{-4}$ seconds [95]. Therefore it is very conceivable to observe similar trapping mechanism at 5-500 kHz frequency range. Unlike slow traps that cause hysteric effect with the DC window sweep, border traps are AC measurement consequence, they exchange charges within the applied frequency. The lower the applied

frequency, the deeper the tunneling occurs and hence the apparent thickness of the oxide will be reduced, resulting in an increase in the total capacitance.

In graphene, high dielectric devices, we expect border traps to be the dominant trapping mechanism due to the lack of dangling bonds. Border traps are a type of bulk traps that are near the interface, they were given this name to distinguish them from interface states and other oxide traps [95], [104], [105]. Those traps are distributed spatially across the oxide.

Border traps have been studied before in MOS capacitors systems and they usually manifest themselves as an excess capacitance in comparison with the oxide capacitance. This excess capacitance increases as the frequency decreases. It's commonly modelled as a capacitor in parallel with the oxide capacitance [104][94], [106]. Our analysis methodology is based on utilizing a local back gate design. Thus both devices namely; metal insulator metal (MIM) and the metal insulator graphene (MOG) have the *exact same* oxide as shown in Figure 4-2. Because the $HfO_2$ is deposited on top of the gate metal, the only difference between the two devices is the electrode layer on top of the oxide. That allows us to distinguish between the non-idealities relating to the oxide-graphene interface from the ones in the oxide itself. Once again it is important to distinguish between slow traps that were studied in the previous chapter and border traps. Slow traps are DC traps that stretch out the C-V curve, but they mainly cause a shift in the Dirac point which results in hysteresis. There is a hysteresis correction that can be applied whenever the hysterics value is significant. The border traps on the other hand are only observed in a small signal measurement and they shift the C-V curve up i.e. an increase in the total capacitance.

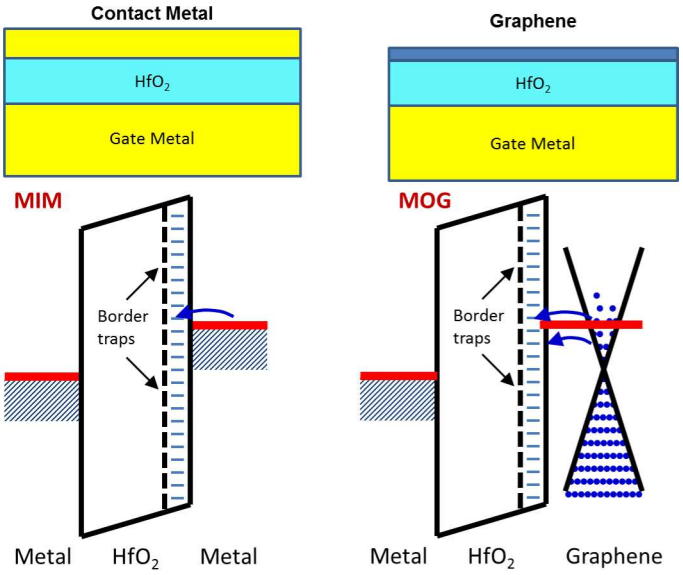


Figure 4-2: Cross-sectional cartoon shows the similarity between the MIM and MOG systems and below them is the Energy band diagram for both devices. The border traps are distributed uniformly in energy. The blue arrows indicated the tunneling mechanism.

Though the dispersion varies from one sample to another, it is almost identical between the different structures (MIM and MOG) on the same sample. The Frequency dispersion shown in Figure 4-3 was the first clue that led us to think about border traps. The similarity in the dispersion between the two devices in Figure 4-3 is an indctive of a common source behind this disperison, in other words the $HfO_2$ layer. The variation among different samples however could be related to the quality of the oxide and the graphene [107].

A second clue was found from the DC measurements. The shift in the Dirac point in graphene is an indicative of doping since the expected value for the Dirac point for graphene on Pd gate is +0.6; however in vacuum the Dirac point has been always less than that which is an indicative of the effect of the oxide defects on the graphene [78]. Since there is no actual bond between the graphene and the dielectric, the doping is a

result of the energy position that the graphene occupies relative to conduction or valance band of the dielectric [87].

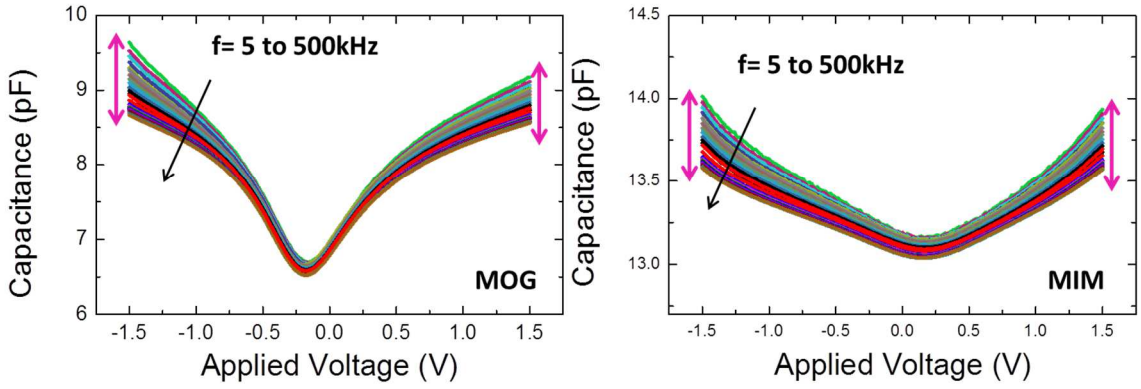


Figure 4-3: Capacitance versus voltage at frequencies from 5 kHz to 500 kHz for MOG and MIM device.

Those bands provide free carriers that potentially can dope the graphene. However as can be seen in Figure 4-4 graphene sits in the middle of the energy gap of $HfO_2$ that means $HfO_2$ adds no states above and below Fermi-level in graphene. Therefore the doping affect is a result of trap states in the $HfO_2$ band gap. The oxygen vacancies in the $HfO_2$ work as donors and shift the Dirac point back to zero [87]. Our collaborative work with a theoretical research group in Illinois shows the effect of those vacancies on the Dirac point. Some of their finding from first principle density functional theory (DFT) calculations is summarized in Table 1. The effect of oxygen vacancies and oxygen molecules on varactors performance will be discussed in detail in the coming chapters.

| **Sample** | **Pd/$HfO_2$/G** | **Pd/$HfO_2$ (VO1)/G** | **Pd/$HfO_2$ (VO2)/G** | **Pd/$HfO_2$ (VO4)/G** |
|---|---|---|---|---|
| **Dirac point** | +0.6 | +0.27 | -0.32 | -0.59 |

Table 1: Frist principle calculation from Aluru group to illustrate the effect of oxygen vacancies on the Dirac point [108].

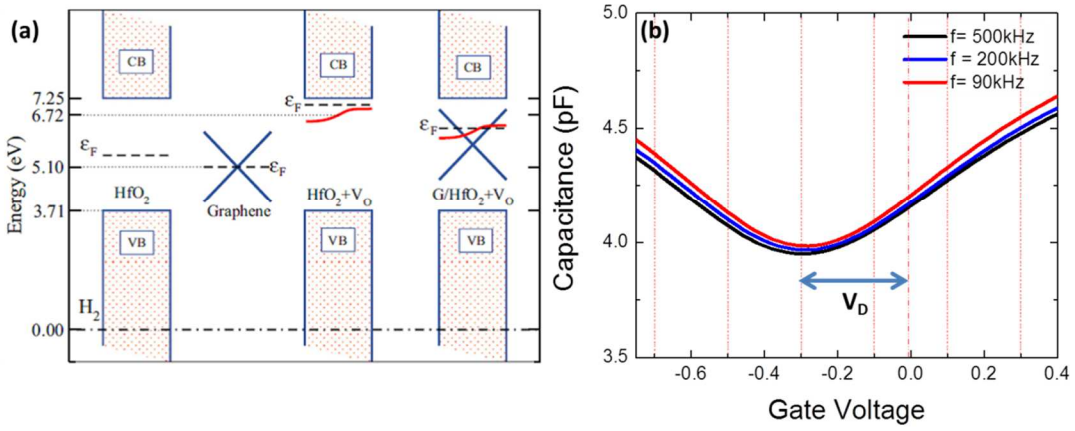


Figure 4-4: The effect of oxide traps on the Dirac point. (a) (Color online) Schematic energy diagram for isolated systems, (left) $HfO_2$ surface, and graphene sheet, (center) defective $HfO_2$ surface ($HfO_2$ + VO). (Right) Graphene adsorbed on the $HfO_2$ upon the presence of VO (G/$HfO_2$ + VO). Dashed lines represent the Fermi energy for each system calculated separately, and the solid (red) line represents the VO impurity level. The horizontal dot-dashed line is the energy position of the common reference for the $H_2$ molecule level [87]. (b) The Dirac point has negative value at different frequencies.

## 4.2 Border trap density extraction

### *4.2.1 Border traps model*

Border traps are arguably a problem that related only to the oxide. In the case of MOG devices the graphene can be replaced with a layer of metal with the same work function, and similar results should be obtained. Therefore the total gate capacitance in both MOG and MIM devices is treated the same, which is accurate as the same frequency dispersion is observed in both structures. Furthermore border traps have larger time constant, therefore it can be observed within frequency range (5-500 kHz). In case there was interface traps at graphene-$HfO_2$ boundary at some defect or edge sites in graphene, they cannot be observed within our frequency range. Due to the absence of band gap in graphene the trapping and de-trapping at the interface happens so fast that a much higher applied frequency is needed to observe them. The increase in the device capacitance

(excess capacitance) with the decrease in frequency was observed before in $HfO_2$ on Si-MOS capacitor. Reference [104] modeled the border traps as an extra capacitance in parallel with the device capacitance as in Figure 4-5(a). In reference [104] their model analysis depends on the slope of the capacitance versus log frequency. Figure 4-5(b) depicts their results. In this chapter similar approach was followed, and a good estimate of the border traps density per volume per energy was obtained.

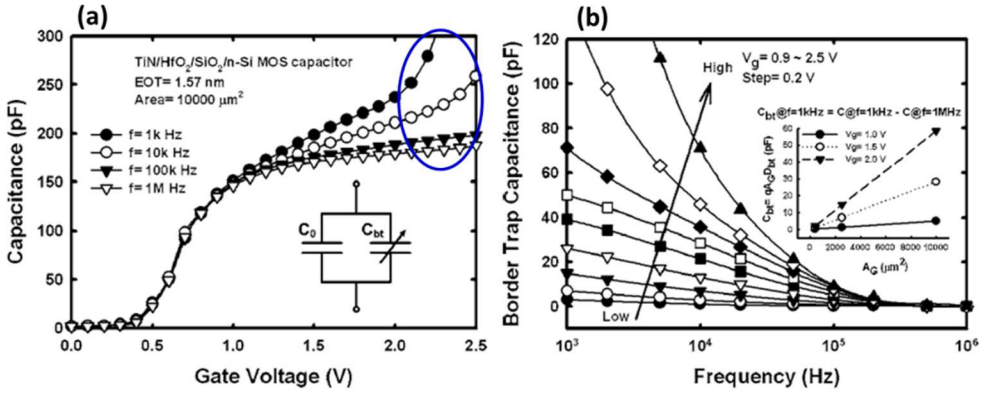


Figure 4-5: (a) Border traps behavior is observed in $HfO_2$ MOS capacitor, simple RC circuit model is in the inset. (b) Extracting the traps density from the slope of the gate capacitance versus log frequency [104].

Several groups have modeled border traps with RC circuit, either with a lumped simple model or a distributive comprehensive model. The Distributive model is more accurate than a lumped circuit border traps model because it accounts for spatial distributive nature of traps across the oxide. The oxide thickness in the distributive model case is divided into much smaller thicknesses called $\Delta x$ where $\Delta x << t_{ox}$, and each one of those thicknesses represents $\Delta C_{ox}$ which is in parallel border traps capacitance ($\Delta C_{bt}$), and the sum of all the branches are in series with semiconductor capacitance ($C_s$) for MOS systems. While more complex border trap models gives more accurate estimate of the border traps density, a simpler model is utilized in here to provide a basic understanding of the trapping behavior. The lumped circuit model that we utilize is similar to the distributive model but simpler. Instead of dividing the oxide thickness into $\Delta x << t_{ox}$, our

model assumes $\Delta x = t_{ox}$. Therefore there is only one border trap capacitance $C_{bt}$ which is in parallel with the gate capacitance as shown in Figure 4-6. The model was simplified to avoid numerical analysis for the multi-branches circuit. The following model analysis is based on the model presented in references [104], [109]. In this model the $C_{bt}(x)$ is at $\Delta x = t_{ox}$. Time constant associated with the charge exchange is $\tau$ and is defined as

$$\tau(x) = \tau_o \, exp(2\kappa x), \qquad 4\text{-}1$$

where $\kappa$ is the attenuation coefficient and $\tau_o$ is inversely proportional to the charge density at the graphene surface.

$$\kappa = \sqrt{2m^* \left(\frac{E_{CO} - E_F}{\hbar}\right)}, \qquad 4\text{-}2$$

where $m^*$ is the effective mass of the $HfO_2$ , we can define $C_{bt}$ as

$$C_{bt} = (q^2 N_{bt} t_{ox}) * A, \qquad 4\text{-}3$$

where $N_{bt}$ is the density of border traps per volume per eV, $A$ is the device area. The measured data can be linked to density of border traps through the border traps capacitance. The following equation defines the relationship between the $C_{bt}$ and $N_{bt}$

$$N_{bt} = \frac{\partial C_{bt}}{\partial \ln(f)} \left(\frac{\sqrt{2m^*(E_{CO} - E_F)}}{\hbar}\right) \frac{1}{q^2 A}. \qquad 4\text{-}4$$

As we can see from equation 1-2 the slope of the total capacitance versus natural logarithm of frequency in fact is function of the density of the border traps. One can rewrite equation 4-4 as

$$N_{bt} = \frac{\partial C_{gate}}{\partial \ln(f)} \left(\frac{\sqrt{2m^*(E_{CO} - E_F)}}{\hbar}\right) \frac{1}{q^2 A}. \qquad 4\text{-}5$$

Since $C_{bt}$ is not a measured quantity one can replace it with the $C_{gate}$. This replacement is acceptable because neither the $C_{ox}$ nor the $C_q$ are function of frequency so the slope of the curve does mainly depend on the $C_{bt}$. Moreover this model assumes a constant barrier height; therefore it ignores the Fowler-Nordheim approximation. In other words this model assumes that the Fermi-level in graphene does not move by a significant amount that would cause a considerable change in the barrier height. Therefore it is a fixed barrier height tunneling model as shown in the energy band diagram in Figure 4-6.

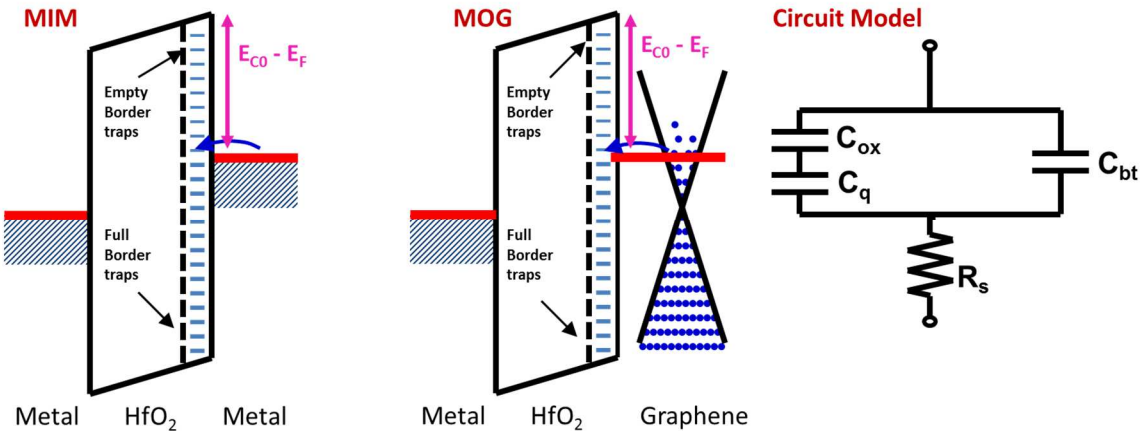


Figure 4-6: Energy band diagram for both MIM and MOG systems illustrated the border traps constant barrier height tunneling model, and lumped circuit model for the border traps capacitance in parallel with the both $C_{ox}$ and $C_q$ in MOG device.

Finally border traps are charged and discharged through an elastic tunneling mechanism. Therefore they are expected to be temperature independent. The temperature dependence issue will be explored later in this chapter.

### 4.2.2 Results and discussion

Two devices are considered in this study, and these samples will be referred to as samples A and B. These devices had a similar fabrication sequence as described in chapter 2, but utilized quartz substrates to eliminate any parasitic substrate capacitance. The quasi-

planar gate electrodes were patterned by embedding metal electrodes in PECVD layer of $SiO_2$ in sample A. Later on PECVD $SiO_2$ was replaced with ALD $Al_2O_3$ in sample B. PECVD $SiO_2$ probably has a rougher surface than ALD $Al_2O_3$ therefore the graphene transfer efficiency was lower in the former. The target $HfO_2$ thickness is 6.8,10 nm respectively, and was deposited by atomic-layer deposition (ALD) at 300ºC. Then the sample was annealed in Ar ambient at 400ºC for 5 minutes. Single-layer CVD graphene grown on Cu foil was then transferred onto the wafer using an aqueous transfer process. The two samples used different Ohmic contact processes, however that is not expected to be significant for this study [67]. The devices area of sample A was determined by fitting. The area in sample A is 670μm$^2$ with an area scaling of 68%. Sample B on the other hand has much better area efficiency because of the difference in the substrate roughness. Both samples were tested in vacuum. These differences are summarized in Table 2.

| Sample | Date | Planarizing dielectric | Graphene sources | Contact Metal | Area efficiency | MIM EOT |
|---|---|---|---|---|---|---|
| A | 2012 | PECVD $SiO_2$ | Vendor | Ti/Pd/Au | 68% | 2nm |
| B | 2014 | ALD $Al_2O_3$ | In-house | Cr/Au | 100% | 4.5nm |

Table 2: Fabrication differences between sample A and Sample B. The quoted EOT values are extracted from the MIM devices.

Impedance measurements were performed using a 50 mV oscillator voltage at frequencies ranging from 5 kHz to 500 kHz and the capacitance extracted assuming a series (Cs-Rs) equivalent circuit. The capacitors had no measurable leakage current between $V_G$ = +2V to $V_G$ = -2V. Before extracting the density of border traps ($N_{bt}$), the C-V curve went through a couple of processes: (1) shifting the Dirac point to zero, and (2) applying the hysteresis correction. Equation 1-2 depicts the process

$$V'_G = (V_G - V_D) * \left(1 - \frac{\Delta V}{2V_{G(max)}}\right), \qquad 4\text{-}6$$

where $V'_G$ represents the new x-axis and $V_G$ is the applied voltage, $V_D$ is the Dirac point, and $V_{G(max)}$ is the maximum applied voltage. Figure 4-7 shows the total capacitance versus log frequencies plot for both MIM and MOG at two different applied voltages for sample A. Since the voltage was normalized to the Dirac point them the $V_G$ = 0V is the Dirac point.

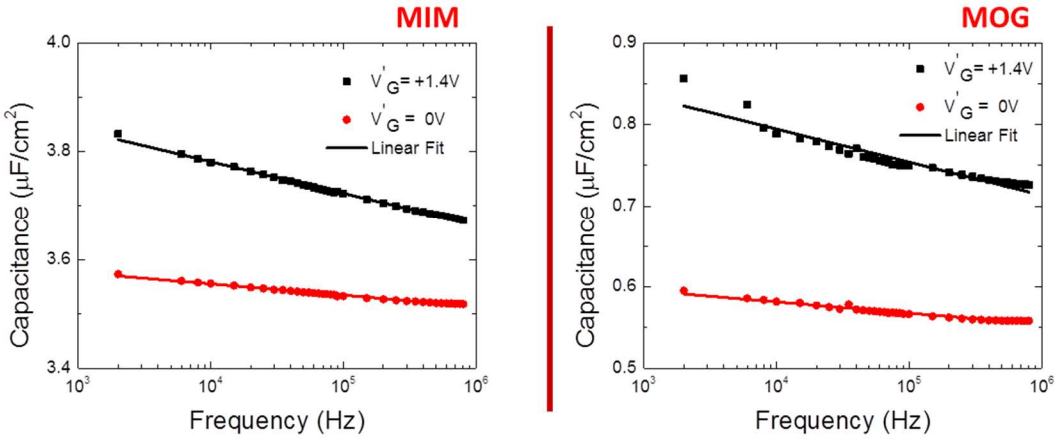


Figure 4-7: Sample A: capacitance vs. log frequency for MIM and MOG capacitors at two different applied gate voltages; $V'_G$ = + 1.4V (black line), and $V'_G$ = 0V (red line).

In some other samples the value of the total capacitance at the positive maximum voltage is not equal to the capacitance at the negative minimum voltage. The reason behind that is the hysteresis of the system which has shifted the Dirac point further away so the capacitance is unable to return back to its original maximum value at the end of the second sweep as shown in Figure 4-8. To avoid unnecessary error in our border trap analysis as a consequence of the hysteresis, samples with such a behavior were excluded.

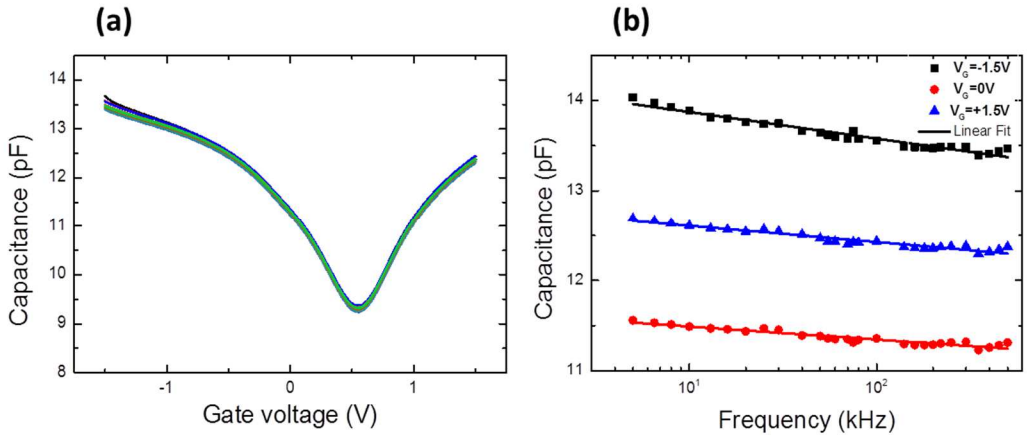


Figure 4-8: (a) MOG capacitance versus applied voltages at different frequencies (75 -500 kHz). (b) Capacitance vs. log frequency with their linear fit at different applied voltages for the device in (a): black at $V_G$ = -1.5V, red $V_G$ = 0V, and blue at $V_G$ = +1.5V.

From equations 4-4, one can see that the density of border traps depends on the device area, therefore not all samples were considered due of the difficulty in accurately estimating the effective area. While Figure 4-7 shows the MIM versus MOG slopes at different voltages at room temperature for sample A, Figure 4-9 shows the same for sample B. Though the capacitance was not normalized to the area in Figure 4-9 , it is considered in the calculation of the density of border traps. One can see that the slopes are slightly different between the two samples, but at each sample the slope of the MIM device, and MOG device are almost identical especially at higher bias voltages. This similarity in the slope between the two devices indicates that the cause of those traps is the same in both devices. At lower applied voltages ($V'_G$ = 0V) however there is significant difference between the slope at $V'_G$ =0 and $V'_G$ = ±1.4V in the MOG devices. This discrepancy in the MOG devise could be related to the lack of states in graphene near the Dirac point.

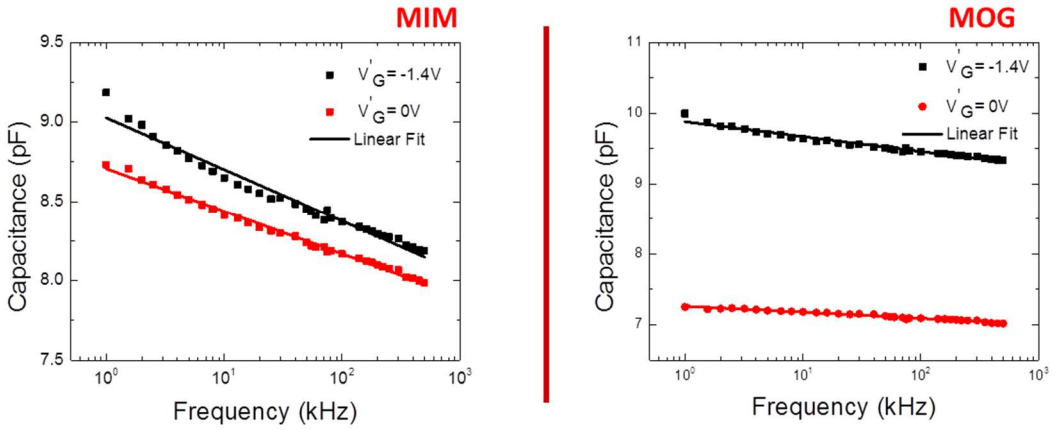


Figure 4-9: Sample B capacitance vs. log frequency with their linear fit (slope) in MIM and MOG at $V'_G$= 0 (red), and $V'_G$ = -1.4 (black).

One can calculate the border traps density at each applied voltage by utilizing equation 4-5. By applying the border trap density extracted using constant barrier height of 2.3 eV and $HfO_2$ effective mass of $0.1m_0$ [104], [107], [110], [111]. That assumes border trap capacitance in parallel with gate capacitance.

Figure 4-10 shows the border trap densities ($N_{bt}$) that were extracted for both structures at room temperature using the model discussed in 4.2.1. The MIM area is 1000µm$^2$, while the MOG device areas are 1088 µm$^2$ and 1200 µm$^2$ in sample A and B, respectively. The prominent features about both samples are: (1) the border traps density shows more dependence on the applied voltage in the MOG devices than it is in MIM ones. (2) The similarity in the order of magnitude among the results, especially at the maximum applied voltage on both structures. The slight variability in the border trap density in MOG device is probably due to the low density of states in graphene near the Dirac point. On the other hand the density of border traps is mostly constant in MIM device because the number of states on the metal side is orders of magnitudes larger than the border traps density. The border traps density at Sample A is ~ 1-2 x $10^{18}$cm$^{-3}$/eV, while sample B is ~ 3-5 x $10^{18}$ cm$^{-3}$/eV. This marginal difference between the two samples is expected since

the samples were fabricated in different times therefore the $HfO_2$ quality might have changed.

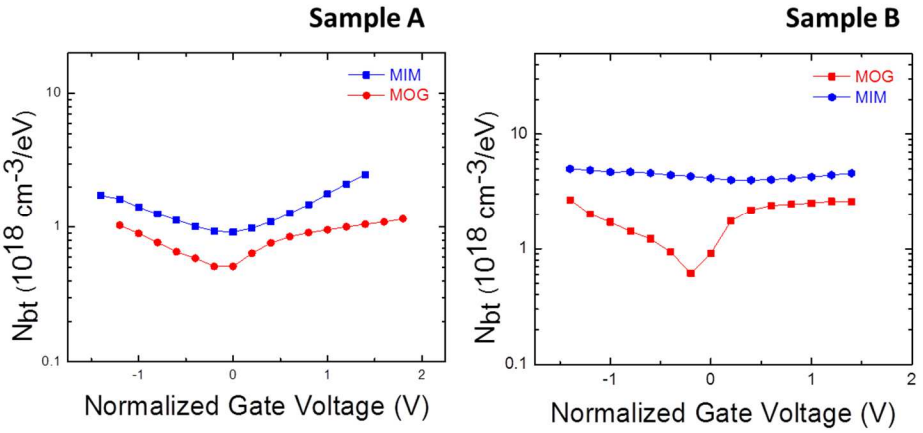


Figure 4-10: Samples A, and B extracted border trap densities at room temp versus normalized gate voltage for MOG (blue), and MIM (red).

The border trap density voltage dependence in sample A, in both MIM and MOG could be due to several effects. The first possible cause could be the traps energy dependence. In other words the border traps can be spatially and energetically distributed across the oxide. Second, the increase in the electric filed could decrease the effective tunneling barrier height. In other words the anomaly in Figure 4-10 could be related to the Fowler-Nordheim approximation which was not considered in this analysis. Finally, the $N_{bt}$ of the MIM and MOG devices in sample B show different voltage dependence. The MIM trap density has almost zero dependence on voltage, while the MOG traps density drops significantly in the Dirac point vicinity. As was hinted before the lack of states at the Dirac point could affect the apparent number of trap states, thus in MOG the trap density-voltage dependence could be a consequence of both the trap-energy dependence as well as the lack of energy states on the graphene side.

### 4.2.3 Temperature dependence results

In order to further explore the nature of the graphene-$HfO_2$ interface, the capacitance vs. frequency characteristics were analyzed at different temperatures from 4.2K to 380K. The experiment takes place in an open flow cryogenic probe station under vacuum using liquid helium as the coolant. In this section two samples will be considered, and a full set of frequency and temperature dependence measurements have been performed. Sample A from the previous section and another sample C were utilized and the sample parameters are listed in Table 3.

| Sample | Date | Planarizing dielectric | Graphene sources | Contact Metal | Area efficiency | MIM EOT |
|---|---|---|---|---|---|---|
| A | 2012 | PECVD $SiO_2$ | Vendor | Ti/Pd/Au | 68% | 2nm |
| C | 2013 | PECVD $SiO_2$ | In-house | Ti/Pd/Au | 62% | 3.1nm |

Table 3: Fabrication differences between sample A and Sample C. The quoted EOT values are extracted from the MIM devices.

Figure 4-11 shows the C-V sweep at several frequencies at 4.2K and 300K for the MOG device in sample (A). At $T$ = 4.2 K, the quantum capacitance "dip" gets steeper, while the frequency dispersion is suppressed. In contrast, strong frequency dispersion is observed at room temperature, where the overall capacitance increases with decreasing frequency. The absence of frequency dispersion at $T$ = 4.2 K is an indication of trap freeze out.

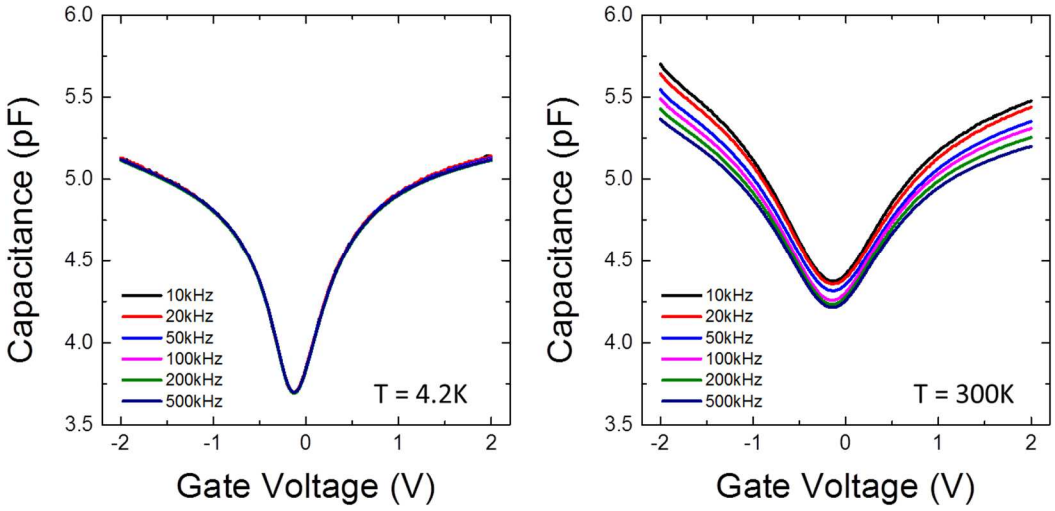


Figure 4-11: Capacitance versus gate voltage in MOG devices in Sample A, at both 4.2K and 300K.

To show the fact that this suppression is observed merely in MOG devices, Figure 4-12 shows the capacitance versus voltage at different frequencies in both devices MIM, MOG at 4.2K and 300K. It is clear that there is inconsistent behavior between the two devices. The frequency dispersion is not a temperature dependent in the MIM devices which is consistent with border traps charging mechanism as it is a tunneling mechanism. Tunneling does not depend in its nature on temperature, but rather on the tunneling distance. To better understand the temperature dependence behavior in MOGs, capacitance versus log frequency at different temperatures was plotted in Figure 4-13 for both MOG and MIM devices.

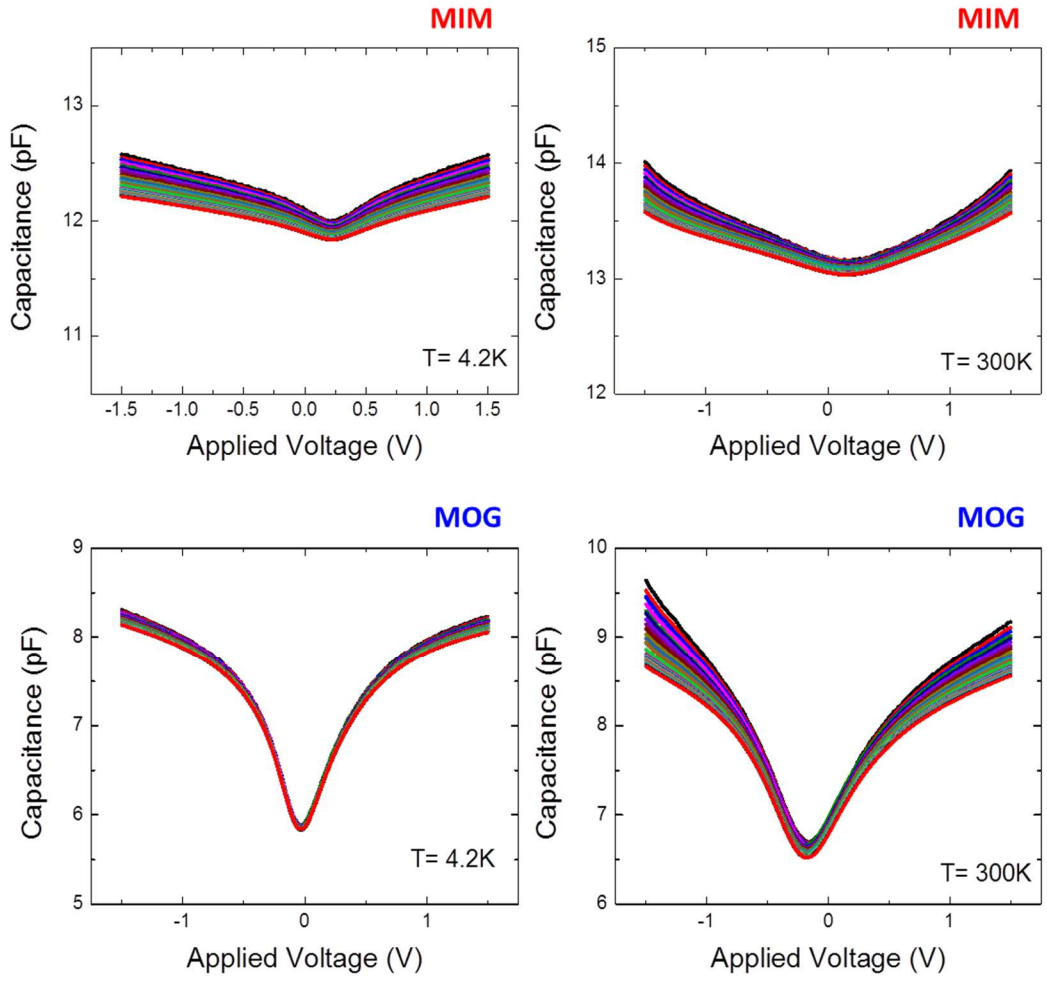


Figure 4-12: Sample C, MOG device (red) and MIM device (blue) plot of capacitance at multiple-frequencies (5-500 kHz) versus applied voltage at 4.2K (left) and 300K (right).

The measured capacitance vs. frequency in Figure 4-13 shows a linear dependence of $C_g$ versus log ($f$). Two prominent properties are observed from Figure 4-13. First, the relative temperature-independence behavior at all temperatures and biases for MIM device, a consistent trend with border traps characteristics. Second, temperature dependence observed at MOG device, suggesting an additional mechanism. Furthermore, the temperature dependence is observed more further away from the Dirac point [107].

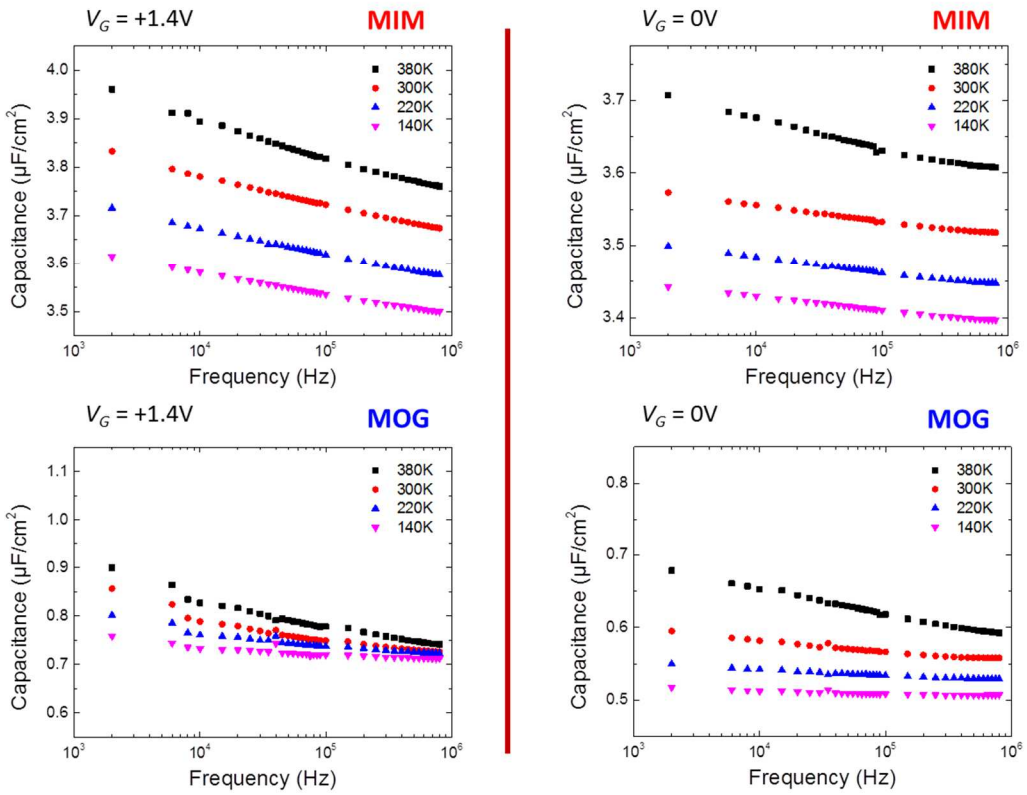


Figure 4-13: Plots of measured capacitance vs. frequency at different temperatures for MIM (red), and MOG (blue) in sample A, at $V_G$ = +1.4V (left) , and $V_G$ = 0V (right).

Structurally the difference between the two devices is the vacuum gap in the MOG device. Since the vacuum gap can be considered a wide band gap material with a very thin thickness (~3Å) it is expected to affect only the tunneling probability. The temperature dependence is normally indicative of a thermionic conductivity effect. In other words, a material with a small band gap but very thin. Such a material if intercalated between the graphene and $HfO_2$ could be behind the temperature dependence.

In order to extract the border trap density at all temperatures, an area scaling term was found by fitting, and it is used to account for the partial delamination of the graphene. As was presented in Table 3 the area efficiency in those two samples is not high due to the

roughness of the PECVD $SiO_2$ surface. The border trap density, $N_{bt}$, versus normalized gate voltage $V'_G$ is shown Figure 4-14. Once again the $N_{bt}$ has been extracted from the slope of the gate capacitance vs. log frequency plot using a simple first-order approximation as in equation 4-5. Extracted border trap densities for MIM and MOG capacitor $N_{bt}$ values of ~ 1-2 x $10^{18}$ $cm^{-3}/eV$ determined for MIM devices. Similar values for MOG devices at high temperatures, but the apparent border trap density decreases at low temperatures. The extracted values of $N_{bt}$ for both the MOG and MIM capacitors are plotted at different temperatures for each sample. The border trap density for the MIM capacitors is in the order of $10^{18}$ $cm^{-3}/eV$, consistent with prior studies on $HfO_2$ [105].

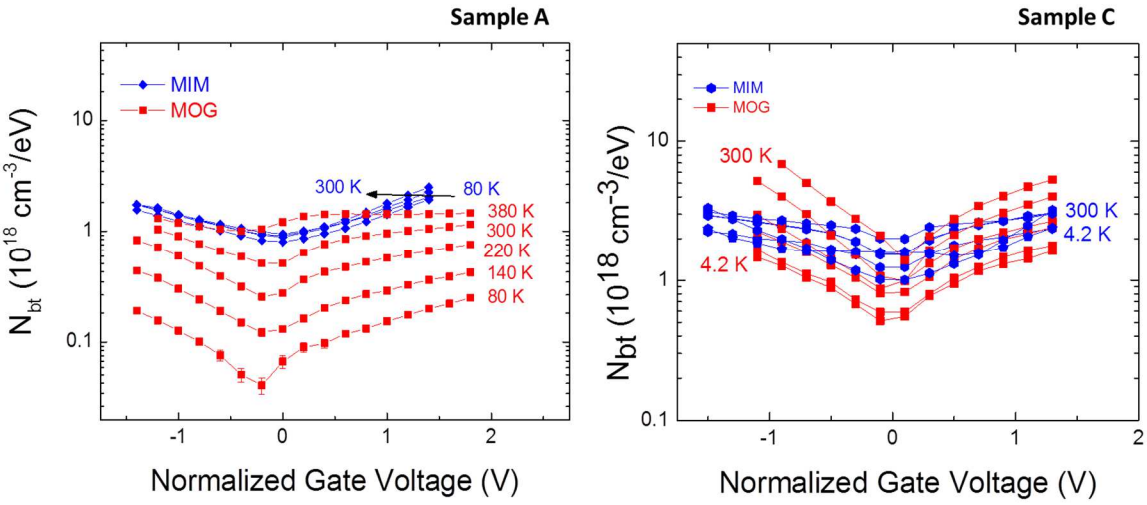


Figure 4-14: Samples A, and C extracted border trap densities versus normalized gate voltage for MOG (red), and MIM (blue), at various temperatures.

The agreement between the high-temperature $N_{bt}$ values between the MOG and MIM capacitors also suggests that the $HfO_2$ border traps are the primary cause of the frequency dispersion. The temperature dependent frequency dispersion is still not fully understood and more detailed study for this phenomenon is needed to understand the kinetic process of suppressing the traps at lower temperatures.

Finally, a proportional increase in total capacitance to the temperature was observed in both the MIMs and MOGs. Similar behavior was observed before in a top gated GFET with $Y_2O_3$ as a gate oxide. This behavior could be explained with the change in the dielectric constant value with temperature [112]. Figure 4-15 shows the capacitance versus applied voltage in sample C, at different temperatures for both MOG and MIM devices.

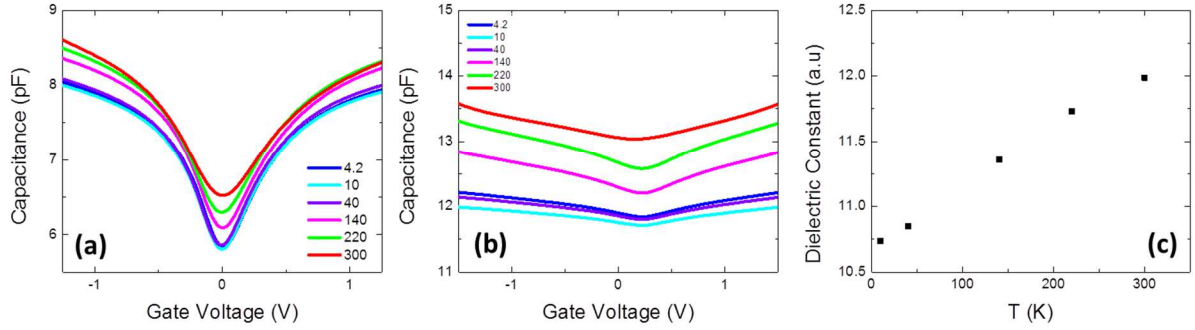


Figure 4-15: Capacitance measurements at 500 kHz temperature (4.2K-300K). (a) MOG C-V data. (b) MIM C-V data. (c) The dielectric constant of $HfO_2$ as a function of temperature measured from the metal–$HfO_2$–metal structure.

The dielectric constant was extracted from the MIMs data assuming the physical thickness is 8 nm and the total area is 1000µm$^2$ .The frequency used is 500 kHz because it does not have an excess capacitance from the border traps [78].

## 4.3 Summary

Despite recent publications [52], [98], which address the issue of traps in graphene systems, prior to this work a comprehensive analysis had not been performed. In this chapter the trapping mechanism in MOG capacitors with $HfO_2$ dielectrics was investigated. Border traps are the likely dominate traps in graphene/$HfO_2$ due to the lack of dangling bonds in graphene. This study is based on comparing two structures (MIM devices to MOG) that share the same oxide. The findings suggest that border traps dominate at high temperature and bias voltages, while this trapping is suppressed at lower temperatures. The same trapping behavior was observed in MIM structures. Unlike MOG structures, the frequency dispersion is temperature independent in MIM structures. A more sophisticated model is needed to fully understand the trapping mechanism in graphene devices. The new model should also account for the vacuum gap between the graphene as well as impurities between graphene and $HfO_2$.

# Chapter 5 :
# Effect of Surface Functionalization on Graphene Varactors

*"Functionalization is among the significant vectors that drive graphene towards technological applications." Liang.Yan.et al Chem. Soc. Rev.,2012, 41, 97–114.*

## 5.1 Surface functionalization

### *5.1.1 Motivation*

Numerous demonstrations of graphene sensors have been made in the literature [39], [40], [43], [46] most of which have been based upon resistive sensing. Capacitance-based sensing is also possible in graphene, leading to the potential to create passive wireless sensors, which could be useful for in vivo applications [22], [23]. Whether it is resistive based sensing or capacitive based sensing, some type of functionalization scheme is required to achieve selectivity and sensitivity. A study on the effect of surface functionalization on the graphene properties is needed. This study provides important information regarding how surface functional groups affect the properties of graphene. This information could be critical for the future use of graphene as a practical sensor material. One of the main goals of building graphene varactors is to make graphene wireless sensors that utilize the low density of state in graphene to make wireless ultrasmall sensors with high quality factor. Studying the functionalization effect on the quantum capacitance paves the way to the realization of a wireless glucose sensor. Retaining the basic electronic properties of graphene such as linear energy momentum dispersion, and low quantum capacitance at the NP is crucial for the success of this sensor. Therefore capacitance measurement was performed on varactor devices at each

step of the surface treatment, to study the change in the graphene nature due to the surface modification. This study offers additional information about the surface interactions between the functionalization groups and graphene. In addition it shows the measure of functional groups effect on the density of states and disorder in graphene. Graphene capacitance based wireless sensors have been demonstrated already for water vapor [22], [23], [113], therefore functional groups could allow a new class of wireless biomolecular sensors. Glucose sensors in particular have been our interest. This chapter provides a study of the effect of glucose oxidase surface functional groups on the quantum capacitance and the overall capacitance properties for metal-oxide-graphene structures.

### 5.1.2 Non-covalent functionalization

Although graphene is an inert material, it is chemically not saturated. That allows it to form both covalent and non-covalent bonds through its basal plane. Covalent bonds change the $sp^2$ structure to $sp^3$ and require high energy [114]. Non-covalent bonds on the other hand, can be formed with much lower energy, and the graphene structure preserves its $sp^2$ structure lattice [114]. Therefore the non-covalent bonds allow the graphene to be fully functionalized while preserving its unique characteristics. The main focus in this chapter is on non-covalent functionalization by using the π-π interaction as the binding force between the 1-pyrenebutanoic acid succinimidyl ester (linker) and graphene. Since the functionalization process that is used in this chapter is for glucose sensing applications, glucose oxidase (GOx) is used. In addition there is a deactivation step to deactivate the reactive ends of the unused linker. The graphene functionalization paves a way to understand more graphene density of state and investigate the effect of the defects and the edges. It is reasonable to think that the graphene functionalization is not as simple as just π-π interaction as the edges and defect sites might have different ways of bonding. For the purpose of practicality and due to the relatively large area of the devices, those

side reactions will be ignored [40], [114]. Basic understanding of chemical or electro-chemical sensing starts by understanding how the surface treatment is bonded and how it reacts with graphene [47]. A similar functionalization scheme was used in [115], [116] on GFET, and the GFET response to glucose was recorded as shown in Figure 5-1. However there was no monitoring of the GFET electrical characteristic during the stages of functionalization or a deeper understanding of the functionalization effect on the device. In both references the response to the change in glucose concentration was recorded as a change in the GFET drain current (conductivity); therefore both those sensors are active wired sensors and the GFET needed to be biased at certain regime.

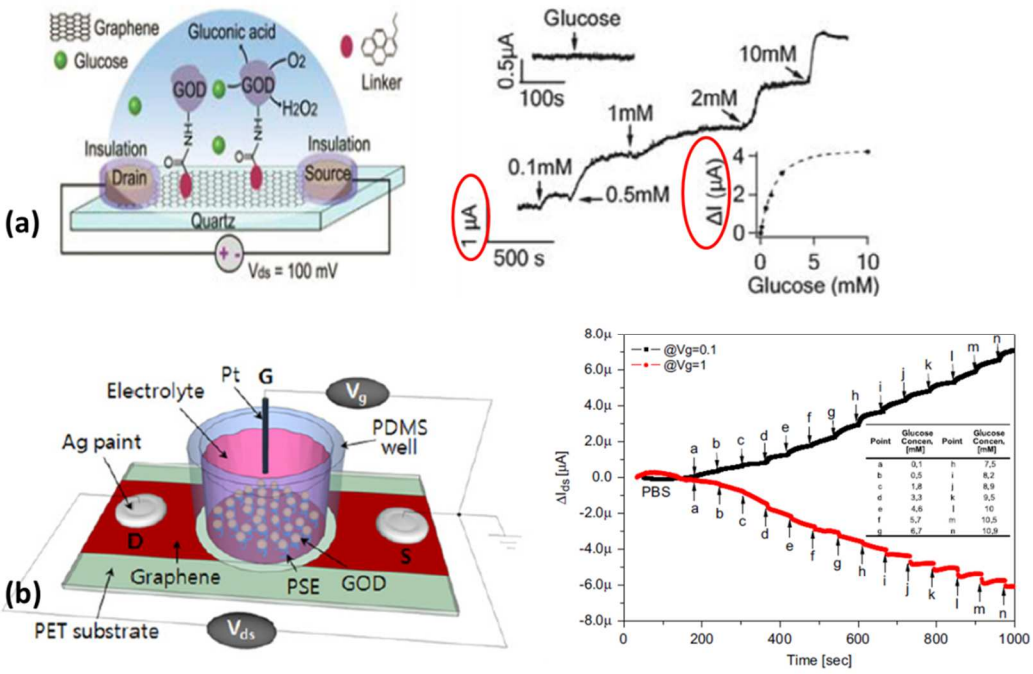


Figure 5-1: Previous work on graphene glucose sensors. (a) Work from [10] for GFET shows the functionalization scheme (left) and the recorded response (right). (b) Cartoon of the functionalized device in [11] (left) and the recorded change in drain current (right).

## 5.2 Experiment evolution

### 5.2.1 Functionalization procedure and detection

The functionalized process is a three-step process, similar to that described in [78], [115], [116]. First the sample is submerged into the linker solution for two hours, which is enough for the physisorption of 1-pyrenebutanoic acid succinimidyl ester (1-PASE) and graphene to take react, leaving the graphene in π-π interaction with the linker molecules. Then the sample is rinsed with deionized water. Later the sample is submerged into a glucose oxidase (GOx) solution overnight, which is enough time for the glucose oxidase to be attached to the linker with a covalent bond. Due to the difference in the size between the linker molecules and the glucose oxidase molecules, some of the linker molecules are left reactive. Ethanolamine solution is used to deactivate the unreacted linker. Therefore the sample was immersed in ethanolamine solution for approximately 40 minutes, rinsed with deionized water and gently dried under a stream of nitrogen. The details of the functionalization process can be found in Appendix B.

The molecule 1-PASE was chosen as the linker since the π–π bonds have been shown to provide a stable bond to graphene and also react readily with GOx to form a covalent link to immobilize GOx on graphene. When operated as a glucose sensor, the GOx catalyzes the oxidation of glucose to produce gluconic acid and hydrogen peroxide as in Figure 5-2(a). It has been previously shown on field-effect transistors that graphene is sensitive to $H_2O_2$ concentration, though the exact sensing mechanism is not fully understood [78], [115]–[117].

The 1-PASE/GOx surface functionalization procedure was first evaluated on blanket graphene samples in order to independently confirm that the surface functionalization could indeed be realized. For this purpose, GOx serves as an ideal test tool to verify the attachment of the linker molecule, since the presence of GOx on the graphene surface can

readily be detected using chemical and physical characterization [115], [116]. Since GOx works as a catalyst in which glucose is oxidized to produce gluconic acid and hydrogen peroxide, a luminescence spectrum confirming $H_2O_2$ production from GOx-functionalized graphene can be used to assure the existence of the GOx. A 5 mM of glucose was added to the functionalized graphene surface, and the luminescence spectra was taken after an hour to allow enough time for the reaction to occur. A positive control sample was used by dissolving GOx directly into 5 mM of glucose solution, and the measurement was then compared to the graphene results, as in Figure 5-2(b) [118]. More details on the chemiluminescence experiment are in Appendix B. The presence of GOx on the graphene surface was also confirmed with atomic force microscopy (AFM). The size of the GOx enzyme that was detected on the surface agrees with the size in the literature Figure 5-2(c-d) [119]. GOx molecules are the rounded features in the figure with average height of ~ 5.0 nm, which is consistent with the known radius (6.2 nm) of GOx; however the lateral diameter of the features is significantly larger (~100 nm) than expected. This lateral distortion of the GOx molecules is likely a result of agglomeration of GOx during the immobilization and subsequent desiccation of GOx on the graphene surface.

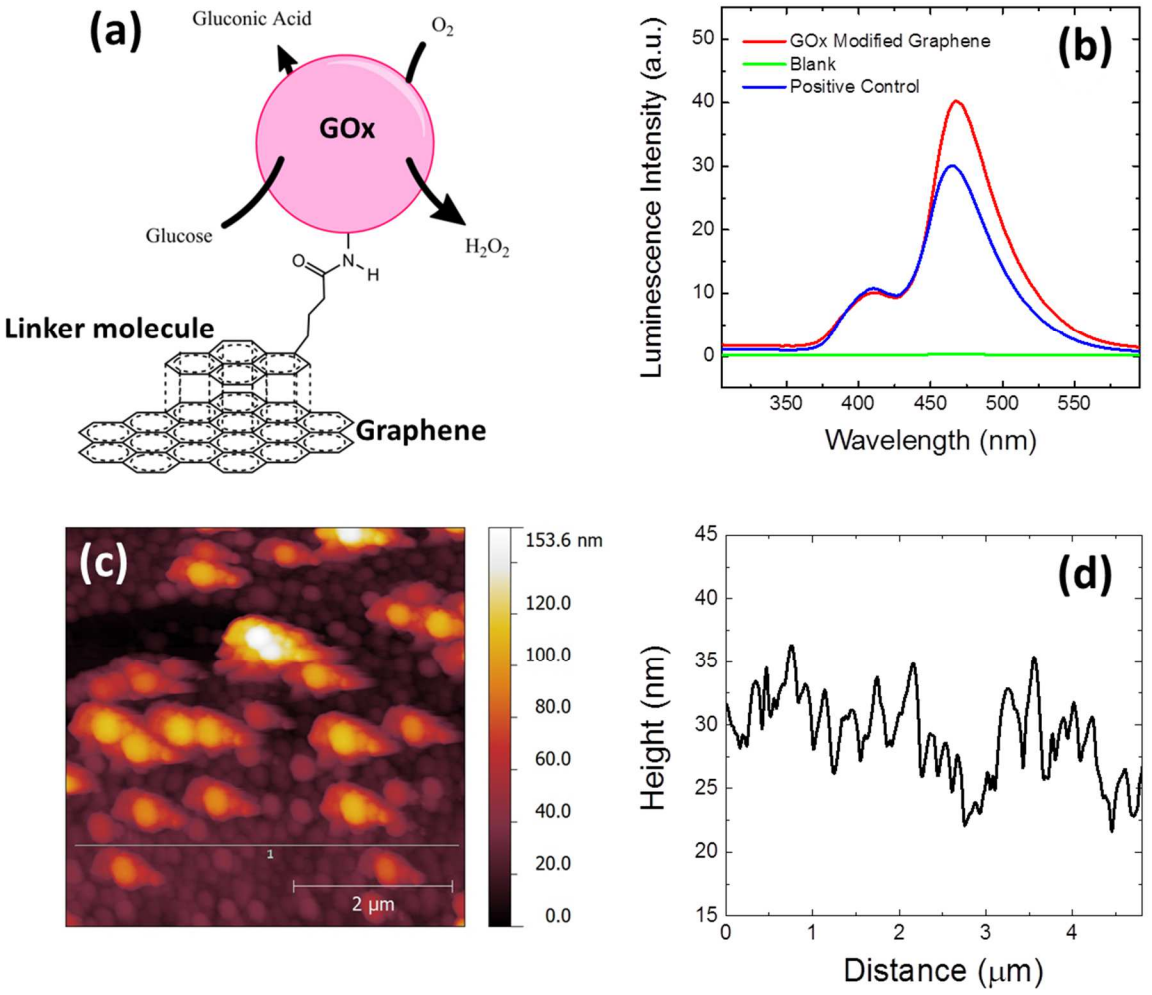


Figure 5-2: (a) Schematic diagram of Glucose oxidase (GOx) attachment to graphene. (b) chemiluminescence spectra confirming $H_2O_2$ production from GOx-functionalized graphene as well as a positive control of GOx in solution. (c) Atomic force microscope (AFM) image of functionalized single-layer graphene. (d) Line scan AFM image from the sample in (b) indicating a mean height variance of 5.0 nm, consistent with expected value of 6.2 nm for GOx.

Finally, the effect of the surface functionalization at each stage was further characterized using Raman spectroscopy. Raman spectroscopy confirmed that the functionalization through π-π interaction is not a destructive process and the graphene maintains its original Raman signature [25], [78], [120]. Figure 5-3 shows the Raman spectroscopy

results after each step of the functionalization. This is point Raman spectroscopy and not a line or area scan.

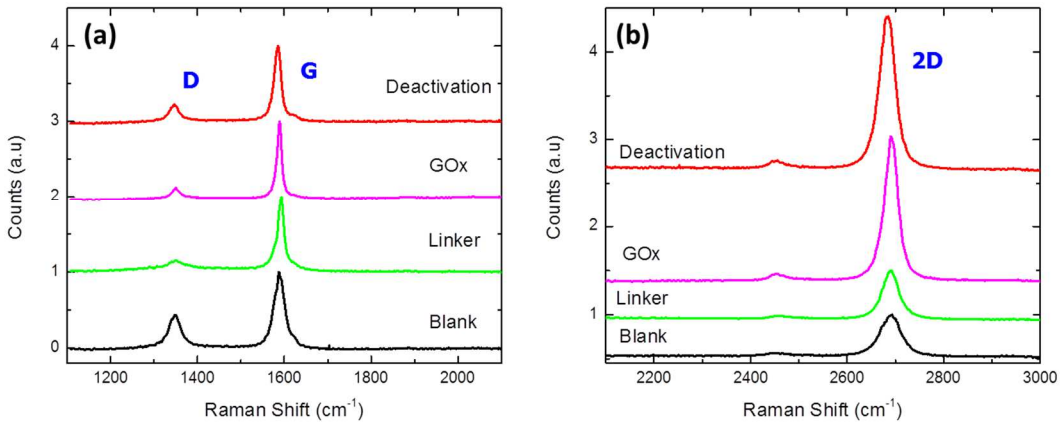


Figure 5-3: The Raman spectroscopy confirmed that the functionalization does not change the graphene lattice structure. (a) The D and G peaks after each stage of functionalization. (b) The 2D-peaks after each stage of the functionalization.

It should be pointed out that some uncertainty exists in the Raman spectra, since the precise point on the sample where the spectra were taken could have varied in the successive measurements in Figure 5-3. Therefore, precise trends in the Raman spectrum with functionalization could be determined, however, it is clear from the data that the functionalization maintained the $sp^2$ nature of the graphene and did not substantially affect the band structure or disorder.

### *5.2.2 Varactors functionalization procedure*

In this study there are two different samples involved. One of those samples has the sensor mask layout. As this study is strongly related to the wireless glucose sensor project, it is not surprising that the effect of the functionalization was first detected on a graphene sensor device. Graphene sensor are also varactors but with much larger active

area (almost 10 times more), and they can be probed through long pads as was described in chapter 2. After the changes at each stage of the functionalization were noticed, an independent study with a smaller mask set up was performed. The smaller mask has less fabrication steps. It also does not have long metal pads which can add some parasitic capacitance. An optical micrograph of the first functionalized sensor device is shown in Figure 5-4(b). Figure 5-4(a) shows a cartoon that depicts the functionalization scheme and the device on the sensor sample after functionalization. The other sample (smaller mask set) has seven devices, all of which all were involved in this study. Therefore they will be the focus of the study. In brief, all the samples are made on $Si/SiO_2$ with a thick thermal $SiO_2$ (980 nm) substrate. The gate dielectric is $HfO_2$; it was deposited by atomic-layer deposition (ALD) at 300$^{o}$C, and the final physical thickness is ~ 9 nm. Single-layer graphene grown by chemical vapor deposition was then transferred onto the wafer using an aqueous transfer process [62]. The device fabrication process is similar to the one described in chapter 2. After fabrication, but before functionalization, the device was baked in vacuum (~ $10^{-6}$ Torr base pressure) at 380K for 20 hours in order to desorb moisture from the graphene surface. Capacitance versus voltage measurements were then performed using an Agilent B1500A semiconductor parameter analyzer at frequencies ranging from 5 to 500 kHz, and using an rms oscillator voltage of 50 mV. No measurable gate leakage was detected in all the devices over the range of gate voltages tested, and therefore, the series equivalent circuit mode (Cs-Rs) was utilized for the C-V measurement. In addition, the capacitance value of the open-circuit pad geometries (~80 fF) was measured and subtracted from the results. This experiment utilizes three different structures on the device chip. First the back gated varactors, which are two terminal devices in a multi finger configuration. Second back gated GFETs, three terminal devices which have less total area hence less capacitance. However GFETs provide us with both C-V and I-V measurements that can be correlated. Finally, the metal-insulator-metal devices, which are used as control devices to estimate the EOT values.

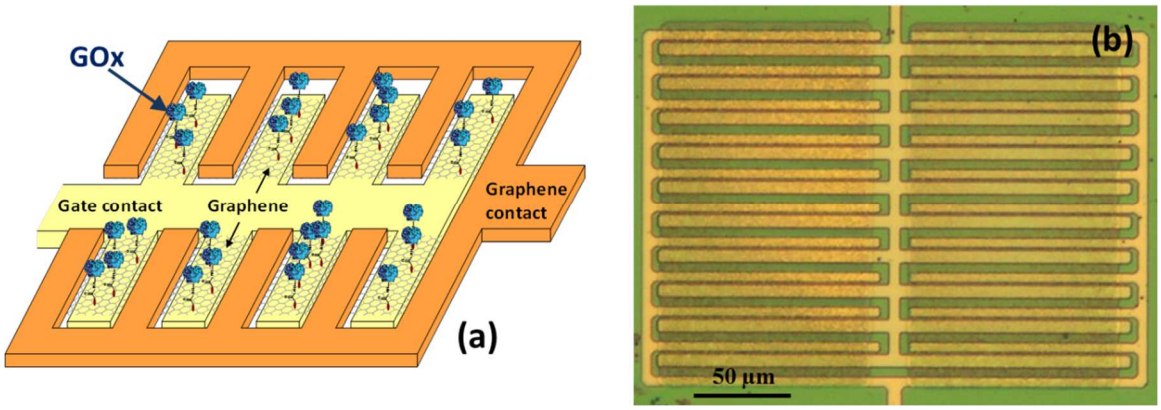


Figure 5-4 (a): Schematic diagram of functionalized graphene varactor. (b) Optical micrograph of the used device for experiments.

## 5.3 Results and discussion

### 5.3.1 Measurement devices and set up

Figure 5-5 shows the first functionalized sensor data. The device was first measured in air before the functionalization started ( black curve) then the device was fully functionalized in three steps process, as presented earlier, and measured again in air ( red curve). The functionalization introduced several changes to the C-V curve, starting with the Dirac point, the shape of the C-V curve, and even the total capacitance value. Those changes can be summarized as (1) the Dirac point shifts to less positive value. (2) Hysteresis increases. (3) The tuning range also increases. The first sensor was not measured in vacuum before air because the experiment was not intended to monitor the functionalization effect on the graphene but rather to prepare the device for the glucose sensing experiments. Since the changes were very intriguing, a study was dedicated to focus on the effect of functionalization at each step. The next section will explore the observable trends of those changes at each step across several samples.

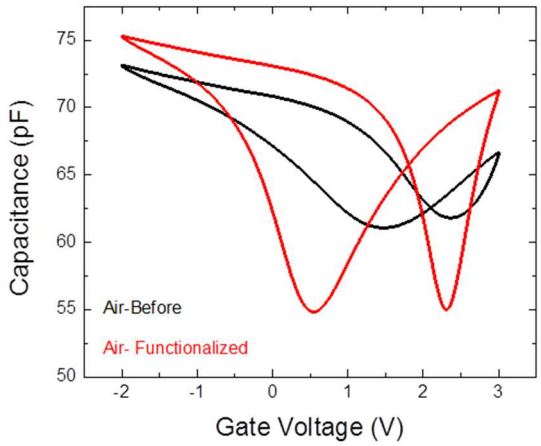


Figure 5-5: Capacitance vs. gate voltage at both up and down sweeps, at 500 kHz for the first sensor with physical layout area of 10,000μm$^2$ before (black), and after (red) functionalization. Both measurements were taken in air.

### 5.3.2 Observable trends

From this point and onward the focus will be on varactor sample in which seven devices total were measured, five varactors and two GFETs. The measurements were first carried out in vacuum after 20 hours bake to define a benchmark point for both the Dirac point and the C-V characteristic at what is believed the closest to the ideal. For the GFETs both C-V characteristics and $I_D$-$V_G$ have the same Dirac point. This value reveals the doping level in the graphene sheet. After the measurements in vacuum the devices are measured in air before the functionalization. Later, the devices were measured in air after each step of the functionalization. The sweep window and the frequency set were kept the same to ensure fair comparison and consistency. Figure 5-6(a) shows the C-V curve for a varactor in vacuum after 20 hours bake. Figure 5-6(b) shows the trends that were observed at the same varactor in air before the functionalization, and after each step of the functionalization. While hysteresis similar to Figure 5-5 was observed in all samples, only the reverse sweep ($V_G$ decreasing) is considered. The color code is consistent

throughout the chapter. The C-V measurement in black represents measurements in air before the functionalization, and has a Dirac point of ~0.75V which is an indicative of p-type doping. While the maximum capacitance has increased relative to the blue line (vacuum), the total capacitance tuning has drastically decreased with higher quantum capacitance (larger minimum), and more smearing is observed at the Dirac point. Once the linker molecules are attached (green line), the Dirac point within two hours was shifted back to ~0.4V with less smearing at the Dirac point and lower maximum capacitance. Attaching the GOx (Magenta) did not shift the Dirac point significantly, but the capacitance tuning has increased by increasing the maximum capacitance. This trend of restoring the C-V curve back to its original shape in vacuum continues as the functionalization progresses. The deactivation curve (red line) has higher capacitance tuning due to the remarkable increase in the maximum capacitance with retaining the minimum capacitance same as in vacuum. The C-V curve appears to be less stretched out after the deactivation than it is in vacuum. The slight enhancement after the deactivation step could be related to the unsatisfied bonds of the linker. As those bonds become deactivated the system becomes more stable. In some other cases, the functionalization restored the Dirac point even closer to zero than it was in vacuum. The Dirac point is shifted in air toward a positive value, and it became less positive after each step of the functionalization. This change in the Dirac point indicates some sort of n-type doping to the graphene by the functionalization group. This unintentional doping is in some cases even more effective than the baking. Furthermore, the tuning range, the ratio of the maximum capacitance to the minimum capacitance, increases and the C-V curve becomes narrower, which implies that the functionalization somehow mitigates the disorder in the graphene. It is important to remember that all the measurements, during and after the functionalization, were taken in air with the graphene surface totally exposed to the room temperature and humidity.

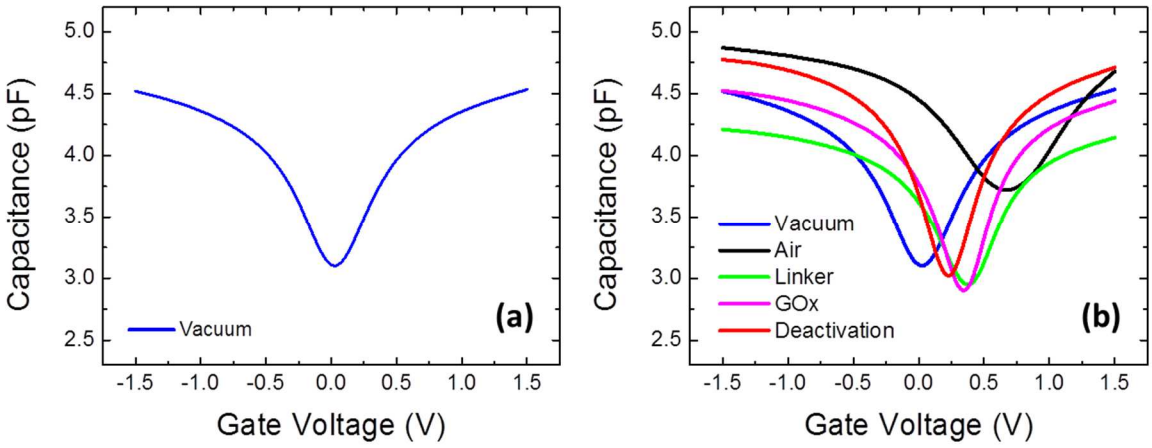


Figure 5-6: Plot of measured capacitance vs. gate voltage for one of the graphene varactors at 500 kHz (a) In vacuum (before functionalization). (b) At every step of the experiment as vacuum (blue), air (black) ,1-PASE (green), GOx (magenta), and deactivation (red).

These changes were observed across seven devices with varying geometrical dimensions, which is an indicative of the repeatability of these trends. The values for the average Dirac point follows similar steps across several samples starting around zero volts in vacuum which is expected, and then it shifts to be more positive as the sample becomes exposed to moisture in air [39], [78]. The plot in Figure 5-7(a) shows C-V measurement where the capacitance is normalized to the maximum to clarify the Dirac point shift. Figure 5-7(b) shows the average value of $V_{Dirac}$ (indicated by the dashed line) is -0.07 V in vacuum (step1). Upon testing in air, the average value has increased to +0.29V (step2). Finally, after the successive functionalization steps, and after the deactivation the average Dirac voltage is 0.02V (step5), which is nearly the same as its original value in vacuum. The upsweep Dirac points are almost the same as in vacuum, but the hysterics makes the down sweep a bit different. The Dirac points for both up and down sweeps were considered independently. In Figure 5-7(c) the Dirac points were all normalized to zero to emphasize the change in the row maximum capacitance in one device. Figure 5-7(d) shows the maximum capacitance per unit area trends across seven devices after each step in the functionalization process. The maximum capacitance is defined as the average

capacitance at $V_G - V_{Dirac}$ = +1.3 V. The maximum capacitance per unit area changes through the evolution of the experiment; it increases by (20%) as we take the measurement in air, but then it drops by (30 %) after attaching the linker molecules. However, the maximum capacitance is higher than the vacuum value after the deactivation step [78].

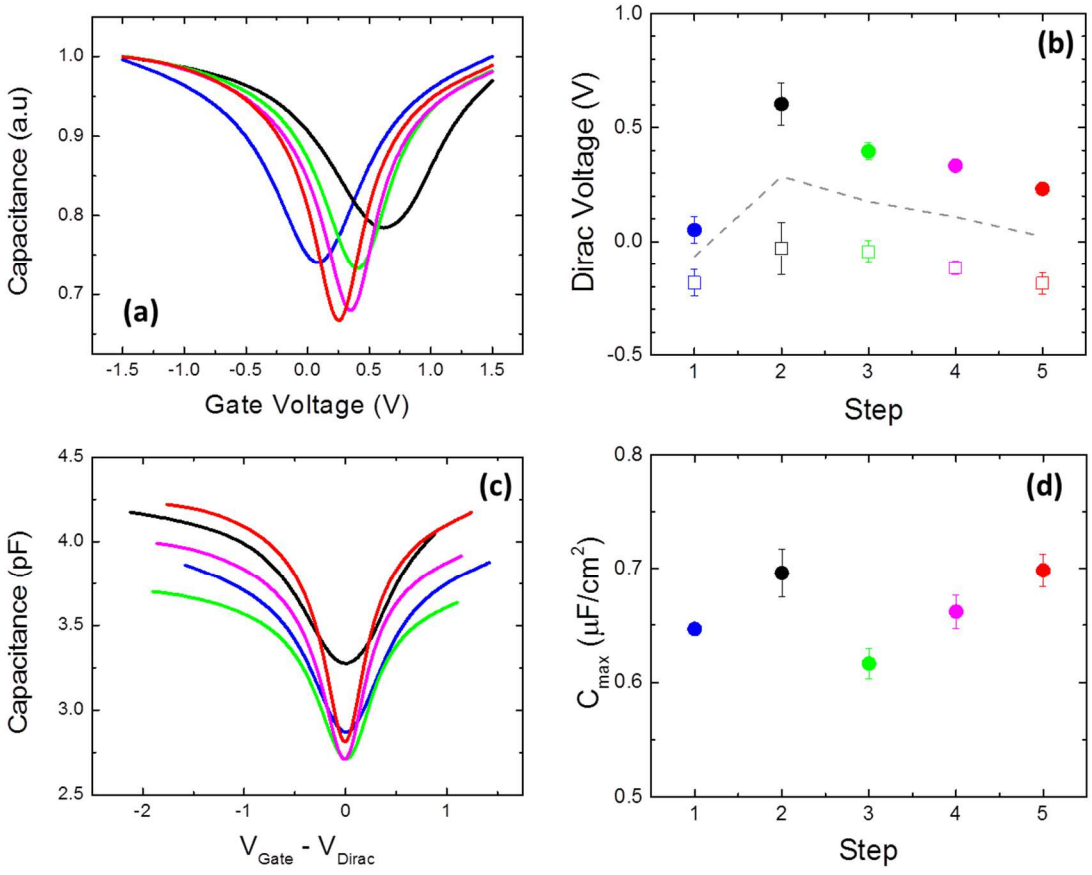


Figure 5-7: (a) Normalized to the maximum (C-V) curve for one varactor under all conditions: before the functionalization in vacuum (blue), and air (black), and at after attaching the linker (green), GOx (magenta) and finally deactivation (red). (b) Dirac point statistics for seven samples for up (open symbols) and down (solid symbols) sweeps, as well as the average between the two (dashed line). (c) C-V curve for one varactor, the x-axis is normalized to the Dirac point. (d) Maximum capacitance statistics for seven samples, with the same color code as in (b).

The maximum capacitance per unit area itself does not capture the full picture of the change in the capacitance tuning because the minimum capacitance is an important part of the tuning range. The tuning rang which is the $C_{max}/C_{min}$ is plotted vs. the functionalization steps in Figure 5-8(a). Figure 5-8(a) shows that the tuning range for several devices starts as 1.35 in vacuum then drops by 10% in air. However it rises up again as the functionalization progresses to reach ~1.45 after the deactivation. One should realize that $C_{max}/C_{min}$ is a combination of the increase in the $C_{ox}$ value, probably due to the reduction in EOT, and the stronger domination of $C_q$ which is probably due to the reduction in random potential fluctuations. Figure 5-8(b) shows the level of hysteresis after each of the functionalization steps. The average hysteresis between the two sweeps in vacuum is about 0.23 V. Upon testing in air, the average value increases dramatically to 0.63 V. The average hysteresis (> 0.4 V) remains even with Dirac voltage of 0.02 V, which is nearly the same as its original value in vacuum. Both the forward and reverse sweeps were averaged together when extracting the tuning range, maximum capacitance and hysteresis.

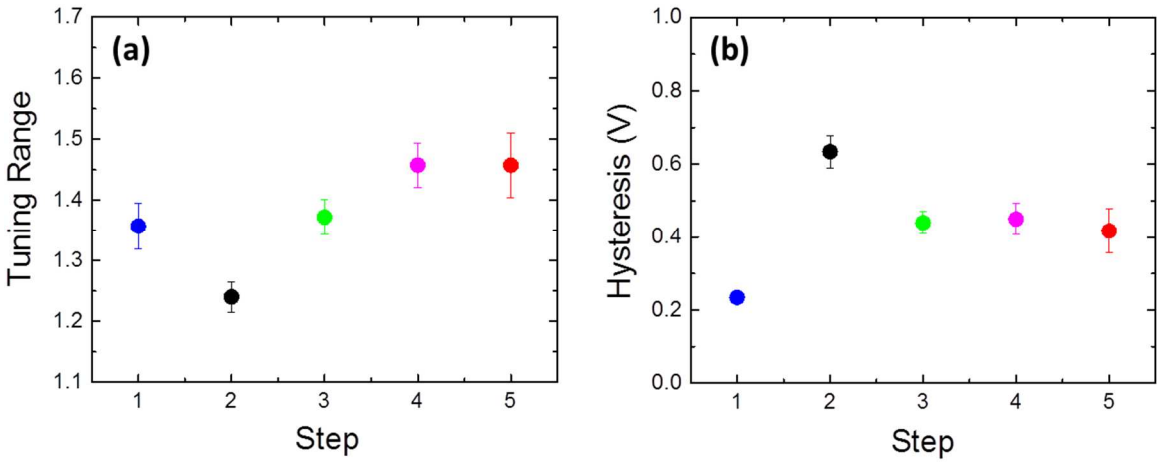


Figure 5-8: Plot of measured parameters compiled from seven graphene varactors as a function of the functionalization steps. (a) Tuning range ($C_{max}/C_{min}$). (b) Hysteresis determined as the difference in the Dirac voltages between the up and down sweeps. The error bars indicate the standard deviation obtained over seven devices.

The previous C-V curves were all taken at 500 kHz to avoid inconsistency. The effect of functionalization at multiple frequencies was also studied. Figure 5-9(a-b) show the difference between the C-V measurement in vacuum and after the functionalization is completed. Unlike the data at vacuum, the Dirac point changes with frequency in Figure 5-9(b). This Dirac point – frequency dependence after complete functionalization, indicates different trapping mechanism than the one which was explored in chapter 4. To further understand this new behavior, capacitance versus log (f) at each step of the functionalization was plotted. Figure 5-9(c) shows *C* vs. log (f) data at the Dirac point. In vacuum, the slope is nearly zero due to lack of states as was explained in chapter 4. The slope increases slightly in air before functionalization (black). Once the linker molecules (green) are attached the slope increases. The slope does not change much afterwards. The same characteristics were plotted at +1.5 V in Figure 5-9(d). It is important to notice that the slopes at all stages are almost identical; however it is still slightly greater after functionalization. The reason for the higher slope increase at the Dirac point in air could be related to the gap between the graphene and $HfO_2$. Water molecules from the ambient atmosphere could have intercalated in this gap, which is quite possible considering the hydrophilicity of $HfO_2$ [121]–[123]. The additional increase in the slope after the functionalization could be related to the functionalization molecules themselves. The additional molecules could have added new states to tunnel from that were not there in vacuum case. In addition, the noticeable increase in the hysteresis in Figure 5-9(b) supports this hypothesis [78].

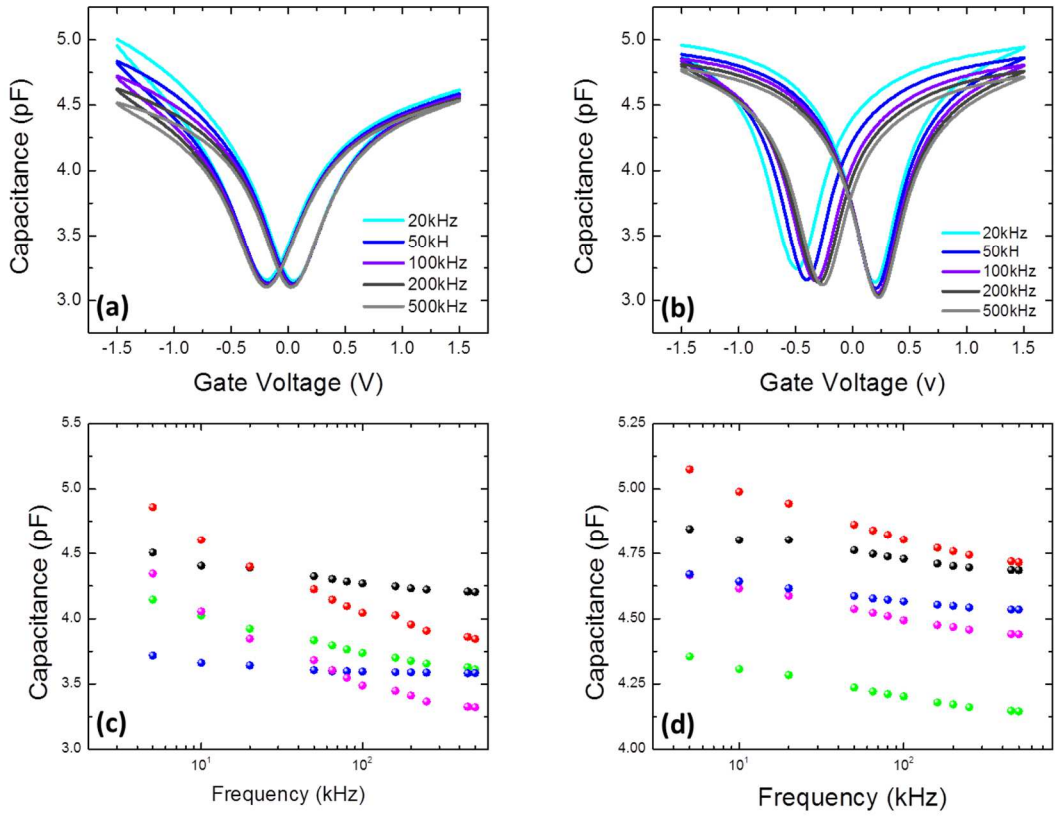


Figure 5-9: Varactor measured capacitance vs. gate voltage (up and down sweeps) at different frequencies ranging (20 -500 kHz); (a) At vacuum, (b) Fully functionalized. Measured capacitance versus the log frequency for the same device in (a-b) at two different applied voltage points under the following conditions: vacuum (blue ), air (black) before functionalization; linker (green), GOx (magenta), and deactivation (red) all at ambient atmosphere after (c) Dirac point , and (d) at +1.5V.

The effect of functionalization on GFET performance was also studied and the $I_D$-$V_G$ data is shown in Figure 5-10. Figure 5-10(a) shows $I_D$-$V_G$ curve at each stage of the functionalization for GFET with 40 µm width and 10 µm channel length. Figure 5-10 (a-b) shows an optical image and Raman mapping for the same GFET. It is important to notice that there is a reduction in the total current which is likely due to partial delamination and breakage at the edges of the graphene sheet. As those edges are the current access points, the electron transport path becomes narrower therefore the total

drain current becomes smaller. In other words the access resistance increases and that reduces the source-drain current value. The total area however stays roughly the same; consequently the total capacitance is left unaffected by those breakages.

In addition, extracting the device mobility is challenging because of the inconsistent width of the device as depicted in Figure 5-10(c) [82], [124], [125].

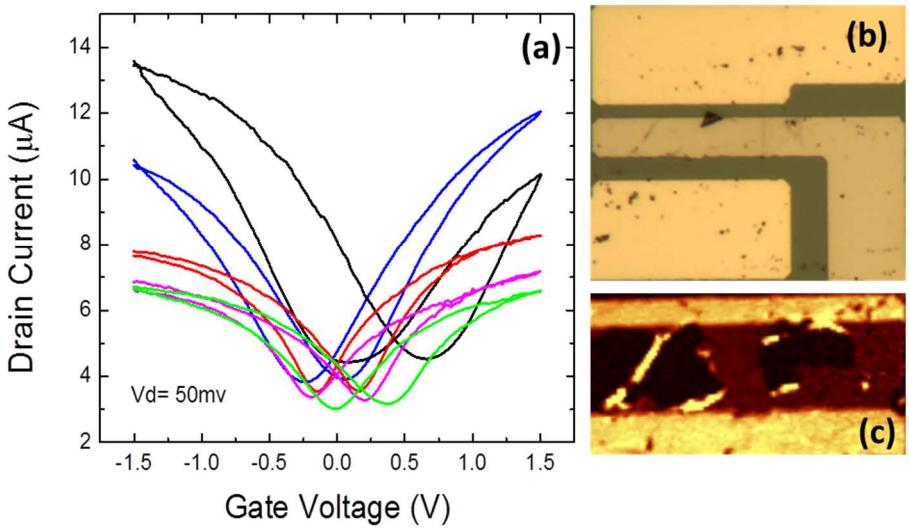


Figure 5-10: GFET results (a) Drain current versus gate voltage at $V_d$ = 50mV under the following conditions: vacuum (blue ), air (black) before functionalization; linker (green), GOx (magenta), and deactivation (red) all at ambient atmosphere after (b) Top-view optical micrograph picture for the GFET device in (a); (c) Raman mapping for the same device in (b).

### 5.3.3Extracted trends

Measuring the quantum capacitance at each step of the functionalization is a powerful tool to monitor the change in the density of states and the disorder in graphene. In order to understand the previously demonstrated responses at each step of the functionalization, the effective temperature model from chapter 3 is utilized. The increase in the tuning range is related to both the increase of the maximum capacitance and the decrease of the

minimum capacitance (capacitance at the Dirac point); the former is related to the change in the EOT, while the latter is related to the decrease in the disorder. Both $T_0$ and EOT parameters can be extracted from the effective temperature model at each stage of the functionalization to obtain a quantitative measure of the change. This model was discussed in detail in chapter 3. It might be useful to remember that $T_0$ is related to $C_q$ by

$$C_q = \frac{2q^2 k_B T_{eff}}{\pi(\hbar v_f)^2} ln\left[2 + 2\,cosh\left(\frac{E_f}{kT_{eff}}\right)\right], \qquad 5\text{-}1$$

where

$$T_{eff} = \sqrt{T_0^2 + T^2}\,. \qquad 5\text{-}2$$

Once again 500 kHz was chosen as the frequency to carry out the fitting since it is approximately at this frequency that the excess capacitance disappears and that the C-V characteristics are roughly symmetric about the Dirac voltage. Such an approach is justified assuming that the excess capacitance at negative voltages is due to interaction with border traps [78]. In addition only the reverse sweep was considered for this analysis. As was demonstrated in chapter 3, the fitting procedure needs to normalize the capacitance to the device active area. Some of the areas were found through fitting the data in vacuum (the closest to the ideal), while others were estimated by utilizing Raman mapping as shown in Figure 5-11. The SEM was not used in this case as the effect of the electron beam on the functionalization is unknown. Furthermore, in this analysis there was no hysteresis correction because the vacuum data did not show much of hysteresis and the other hysteric effect is probably related to the effect of ambient environment on the sample, which will be discussed later in this chapter.

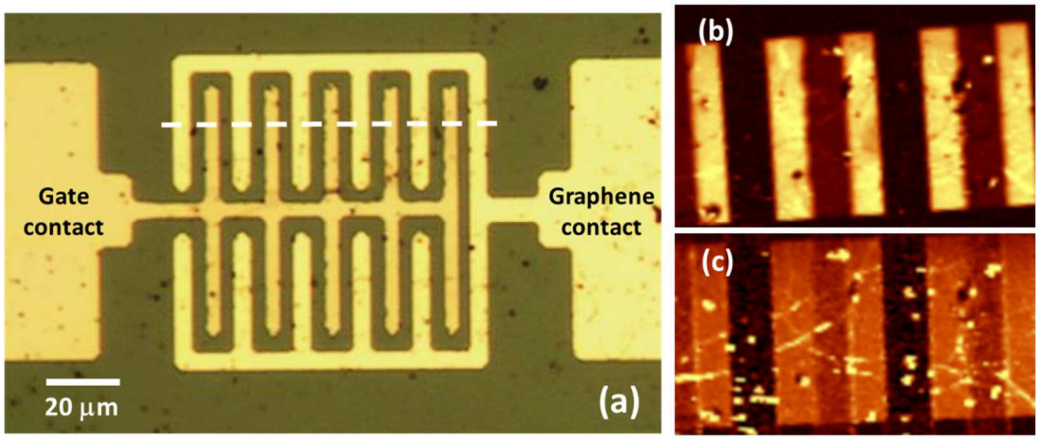


Figure 5-11: (a) Optical micrograph image of one of the varactors in this study . Raman spectroscopic 2D map of a portion of the graphene varactor in (a). (c) shows the G peak, while (d) shows the 2D peak.

The extracted values of the both the EOT and $T_0$ are shown in Figure 5-12. The average obtained value for EOT in vacuum is 4.70 ± 0.05 nm. The EOT decreases in air to average 4.3±0.2; it is important to notice that this case has the highest fluctuation for a reason that will be clarified later. Once the linker molecules are attached to the graphene surface, the EOT increases again, but then decreases throughout the functionalization process, returning to an average value of 4.28 ± 0.11 nm, which is nearly identical to that measured in air before functionalization. The trends in the disorder parameter are as the following: in vacuum, $T_0$ = 479 ± 50 K, a value that corresponds to random potential fluctuations with standard deviation on the order of 58 meV. The $T_0$ value increases substantially to 711 ± 70 K for non-functionalized devices in ambient atmosphere, but decreases again upon initial attachment with linker molecules, and then continues to decrease through the GOx attachment and deactivation steps, finally reaching $T_0$ = 406 ± 103 K, a value that is lower than that in vacuum. Moreover, the lowest extracted $T_0$ = 292 K for a graphene device was extracted from a fully functionalized device in Figure 5-13 [78].

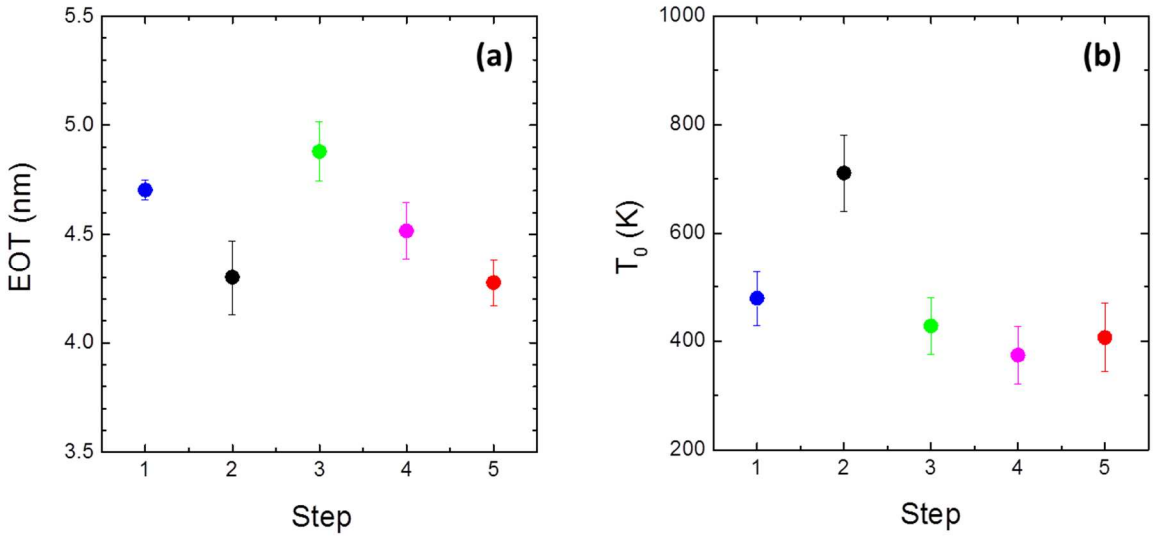


Figure 5-12: Extracted parameters compiled from graphene varactors as a function of the functionalization in order step (1,2,3,4,and5) as vaccum, air,linker,GOx, and deactivation respectively . The extracted parameters are (a) EOT and (b) $T_0$. The error bars indicate the standard deviation of the extracted values obtained over seven devices.

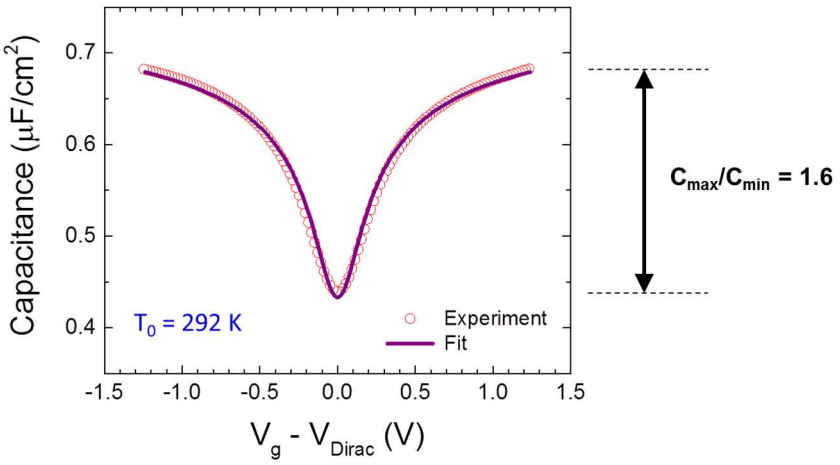


Figure 5-13: Comparison of fit vs. experimental C–V characteristics for one device measured after completion of the surface functionalization. The open symbols represent the experimental data and solid line shows the theoretical result using fitting parameters of EOT = 4.42 nm and $T_0$ = 292 K.

The fact that the disorder is less after the functionalization than it was in vacuum is not fully understood. One possibility is that the higher dielectric constant of the $H_2O$ intercalated layer modifies the Fermi velocity in graphene, which is similar to previous studies on graphene with few-layer ice deposited on top [126]. Other work studying the effect of fluorinated polymers deposited on graphene has shown similar effects [24]. Moreover, since there was no chemical mechanical polishing step in the device fabrication process, it is reasonable to assume that the $HfO_2$ has a rough surface. This surface roughness could have added to the disorder in graphene. The infiltrated water molecules however could have bridged over the terrace of the $HfO_2$ thus have smoothened the surface, which has led to a decrease in the disorder that supersedes the vacuum condition. The source of those water molecules is the ambient humidity in the room, as those measurements took place in air. The humidity in these experiments was not controlled; therefore the relative humidity is unknown. The next section will provide further evidence on the water intercalation hypothesis.

### 5.3.4 Water intercalation hypothesis

In order to explain the previously demonstrated trends, it is important to remember two criteria about those devices. First, there is a gap between the graphene and the $HfO_2$ [78], [87]. Second, the graphene sheet in our devices has some breaks and tears that could function as an access point for water molecules in the ambient atmosphere. The gap that causes the disparity between the EOT extracted from the MIM to the ones extracted from the MOG was explained in chapter 3. Once this device is exposed to air, this gap can be filled with a layer or more of water molecules. Though water molecules are not expected to diffuse through carbon atoms in graphene, water molecules can laterally accumulate beneath the graphene sheet through the breaks and tears in the graphene sheet [108]. This water intercalation hypothesis could explain the previously observed trends. When the sample is in vacuum there is no water beneath or on top of the graphene, consequently the EOT is still about 1 nm higher than it is from the MIMs because the vacuum gap dialectic constant is ~1. Once the sample is taken out of the vacuum chamber the water can infiltrate the gap through the breaks and tears, which results in decreasing the EOT because the dielectric constant of water is larger than 1. In addition to the water beneath the graphene, there is an adsorbed film of water molecules on top of graphene. Those molecules are distributed in a position and orientation that maintain a steady state condition relative to the atmosphere. Therefore those molecules are the ones responsible for increasing the disorder as they are expected to be distributed randomly.

During the functionalization progress the water on top gets replaced with the linker molecules, however the water underneath the graphene remains in place to. Figure 5-14 depicts those steps. If the water layer dielectric constant is ~80 and the physical distance between the graphene and the $HfO_2$ is about 0.3nm then the expected decrease in the EOT is more than 1nm; however our results show ~0.4nm decrease. This apparent discrepancy is possibly because the dielectric of one layer of water is not the same as bulk water [128]. Furthermore, the gap between $HfO_2$ and graphene could have been

widened to accommodate the water molecules; therefore the physical thickness is more than the predicated value of ~0.3 nm. [78], [87]. Moreover, the noticeable increase in the hysteresis upon measuring in air is another evidence of water infiltration between the graphene and $HfO_2$, as it was reported before the effect of water on the hysteresis in GFET in [129]. On the other hand these hysteretic effects can be suppressed if the substrate was hydrophobic unlike $HfO_2$ which known for its hydrophilicity [130].

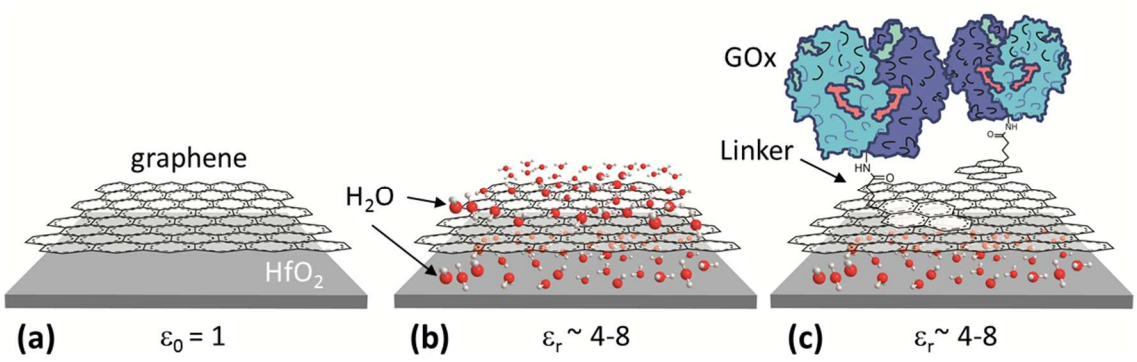


Figure 5-14: Cartoon illustrates the proposed mechanisms for experimentally observed behavior. (a) The device in vacuum where the gap between $HfO_2$ and graphene has a dielectric constant of ~1. (b) The device in air before functionalization in which water molecules has intercalated in the gap between $HfO_2$ and graphene as well as physisorbed $H_2O$ on top of the graphene (gap dielectric constant increases). (c) The device in air after functionalization in which water molecules are still in the gap between $HfO_2$ and graphene but functionalization prevents $H_2O$ interaction on the graphene surface.

To further validate the above hypothesis we sought a physical characterization method. This method is based on utilizing AFM to see if the water layer beneath the graphene can be detected. In this physical characterization study, an exfoliated graphene flake was utilized to avoid any residues associated with CVD graphene, which can complicate the AFM data interpretation [71], [78]. ALD $HfO_2$ was deposited onto a $Si/SiO_2$ wafer to replicate the surface conditions in the fabricated devices. Next, graphene flakes from HOPG were exfoliated onto the $HfO_2$ surface. Tapping-mode AFM was then performed on the exfoliated piece just after the exfoliation. The initial result is shown in Figure 5-15(a). Here, it was found that the graphene is multi-layer but sufficiently flat. The step

height can be accurately determined, and an average step height of 5.49 nm was determined by fitting the height histograms extracted from the AFM data Figure 5-15(f-j). The condition in Figure 5-15(a) most accurately replicates the varactor ambient atmosphere conditions. After imaging, the sample was then baked under the same conditions as the varactor samples, and immediately measured again by AFM under dry nitrogen atmosphere, as shown in Figure 5-15(b). After the baking process, the step height reduced to 4.37 nm. The post-bake condition is believed to be an accurate representation of the vacuum conditions, as the sample was purged with dry nitrogen upon removal from vacuum and maintained in the atmosphere throughout the imaging process. This imaging procedure was then repeated for each of the three stages of the functionalization Figure 5-15(c-e), and the resulting step heights are as follows: linker (5.70 nm), GOx (5.48 nm) and deactivation (4.98 nm). The initial reduction of step height after high-temperature bake supports the hypothesis that $H_2O$ intercalates beneath the graphene when exposed to ambient atmosphere, presumably entering from the edge of the graphene flake. These results are generally consistent with those of [14]. The strong hydrophilic nature of $HfO_2$ suggests that the presence of $H_2O$ (as opposed to another molecule) is the most likely event. As was hinted to before, the $H_2O$ can access the devices from a number of exposed edges in the devices as well as intermittent rips and tears in the CVD graphene. The increase in the step height after functionalization further bolster the trends presented before, assuming that the intercalated water below the graphene has a relative dielectric constant between (4-8) as was mentioned in Figure 5-14 [78]. This is a reasonable assumption for a water layer, though further studies are needed to determine the precise dielectric constant of this underlayer film [78], [131]. Since line scanning can be misleading, a statistical approach was utilized to observe on average the difference in the step height at each stage of the functionalization. Therefore corresponding histograms were generated by plotting the number of points at any given height in the scanned window at each stage of the functionalization, as shown in Figure

5-15(f-j). For example the peak ~ 4nm indicates the number of points at 4 nm while the other peak around ~10 nm indicates the number of points with 10 nm height. On average the difference between the peaks represents the increase in the height due to the water intercalation.

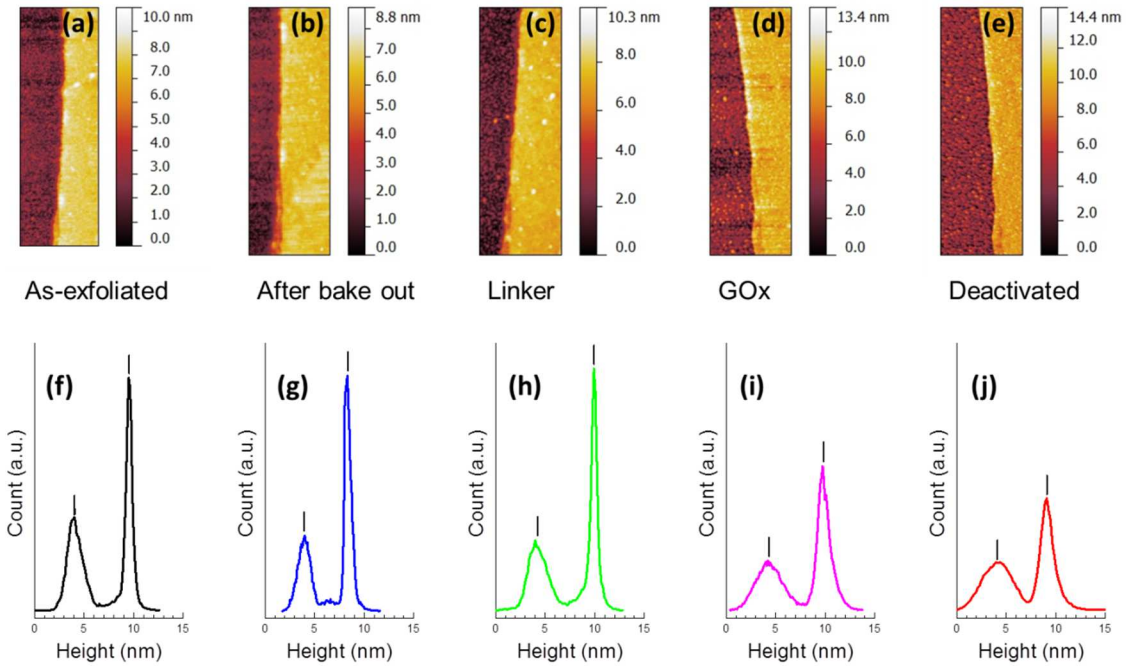


Figure 5-15: AFM date on exfoliated graphene after different stages of functionalization. (a-e) AFM false color maps (a-e). (f-j) height histograms profile generated to corpspond to the color map in (a-e) respectively. The lables in the middle are for both top, and bottom plots.

All the previous experimental observations along with the hygroscopic nature of $HfO_2$ and the previously-reported water diffusion under graphene layers support the feasibility of water layer intercalation between the graphene and the $HfO_2$. One might question the variation in the EOT and wonder if we could consider the EOT to be constant at all stages of functionalization, and relate the change in the tuning range or maximum capacitance to the carrier concentration in the system and residual charges. This idea however won't provide us with an accurate understanding of the system. Since adjusting the residual

carrier density does not reproduce the increase in capacitance far from the Dirac point. Therefore only the decrease in the disorder can explain the restoring of the minimum capacitance value, and in turn the enhancement in the C-V curve shape. While the increase in the maximum capacitance, and consequently the tuning range, can only be explained by the decrease of the EOT.

Finally, the shift of the Dirac point in Figure 5-7(a-b) toward more positive value in ambient atmosphere is consistent with intercalation of water under the graphene, as this water is expected to occupy the oxygen vacancies in the $HfO_2$ and thus make them unavailable for doping the graphene, which is consistent with previous results that have reported a p-type doping effect associated with physisorption of $H_2O$. The trend toward decreasing Dirac voltage is consistent with displacement of $H_2O$ on the graphene surface by the linker molecule. Moreover, the hydrophobicity of the local environment at the graphene surface is expected to increase as functionalization progresses, consistent with the gradually decreasing Dirac voltage. Lastly, the Dirac point does not completely return to the neutral point observed in vacuum, even upon full functionalization. Figure 5-16(a) summarizes the movement of the Dirac point.

The effect of oxygen molecules above or beneath the Dirac point in graphene was theoretically studied. The first principle density functional theory (DFT) calculations, has estimated a partial density of states (PDOS) versus Fermi-level for non-functionalized $HfO_2$/graphene system with different numbers of vacancies as in Figure 5-16(b). As the number of vacancies increases the more n-type the graphene will become. Once the sample is moved to air, the oxygen molecules in air cause p-type doping effect, because oxygen molecules act as acceptors. The PDOS curve with extra oxygen molecules shows a p-type doping effect on graphene as in Figure 5-16(c) [78], [87], [132][108]. More on the effect of oxygen molecules and water on the Dirac point in graphene is discussed in the next chapter.

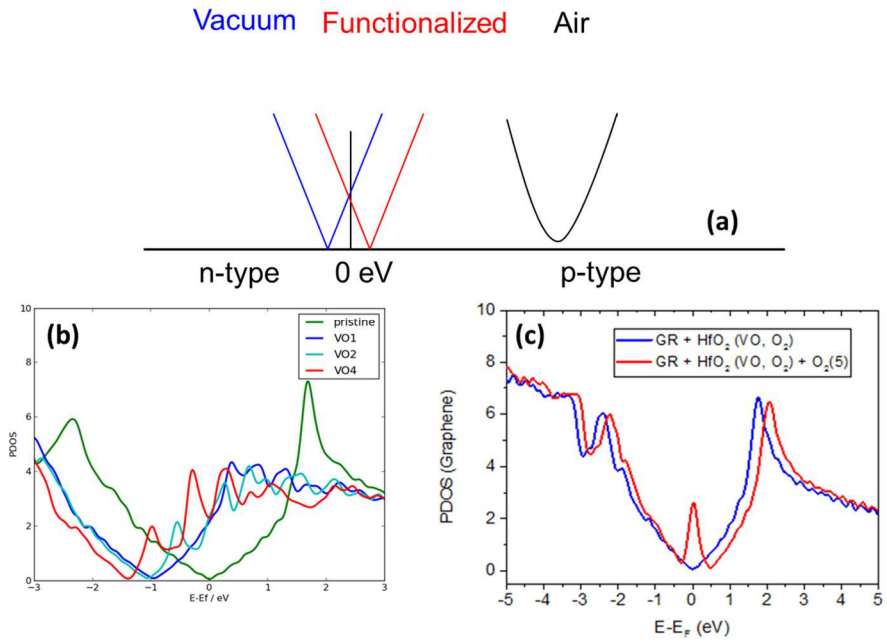


Figure 5-16: DFT calculations results: (a) schematic cartoon to illustrate the Dirac point shift at the main stages of the experiment. (b) PDOS versus Fermi-level for graphene / $HfO_2$ with $HfO_2$ with : zero, one, two, or four oxygen vacancies respectively similar to the vacuum condition. (c) PDOS versus Fermi-level for graphene/$HfO_2$ with one oxygen vacancy to mimic the measurement in air at two different conditions. First, with only one water molecule and one oxygen molecule on top (blue). Second, with only one water molecule, and five extra oxygen molecules on top.

## 5.4 Summary

In conclusion, the effect of surface functionalization of 1-PASE/GOx on graphene varactors performance was studied. The electrical and physical analyses show that not only does the functionalization has not degrade the varactor performance but also tends to improve the capacitance tuning range. Both C-V measurements and AFM data suggest that when the device is measured in air before functionalization, water molecules will infiltrate in between graphene and $HfO_2$ which is quite possible considering the hydrophilicity of $HfO_2$ [123]. The trapped layer of water causes two changes; first, it decreases the n-type doping effect by the substrate oxygen vacancies. Second, it increases the total capacitance because of the difference in the dielectric constant of water to vacuum that will decrease the EOT of the device. Meanwhile, the oxygen molecules in air reside on top of graphene and cause a p-type doping effect, and possibly an increase in the disorder as they are randomly distributed over the graphene sheet (non-uniform doping). These extra charges could create extra states at the Dirac point and smear the quantum capacitance. Once the functionalization starts it replaces both the oxygen and water molecules on the top of graphene, hence decreases the disorder and the p-type doping. However the water molecules underneath the graphene continue to exist. The slight decrease in the total capacitance after adding the linker is suspected to be an initial hydrophobicity that was introduced to the substrate as it was submerged in the linker solution for two hours, but once the sample is removed from it and exposed to air multiple times the water molecules will intercalate again and increase the total capacitance. More details on water effect will be presented in the next chapter.

# Chapter 6 :
# Effect of Humidity on Graphene Varactors

*"At sufficiently high humidity a continuous molecularly thin water film wets the interface between the graphene and mica. At lower humidities the film dewets with fractal depressions exhibiting dimensions around 1.7 and depths comparable to the size of a water molecule." N. Severin et.al Nano Letters, 2012, 12 (2), pp 774–779.*

## 6.1 Introduction

### 6.1.1 Research goals

As was presented in the previous chapter the effects of the ambient conditions, especially water and oxygen molecules on the graphene varactors are very important. Those effects play an important role in the MOG electrical characteristics such as Dirac point and capacitance tuning [78]. Therefore studying the effect of humidity on the graphene varactors serves more than the purpose of introducing a new vapor sensor device. It also shines more light on the graphene varactor interfaces and the device stability in ambient conditions. There are several studies on graphene device applications as a vapor sensor [38], [39], [46], [133]. This chapter, however, focuses on the humidity effect on graphene varactors. First, the wireless graphene based vapor sensor is presented, in which both the Dirac point and the capacitance are indirectly measured, through the shift in the resonant frequency. Second, a study of a wired graphene based vapor sensor is presented in which the capacitance versus voltage is measured directly and continuously as the humidity changes [108]. In both cases systematic changes are observed, and the feasibility of utilizing this device to be a vapor sensor is high. In addition those experiments have revealed important information on the interactions between the graphene and $HfO_2$ and between the graphene and both water and oxygen molecules [39].

## 6.2 Indirect measurements

### 6.2.1 Measurements setup

In order to explore the sensitivity of the graphene varactors to water vapor, a variable-humidity test setup was constructed. In the initial experiments, the devices were integrated with inductors and tested wirelessly using near-field inductive coupling. This experiment set up is quite different from the previously discussed measurements. Here the device was measured in an open flow chamber. The chamber is connected to a source of air (dry or moist), and to a commercial humidity sensor is used to monitor the humidity as in Figure 6-1(a). The semiconductor analyzer used in this study is an impedance analyzer (Agilent 4291B) as this measurement is a wireless measurement, thus it requires a read-out coil that is connected to the impedance analyzer as in Figure 6-1(b).

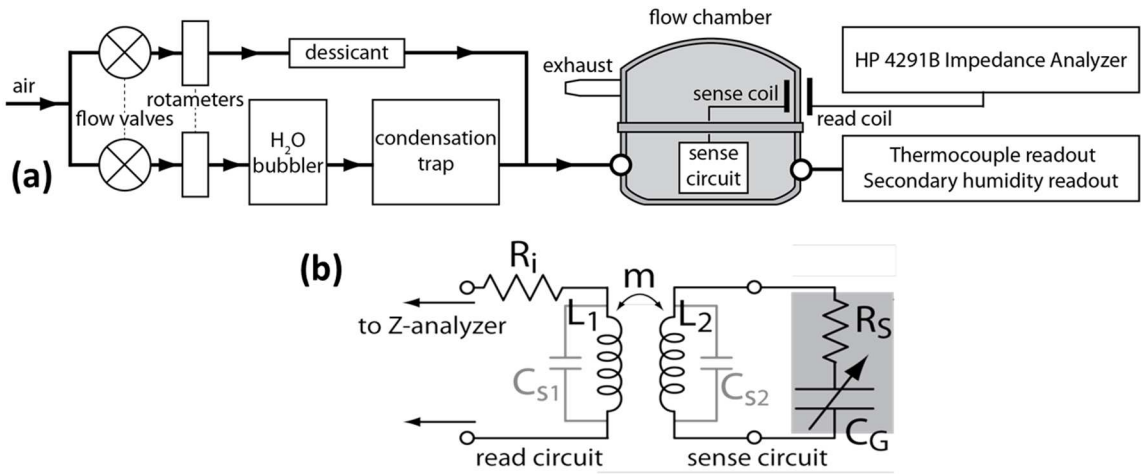


Figure 6-1: (a) Cartoon that shows the wireless measurement apparatus. (b) Circuit diagram for the sensing circuit utilized in this work.

The experiment starts by wire-bonding five varactors with gate widths of 40 µm or 100 µm and different numbers of gate fingers on the same sample in parallel to obtain

maximum capacitance. High capacitance is needed to exceed the self-capacitance from the read and sense coils and to set the sensing resonance frequency in the desirable range. The devices then were wire-bonded to a printed circuit board (PCB) with copper leads that are coupled to a ferrite-core inductor. Prior to the humidity experiment, the device was baked at 380 K in vacuum to remove adsorbed water during fabrication. Capacitance–voltage (C–V) measurements were taken on the wire-bonded varactor prior to removing from vacuum. The C–V curves were taken at 1MHz in vacuum on the parallel varactors prior to the inductor wire bonding. The C–V curve in Figure 6-2 shows that the capacitance values rang between ~80-95 pF with 1.2:1 tuning range. More importantly, the device has a slightly positive Dirac voltage; therefore the curve exhibits the steepest slope near zero, which is required to attain high sensitivity with the resonant circuit. A fitting procedure was applied to the C-V curve obtained from the measurements in vacuum, and several parameters were extracted such as EOT =2.52 nm and $T_0$ =1500K and the total extracted area was 7975 μm$^2$. These parameters were extracted in similar manner as was described in chapter 3 [22].

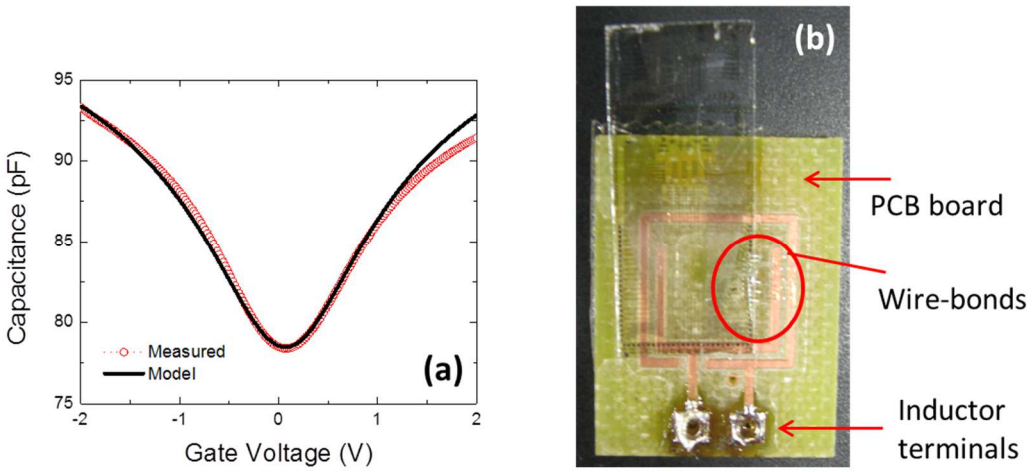


Figure 6-2: (a) Measured and modeled capacitance vs. voltage characteristics for the sensing device, the measurement frequency is 1 MHz. (b) Micrographic image of the sensor device on the PCB board consisting of 5 multi-finger graphene varactors wire bonded in parallel [22].

Once again $T_0$ is the measure of disorder in the quantum capacitance equation as in

$$C_q = \frac{2q^2 k_B T_{eff}}{\pi(\hbar v_f)^2} \ln\left[2 + 2\,cosh\left(\frac{E_f}{kT_{eff}}\right)\right], \qquad 6\text{-}1$$

and $T_{eff}$ is given by

$$T_{eff} = \sqrt{T_0^2 + T^2}\,. \qquad 6\text{-}2$$

After removing the device from vacuum, the device is mounted inside the chamber with its own sensing coil as shown in Figure 6-1. A second inductor was placed outside of the chamber in close proximity to the sensor so that good coupling was achieved between the two inductors. The relative humidity in the chamber is controlled by mixing water-saturated air (~100%) and dry air (~0%) from two different lines. The frequency-dependent impedance of the external inductor was then measured as a function of relative humidity (RH), where the RH value was verified using a commercial humidity monitor. A stable RH can be achieved by monitoring the flow rate with rotameters and carefully controlling the ratio of wet and dry air inserted in each line. Water-saturated air was produced by passing compressed air through a diffusing stone immersed in deionized water, while dry air was produced by passing compressed air through a chamber packed with anhydrous calcium sulfate as a drying agent. To prevent condensed droplets of water from entering the sample chamber, a condensation trap was included in the water-saturated line immediately before mixing the wet and dry stream. The measurement started by bringing the relative humidity in the chamber to minimum (~1% humidity) according to the commercial humidity sensor (Electro-Tech Systems Model 514 humidity controller), then the water vapor line was opened to start increasing the humidity in the chamber. The phase of the impedance of the external inductor was then monitored using the Agilent 4291B impedance analyzer, which was coupled to the sensor through

inductive coupling. Next, the humidity was increased gradually every 30 seconds, and the actual reading from the commercial humidity sensor was recorded along with the phase and frequency data from the impedance analyzer. After the humidity reached 97%, the wet air-line was closed and the dry air-line was opened to decrease the humidity in the chamber. The phase versus frequency was recorded during both ramps, and in another experiment it was recorded for random humidity levels [49].

### 6.2.2 Measurement observations

The sense circuit in Figure 6-1(b) is a resonance LC circuit that has a resonant frequency. Since the impedance analyzer is connected to the read coil the phase versus frequency curve has a dip as a result of switching between the -90º at the resonance frequency of the sensing LC circuit back to the +90º of the reading coil [134]. The resonant frequency value mainly depends on the lumped circuit elements (LRC). The total impedance in LRC circuit can be defined as:

$$Z_T = R + j(X_L - X_C), \qquad 6\text{-}3$$

where $X_L = \omega L$ , and $X_C = \frac{1}{\omega C}$ .

At resonance $X_L = X_C$ and therefore:

$$f = \frac{1}{2\pi\sqrt{LC}}. \qquad 6\text{-}4$$

In this work, the impedance distribution is more complicated. The frequency-dependent input impedance for the coupled readout and sensor circuit shown in Figure 6-1, using the transformer equations for the inductively coupled circuit, is given as

$$Z_{in} = Z_1 + \frac{\omega^2 m^2}{Z_2 + R_S + \frac{1}{j\omega C_G}}, \qquad 6\text{-}5$$

where $R_S$ and $C_G$ are the varactor series resistance and capacitance respectively, and $Z_1$ is the impedance on the reading side of the circuit and it can be defined as

$$Z_1 = R_i + \frac{j\omega L_1}{1 - \omega^2 L_1 C_{S1}}. \qquad 6\text{-}6$$

In addition, $m$ is mutual inductance between the read coil and the sense coil and it is defined as:

$$m = k\sqrt{L_1 L_2}, \qquad 6\text{-}7$$

where $L_1$ (1.16μH), and $L_2$ (645nH) are the read-out, and sensor coil inductances respectively and k is the coupling coefficient. $C_{S1}$ (2.16pF), and $C_{S2}$ (2.3pF) shown in Figure 6-1 are the self-capacitances of the read-out, and sensor coils. Finally $Z_2$ is the impedance of the circuit on the sensing side and it can be defined as:

$$Z_2 = \frac{j\omega L_2}{1 - \omega^2 L_2 C_{S2}}. \qquad 6\text{-}8$$

Since the sensor-side LRC circuit is the one that has a minimum at its resonant frequency, the following plots of impedance phases are plots of the phase of $Z_1$ vs. frequency. For the LRC circuit used in this experiment, the phase dip (phase minimum) occurs at 18MHz.

The first set of experiments were performed in a dry environment, then in high humidity, and then again in dry conditions. Here, the "dry" state corresponds to ~ 1% RH, with the "humid" state occurring at RH = 95%. This procedure was achieved by bringing the chamber RH to full equilibrium before the measurement was taken. A clear reversible shift to lower resonant frequency was observed as the humidity increased as in Figure 6-3(a). A shift of ~ 0.5MHz between the dry and humid conditions was observed. Figure 6-3(b) shows the measured impedance magnitude for both dry and humid conditions. Furthermore time-dependent measurements were performed where the device response to the instantaneous change of the humidity in the chamber was considered by changing the humidity every 30 seconds and recording the resonant frequency shift. In Figure 6-3(c) two resonant frequencies as a function of time profiles are plotted which correspond to successive measurements of the graphene sensor on different days. Figure 6-3(d) shows the RH vs. time plot measured using a commercial humidity sensor. The time response of the resonant frequency follows an approximate exponential curvature.

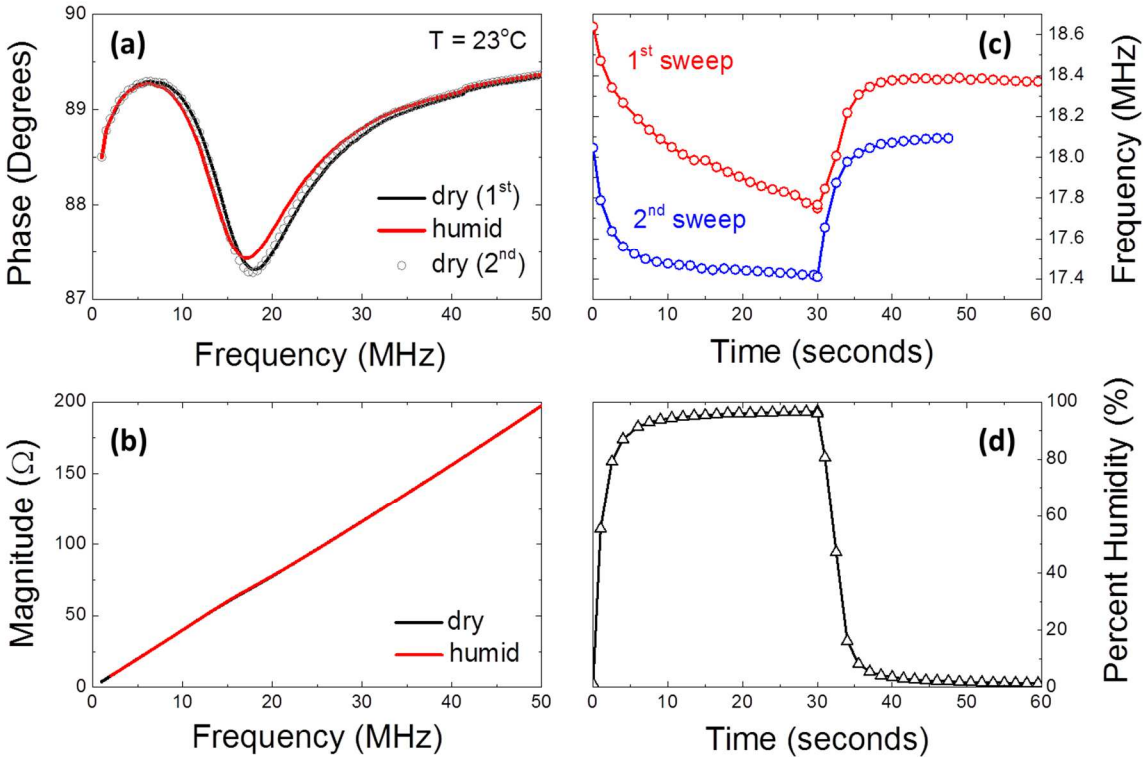


Figure 6-3: Plot of external inductor impedance phase versus frequency for successive measurements in dry (1% RH), humid (97% RH) and dry air. (b) Plot of external inductor impedance magnitude for the first two dry and humid conditions in (a). (c) Resonant frequency shift vs. time for two successive measurements where the RH was switched from the dry to humid states. The first profile (Red) was taken immediately after baking out in vacuum, while the second profile (Blue) was performed after cycling the sensor between dry and humid conditions numerous times. (d) RH vs. time plot measured using a commercial humidity sensor [22].

In the first profile in which the sample was just removed from vacuum (completely dehydrated surface) it can be seen that the resonant frequency does not return to its original value after humidity cycling. The second profile however, was taken after cycling the sensor between dry and humid conditions several times. The resonant frequency does return to its original value. There is about 400 kHz shift between the first and the second profiles. The better stability in the second profile was explained by reaching surface equilibrium, specifically $HfO_2$ surface equilibrium, as in the first profile the device was freshly dehydrated. Once the sample is in the chamber the water

intercalates slowly into the gap between the graphene and $HfO_2$ which causes an initial drift. After the device has been exposed to humidity several times however, the layer of water that had already intercalated stabilizes.

Next the reproducibility and the consistency of responding to humidity was investigated. In this section, three sets of experiments were performed on the same sample, same day, but at different times. First the humidity in the chamber was brought to its RH maximum and data was taken every 30 seconds. Next the measurements started from the minimum RH that was reached at the first experiment and increased again the RH to its maximum point. The third experiment followed a random profile in which the data were taken at random RH points. The results of those experiments are all summarized in Figure 6-4. One can notice that the frequency shift versus the humidity concentration is roughly linear with a slope of -6.2 + 0.1 kHz / % RH despite to the taken course. Furthermore, the random profile slope frequency shift vs. concentration plotted in Figure 6-4(c) fits almost exactly between the profiles corresponding to the increasing and decreasing humidity sweeps. The latter observation is related to a small but non-negligible hysteretic mechanism. This hysteric effect causes the frequency shift to be dependent on the direction of the concentration ramp. The obtained linear dependence of the frequency shift on humidity was not necessarily expected, as noted originally in reference [23]. Rather, the precise functional dependence is expected to depend upon numerous factors, including the interaction of the adsorbed molecules on the graphene surface, the precise shape of the C–V profile and the initial ”doping” in the graphene [49].

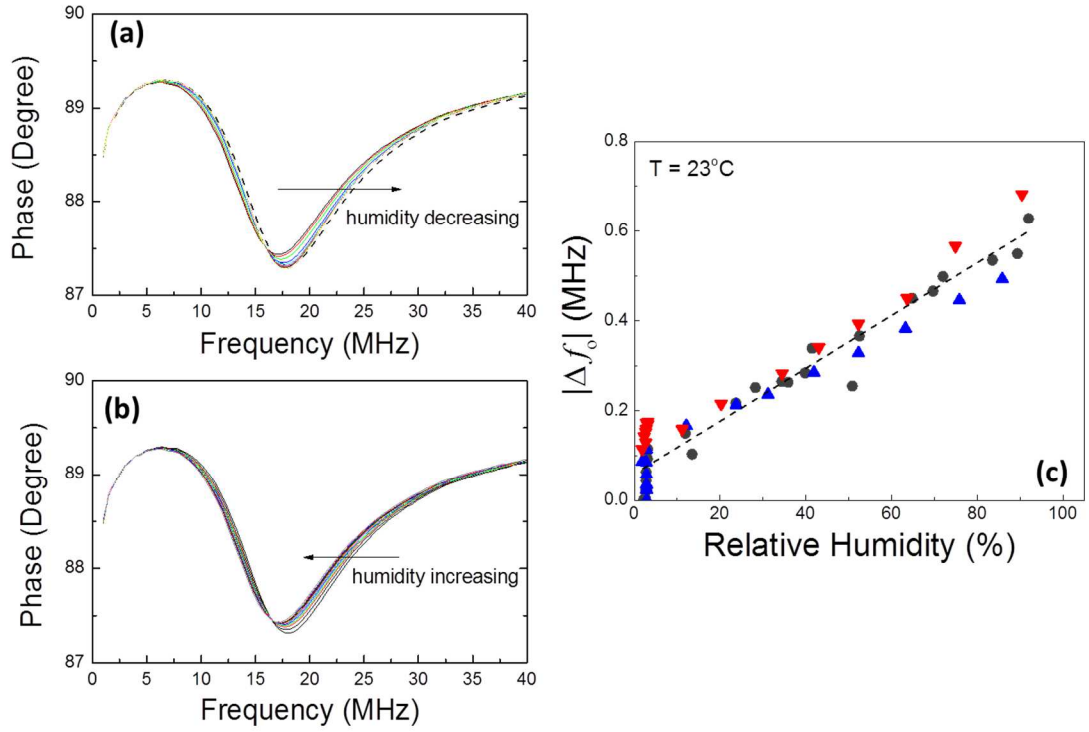


Figure 6-4: Impedance Phase versus Frequency plot for: (a) the decreasing RH cycle.(b) the increasing RH cycle (c) Dependence of resonant frequency shift vs. RH measured using three different concentration sequences: increasing, decreasing and random. The dashed line shows a linear fit including all three measurement sequences [22].

The total capacitance in the sensing circuit must have increased, since the resonance frequency in equation 1-2 becomes smaller as the humidity level increases. The inductance in the coil does not change with humidity. The indirect measurements of capacitance versus humidity indicates a change in the phase vs. frequency that is consistent with the increase or the decrease of the humidity, a trend that is very consistent and repetitive [49]. The change in this minimum with the humidity level change can be interpreted as a change in $C$ but not in $R$ or $L$ as $R$ and $L$ are both physically fixed elements and cannot be function of humidity. The total capacitance ($C_{tot} = (C_{ox}^{-1} + C_q^{-1})^{-1}$), of the varactor is the only variable element. The total capacitance, however, consists of quantum capacitance and oxide capacitance. Since the capacitance

versus voltage was not directly measured, the source of the change could be from $C_q$ or $C_{ox}$ or a mix of both. Only a direct measurement of the capacitance versus voltage while changing the humidity level could reveal the source of the change. One might argue that the resistance in the sensing device could be a function of humidity; as a matter of fact most if not all the graphene based sensors are resistive based sensors [39], [43], [46]. A fitting procedure was applied in which both the capacitance and the resistance values versus humidity were extracted as in Figure 6-5. The results showed a change of ~1Ω for the resistance, and that is not enough to cause a shift of 5MHz in the resonance frequency. The fitting procedure was based on the same equivalent circuit as in Figure 6-1(b). The fitting parameters were the resistance and capacitance of the graphene varactor, the read inductor resistance and coupling coefficient between the two inductors. All other parameters were measured independently. The values of $R_i$ and k were used as free fitting parameters, where values of $R_i$ = 0.093 Ω, $k$ = 0.16 were determined in all cases. Finally, it is important to note that in our wireless sensor paper [49], we had originally hypothesized the intercalated water layer to be stable throughout the experiment; therefore the frequency shift was due to the quantum capacitance effect. However in our subsequent experiments, we realized that the situation is much more complex.

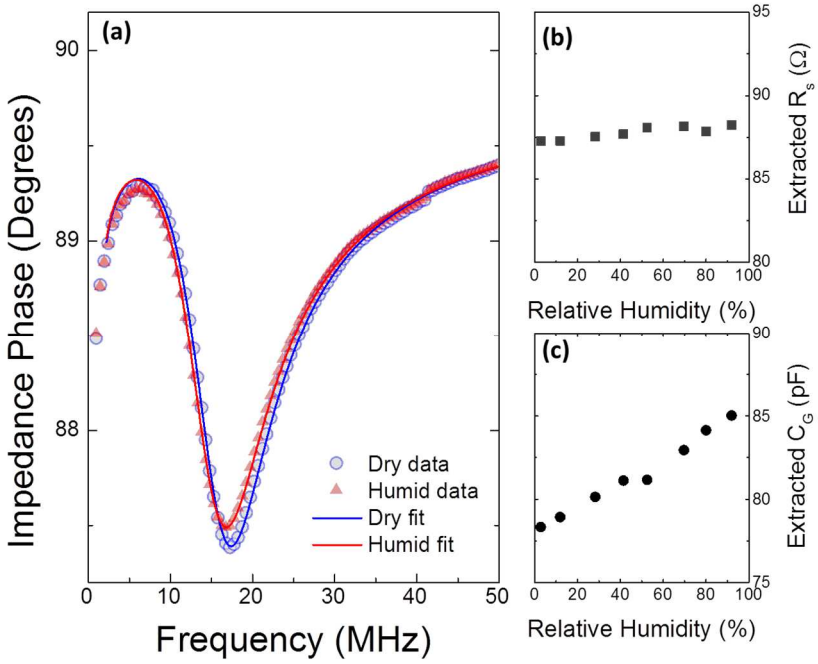


Figure 6-5: (a) Measured phase dip under dry and humid condition along with the results of the fitting model. Extracted (b) resistance and (c) capacitance of the graphene varactors vs. RH using the fitting procedure shown in (a), [22].

## 6.3 Direct measurements

### *6.3.1 Measurement setup*

The previous section presented a change in the resonant frequency that depends on the humidity level. There is no doubt that there was a consistent trend there, yet the source of this trend is arguable. The performed experiments using graphene varactors showed resonant frequency (and thus capacitance) change as a function of relative humidity. Though, the physical nature of the interaction between water and the graphene surface was not necessarily clear. It was speculated that the capacitance change was due to a Dirac point shift, as has been observed in resistive based graphene sensors before.

However, the experiments on graphene varactors functionalization in chapter 5 suggested that the intercalated water molecules between the $HfO_2$ and graphene can affect the capacitance behavior as well, though those experiments were not performed under controlled atmospheric conditions [23], [78][108].

In this section a wired measurement setup was used, Figure 6-6 shows a test chip mounted on a header in the measurement chamber. This chamber is smaller in size, which allows the RH to reach equilibrium in a shorter time. In this setup the test chip is mounted on the header and a single device or several are wire-bonded so they can be connected through coaxial cable to the B1500A. A commercial humidity sensor and a thermocouple are also included in the chamber to monitor the RH and the temperature. The same setup in Figure 6-6 can be used for wireless experiments as was demonstrated in the previous section by wire bonding the device to a sensing coil and mounting a reading coil out of the chamber but in close proximity to it. The RH humidity level was controlled by adjusting the flow rates of water-saturated air and dry air. Water-saturated air was produced by bubbling compressed air through warm deionized water and dry air was produced by passing compressed air through a calcium sulfate desiccant. As the humidity levels were swept from high to low and vise-versa the voltage across the device was also swept between -3V and 3V, and the C-V characteristics were recorded about 1000 times per run. The frequency dispersion was not considered in this study as sweeping multiple frequencies would have taken a much longer time. Therefore the C-V characteristics were obtained at only one frequency.

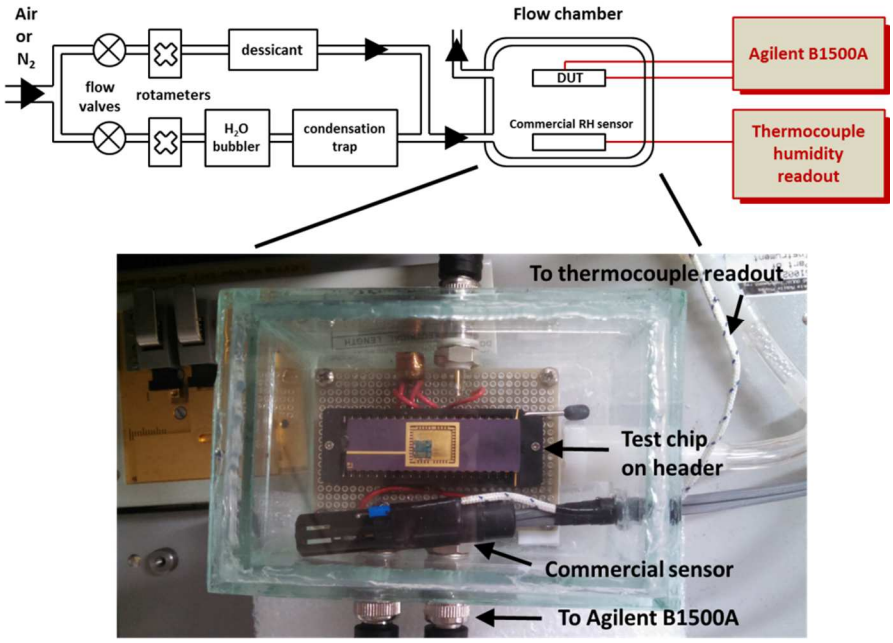


Figure 6-6: (Top): Diagram of wired humidity sensing measurement apparatus. (Bottom): Photograph of the humidity sensing chamber.

### 6.3.2 Measurement observations

Figure 6-7 shows the result of cycling the humidity levels on a single finger device with gate width of 40µm and length of 30µm. Figure 6-7(a) shows full C-V sweeps at RH=74% and 2.8%. While Figure 6-7(b) shows the full sweeps at 44% and 0.6%. It is important to notice, that both the Dirac point and the maximum capacitance are shifting. The maximum capacitance is increasing as the RH is increasing and the Dirac point is shifting to the left as the RH is increasing. Figure 6-7(c) shows the reading from the commercial humidity sensor versus time. Figure 6-7(d-f) show the time evolution of $C_{max}$, $C_{max}/C_{min}$ and $V_{Dirac}$ for both up and down sweeps respectively. Three observations can be made from this plot. First, both the tuning range and maximum capacitance continue to increase as the RH increases. The tuning range reached 1.6:1 which is the highest recorded value in our devices. This enhancement is suspected to be partly because

of the less disorder, as the water molecules beneath the graphene are more ordered than the $HfO_2$ molecules. This hypothesis is supported by the observed enhancement in graphene's mobility both when it is suspended or on top of crystalline h-BN [51], [75], [79], [135], [136]. Though the DFT/MD calculations in chapter 5, show that the water layer beneath widens the distance between the graphene and the dielectric, is believed that the more layers of water, the higher the dielectric constant of water can be (as the dielectric-constant of bulk water is higher than a single layer of water) [128]. Second, the Dirac point shifts to a more negative value as the humidity gets higher, which is Contrary to the common belief that humidity positively dopes the graphene. Third, the C-V curve hysteresis increases proportionally to humidity, and this observation in particular agrees with our previous results in chapter 5 [78], [129], [137][108]. Finally, one can notice that $C_{max}$ does track the humidity with an adequate accuracy; at lower RH levels however, there is a small drift in the $C_{max}$ values, similar to the one that was observed in the resonance frequency shift at low RH [22][108].

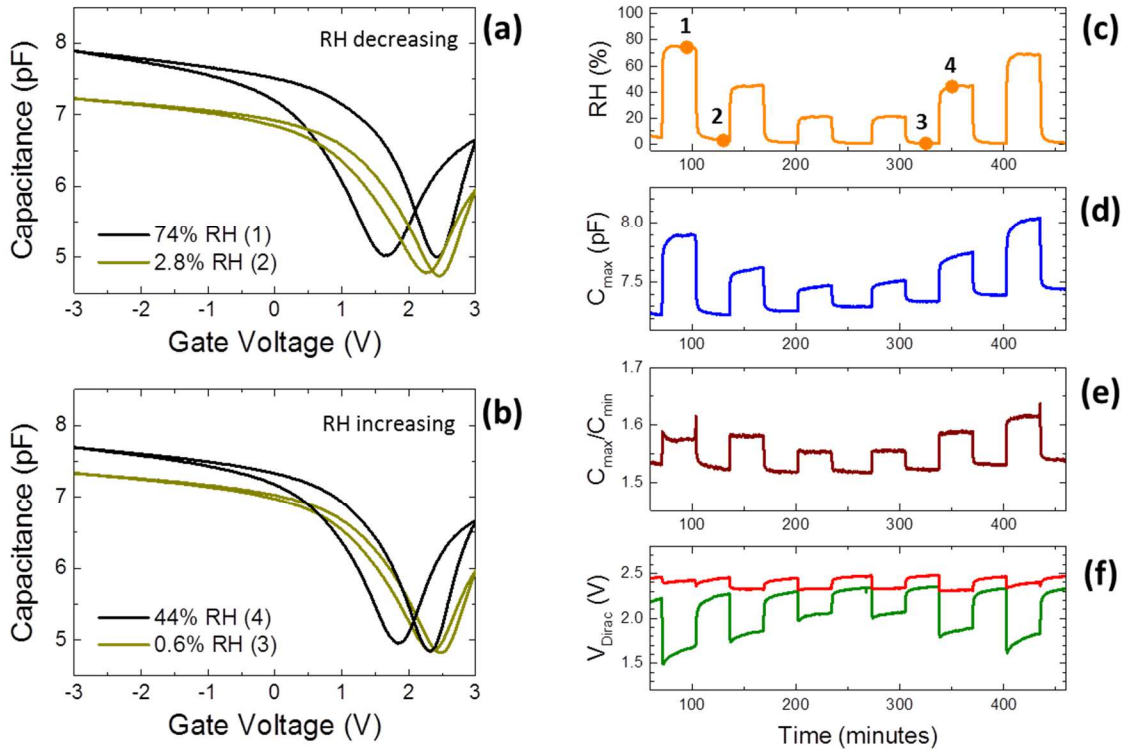


Figure 6-7: (a)-(b) Plot of capacitance vs. voltage for a graphene varactor for (a) decreasing relative humidity and (b) increasing relative humidity, where the plots correspond to the data points on the RH vs. time plot in (c). (d) Plot of maximum capacitance, $C_{max}$, (e) maximum to minimum capacitance ratio, $C_{max}/C_{min}$ and (f) Dirac voltage, $V_{Dirac}$ for increasing (green) and decreasing (red) voltage sweeps vs. time corresponding to the RH sequence in (c) [108].

## 6.4 Results discussion

### 6.4.1 Overview

In the indirect measurement (wireless measurement) the change in the frequency or the frequency shift with the humidity level change was assumed to be based solely on change in the quantum capacitance due to the Dirac point shift. This is based on the premise that

the change in the humidity level shifts the Fermi-level in graphene (doping the graphene) [49]. This explanation however assumes a relatively constant $C_{ox}$ at all times.

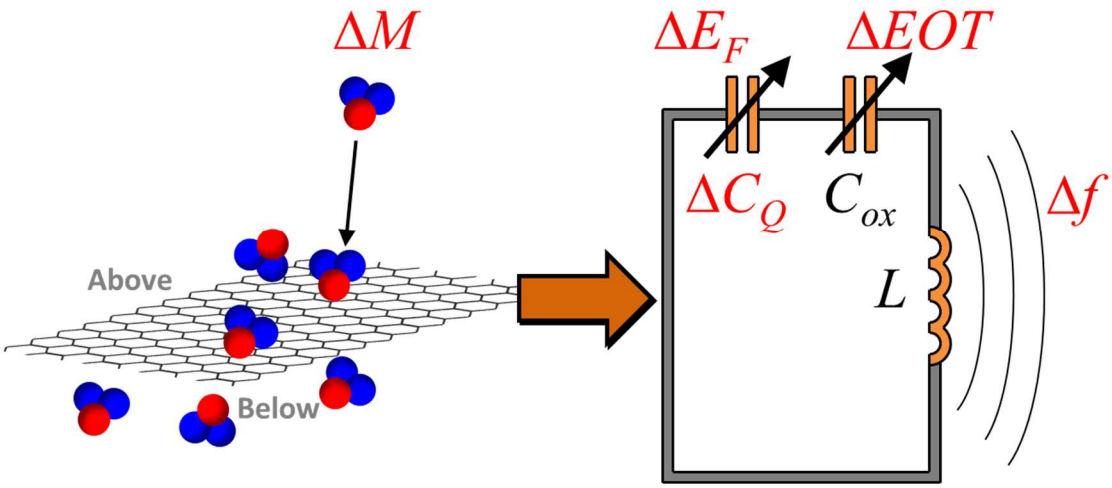


Figure 6-8: Cartoon shows the previously concluded behavior of the wireless graphene vapor sensor ΔM is the change in the water molecules density above and below the graphene sheet ( gray), $\Delta E_f$ represents the change in in doping in graphene, ΔEOT represents the change in the dielectric thickness, both cause change in the resonant frequency $\Delta f$.

In direct measurements, on the other hand, the change in the total capacitance was obviously strongly related to the RH level. However the physical nature of the interaction between water and the graphene surface was not immediately clear. Once again the intercalated water versus the water on top of graphene needed to be further investigated. As they both respond to the change in the humidity, in other words the water molecules above and below the graphene sheet affect the quantum and the oxide capacitance respectively as depicted in the cartoon in Figure 6-8.

### 6.4.2 Water molecules effect

From the indirect measurements, the increase in the RH level leads to a decrease in the resonant frequency that can be only explained as an increase in the total capacitance. The

direct measurement has also shown an increase in the total capacitance proportional to the RH increase. In light of the results in chapter 5, both measurements point towards water intercalation between the graphene and $HfO_2$ [78], [121]. The increase in the total capacitance with RH can be explained by an increase in the effective $C_{ox}$ of the device. Even though intercalation of water into the interfacial layer would result in a larger distance between the gate-oxide and graphene since the interfacial water is expected to have a larger dielectric constant than vacuum, the effective oxide thickness is expected to decrease compared to the case where a vacuum gap exists. The observed increase in the hysteresis with increasing humidity is also consistent with trapped moisture underneath the graphene. To further support this hypothesis, a physical observation to the increase in step height as a function of RH has been performed. AFM experiment was applied, similar to the one that was performed in chapter 5 with a very important twist: observing the change in the graphene step height as a function of the RH. The water intercalation was observed in the previous chapter and confirmed with the AFM experiment. However, the relationship between the water layers thickness and RH levels was not explored. In addition, multilayer exfoliated graphene was used before to avoid misinterpreting the data because of PMMA residues. In this study of the intercalated water molecules between the graphene and $HfO_2$ relative to the humidity level, monolayer CVD graphene was used. AFM scan was applied on a sample of CVD graphene on 7nm ALD $HfO_2$, which was deposited on 300nm $SiO_2$ on Si- substrate. To avoid PMMA residues from the transfer process, the graphene surface was scanned in a contact mode with a high tip force to mechanically remove the residues and create a hole in the graphene surface that will be an access point for the water molecules. Later an AC (pulsed) mode was used to scan the same area at different humidity levels. Figure 6-9(a) shows the targeted area in the indicated rectangle after imaging, a histogram of all the heights in the targeted area was extracted at two humidity levels. Figure 6-9(b) shows high humidity (RH=90%) condition histogram, while Figure 6-9(c) shows the low humidity (RH=2%) condition

histogram. Both peaks were then fit to two Gaussian distributions corresponding to the substrate and graphene heights and the step height from the oxide substrate to graphene was calculated as the distance between the peaks. This procedure was crucial to compensate for the roughness of both the underlying $HfO_2$ as well as the PMMA residues on the graphene. The results in Figure 6-9(d) shows how the step height increases as the RH level increases as expected. A drift in the baseline step height similar to the drift in base capacitance in Figure 6-9(e) was also observed. These images clearly suggest that the source of the capacitance increase in these devices is related to the $C_{ox}$ because of the water infiltration under the graphene at high humidity [108].

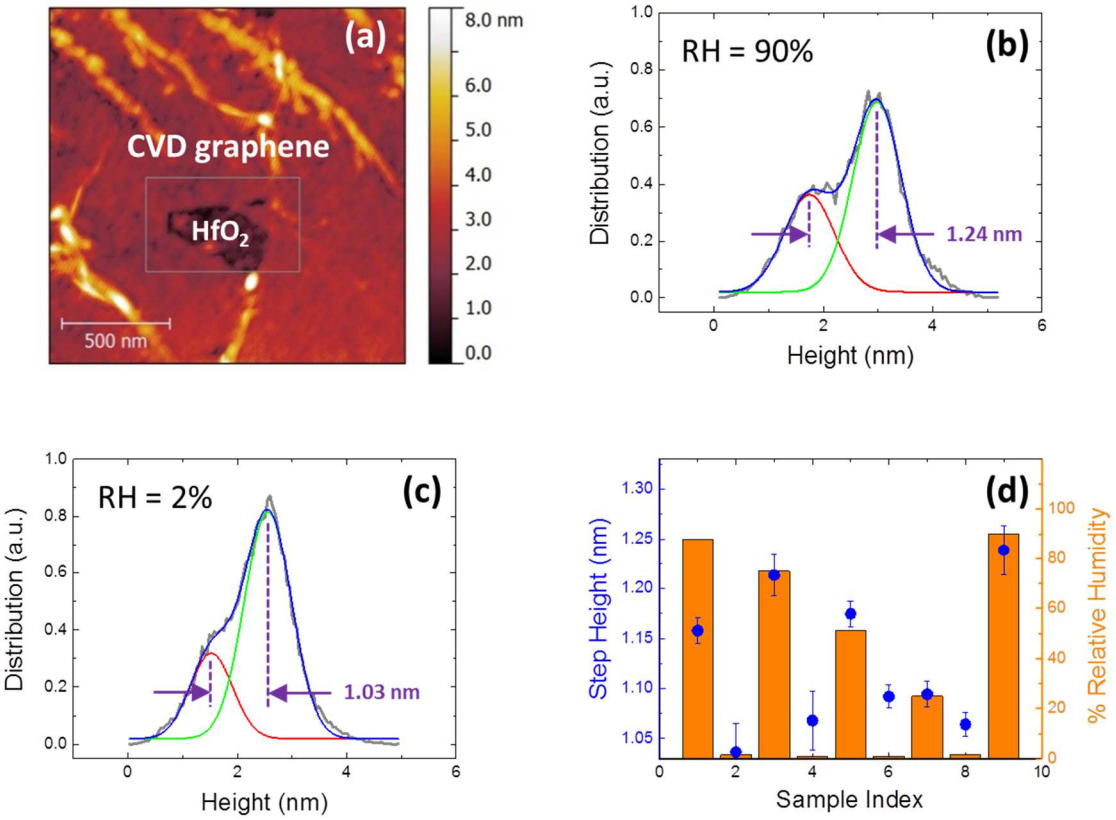


Figure 6-9: (a) Atomic force microscopy scan of CVD-grown graphene on $HfO_2$ (b) Height distribution map for the indicated rectangular region in (a) for RH = 90%. The scans have been fit using two Gaussian distributions and where the difference in the peak heights is indicative of the step height between the graphene and $HfO_2$. (c) Height distribution map for the indicated rectangular region in (a) for RH = 2%. (d) Height of CVD graphene relative to the $HfO_2$ for a sequence of measurements under different RH conditions.

It is important to remember, that the roughness of the $HfO_2$ plays a role in increasing the disorder which on the other hand increases the quantum capacitance, thus lowers the tuning range, as was discussed in chapter 3. The intercalated water could provide a smoother surface for the graphene, which enhances the tuning range [78], [138], [139].

To further validate the mechanism of the water intercalation into the gap between the graphene and $HfO_2$, A combination of a first principle calculation and a molecular

dynamics (MD) simulation for the interactions that are relevant to our devices, was done by Aluru's group at the University of Illinois Urbana Champaign. Their results show the water molecules moved from above the graphene sheet, through the breakages and tears to fill the gap between it and the $HfO_2$. Figure 6-10 captures the motion of water intercalation using MD simulation for a piece of graphene that has a cut in it, as a solid continuous sheet of graphene is impassable for water. Furthermore the water molecules widen up the gap between the graphene sheet and $HfO_2$, which was observed in the AFM experiments [108]. MD simulation confirms that water molecules can intercalate into the $HfO_2$–graphene interface as water molecules get introduced to the $HfO_2$–graphene system. This result is expected considering the relatively high hydrophilicity of $HfO_2$ [21], and is consistent with the increase in total capacitance at high humidity in Figure 6-7. DFT and structural optimization of the system shows that the separation between the graphene and $HfO_2$ surface increases by approximately 2.3 Å upon addition of four water molecules into the interfacial layer.

It is clear from the previous results how the intercalated water molecules affect both the tuning range ($C_{max}/C_{min}$) and increase of the $C_{max}$. However the Dirac point shift relationship with the intercalated water is still not very clear. The results from density functional theory (DFT) and molecular dynamics (MD) simulations indicate that the introduction of a single water molecule under the graphene results in a rather large doping effect upon the graphene while subsequent additions provide very little additional doping.

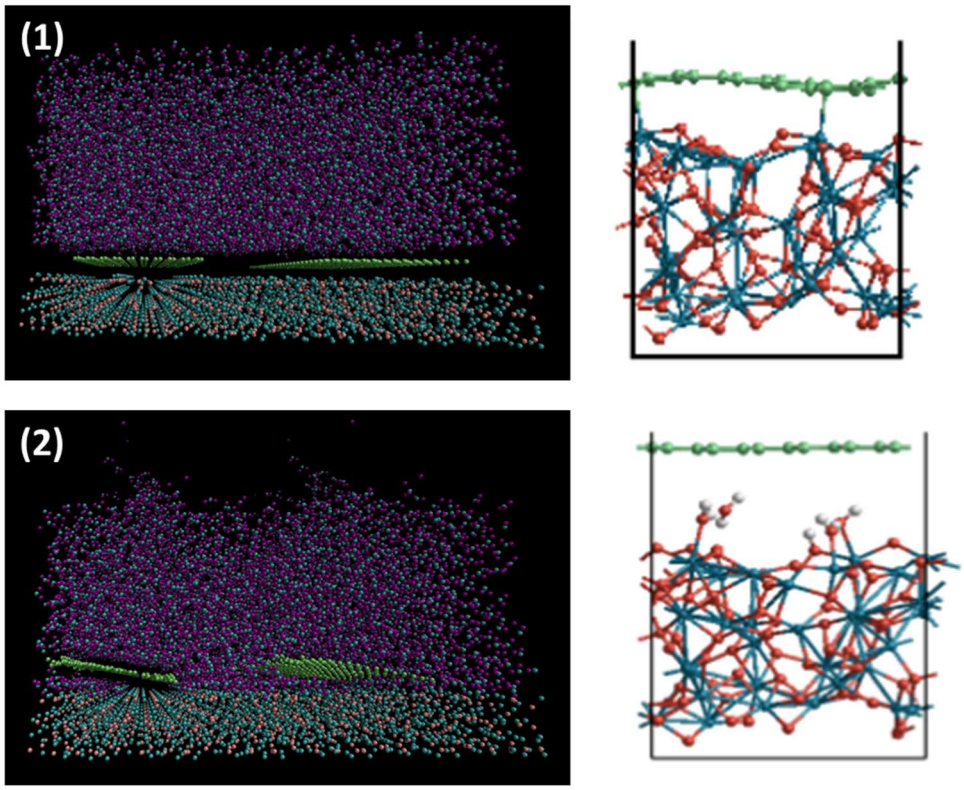


Figure 6-10: MD simulation that shows the water intercalation between the graphene sheet and the $HfO_2$. (1) Water molecules only on top of the graphene/$HfO_2$. (2) The water molecules intercalated between the graphene and $HfO_2$. The figures on the right show the effect of the water molecules on the gap between the graphene sheet (green) and $HfO_2$ (red and blue).

Moreover, simulations of water on top of graphene reveal no significant charge transfer between water and graphene. Furthermore the water molecules beneath the graphene interact with the oxygen vacancies in the $HfO_2$ which affects the Dirac point value [78], [97], [140]. The more water molecules infiltrate between the graphene and $HfO_2$ the further the graphene sets from the $HfO_2$ which weakens the interaction between the two [108]. The water molecules on top of graphene however, do not display any significant change in the doping level according to the simulation results.

To better isolate the effect of water molecules from the effect of oxygen molecules, and further track the source of the shift in the Dirac point relative to the humidity cycling, an experiment comparing dry air and dry nitrogen was conducted.

### 6.4.3 Oxygen molecules effect

The shift of $V_{Dirac}$ to more negative voltages in the presence of increasing humidity could be more related to the oxygen vacancies in the $HfO_2$ than it is to water molecule [87]. To better understand these results, our collaborators performed DFT and MD simulations of the graphene interactions that mimic the conditions that our device has been through. In each simulation, the atomic structure is first optimized by minimization of the free energy of the system. After optimization, the local density of states (LDOS) of the graphene monolayer was calculated. The first investigated system is the interaction of graphene with amorphous $HfO_2$. For this system, a sheet of graphene containing 48 carbons over $HfO_2$ was considered to be large enough to approximate bulk graphene. Under conditions where the amorphous $HfO_2$ is pristine (no oxygen vacancies), the graphene experiences no net doping effect from the oxide (black-line) in Figure 6-11(a). To mimic the actual $HfO_2$ in our case, four oxygen vacancies were added to the oxide surface. Here a substantial n-type doping effect is observed (red-line), which is consistent with the results previously obtained by ab initio simulation of the graphene–$HfO_2$ interaction obtained by W. L. Scopel, *et al.* [87]. This n-type doping is a direct result of a partially covalent interaction between the unpaired electrons on the oxygen and the pi electron system of graphene. Because this interaction has a largely covalent character, it results in a rearrangement of the hybridization of a $sp^2$ carbon to $sp^3$ [108].

In the case of humidity, the calculation of the partial density of states (PDOS) reveals that the n-type doping that had been introduced by oxygen vacancies in the $HfO_2$ was eliminated by introducing water molecules into the interface between the graphene and

$HfO_2$, as shown in (blue-line) Figure 6-11. To investigate the effects of dry air, water vapor and dielectric substrate on the electronic properties of graphene, the n-type doping effect on graphene was confirmed to be due to oxygen vacancies (VOs) on $HfO_2$ surface, which is consistent with the literature. Then $O_2$ absorption on the defective sites of $HfO_2$ surface was studied, which could fill VOs and cause graphene to be neutral. In addition, as the humidity increased, more $H_2O$ molecules were placed on top of graphene, occupying the positions of original $O_2$, and the density of $O_2$ above graphene was decreased compared to pure $O_2$ case (magenta-line) Figure 6-11. Finally the change of graphene doping when different number of $H_2O$ and $O_2$ were sitting above it was investigated. It should be noted that as more $O_2$ molecules were replaced by $H_2O$, graphene exhibited weaker p-type behavior.

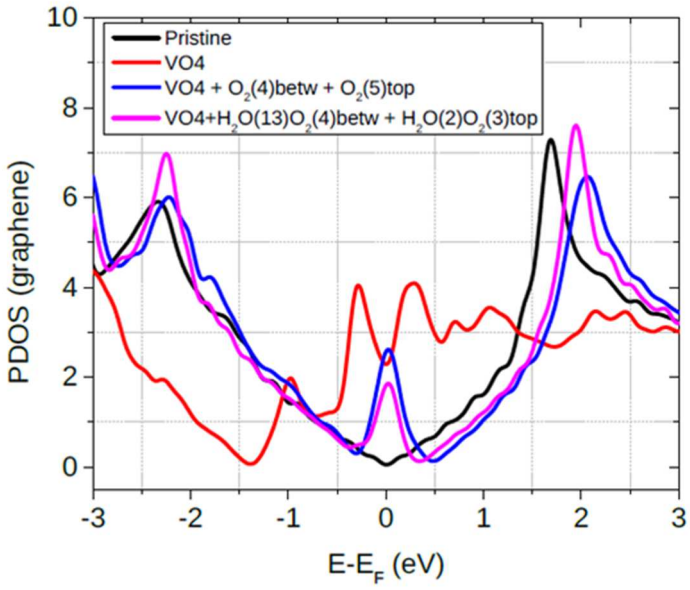


Figure 6-11: PDOS versus Fermi-level in graphene based on (DFT) calculations for different (color coded) scenarios.

Since dry air has about 23% oxygen, there is a chance that the shift in the Dirac point is more related to the oxygen molecules in the air than it is to the layer of water above the

graphene. Therefore replacing dry air with dry nitrogen can shed some light on the origin of the shift. The experiment was preformed several times on 8-finger MOG varactors with finger length of 40μm and width 5μm; as always two separate sweeps (RH increasing and RH decreasing) were run through two different gas setups. At first the moisture was passed though desiccated air. In the second experiment the moisture was mixed with dry $N_2$. Figure 6-12 shows the results of the experiment. By comparing (b) to (f) one can notice that the change in the maximum capacitance is almost the same; similar observations can be said on the tuning range. The shift in the Dirac point on the other hand is clearly different; the Dirac point in the desiccated air case is relatively more positive than it is in the case of the nitrogen. Figure 6-13 shows the results of the same experiment, but the order of the gases was reversed. Though the same observations hold, the Dirac point in general is less positive in the case where the nitrogen was passed first. These results provide strong evidence that the oxygen in the air also influences the device behavior.

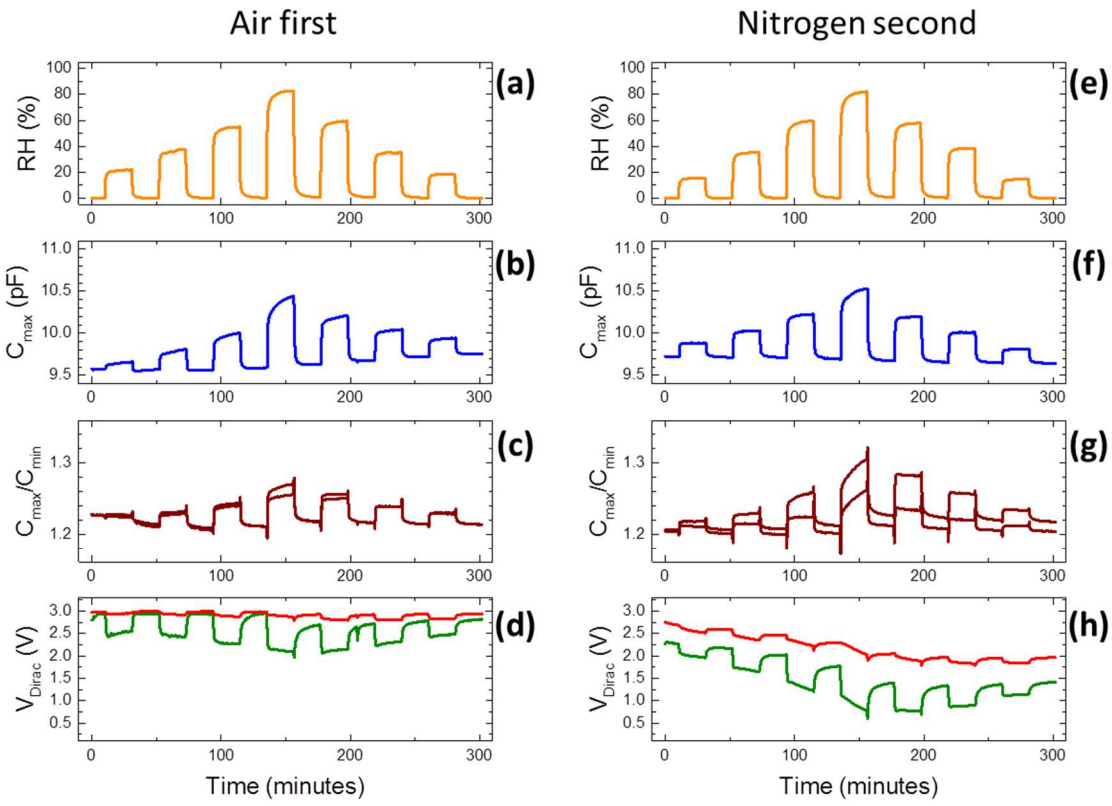


Figure 6-12: Comparison of MOG humidity sensing characteristics with air being (first) carrier and $N_2$ (second) (a) Plot of relative humidity, (b) maximum capacitance, $C_{max}$, (c) maximum to minimum capacitance ratio, $C_{max}/C_{min}$ and (d) Dirac voltage, $V_{Dirac}$ for increasing (green) and decreasing (red) voltage sweeps vs. time with desiccated air as the carrier gas. (e)-(h) Plot of same parameters as in (a)-(d).

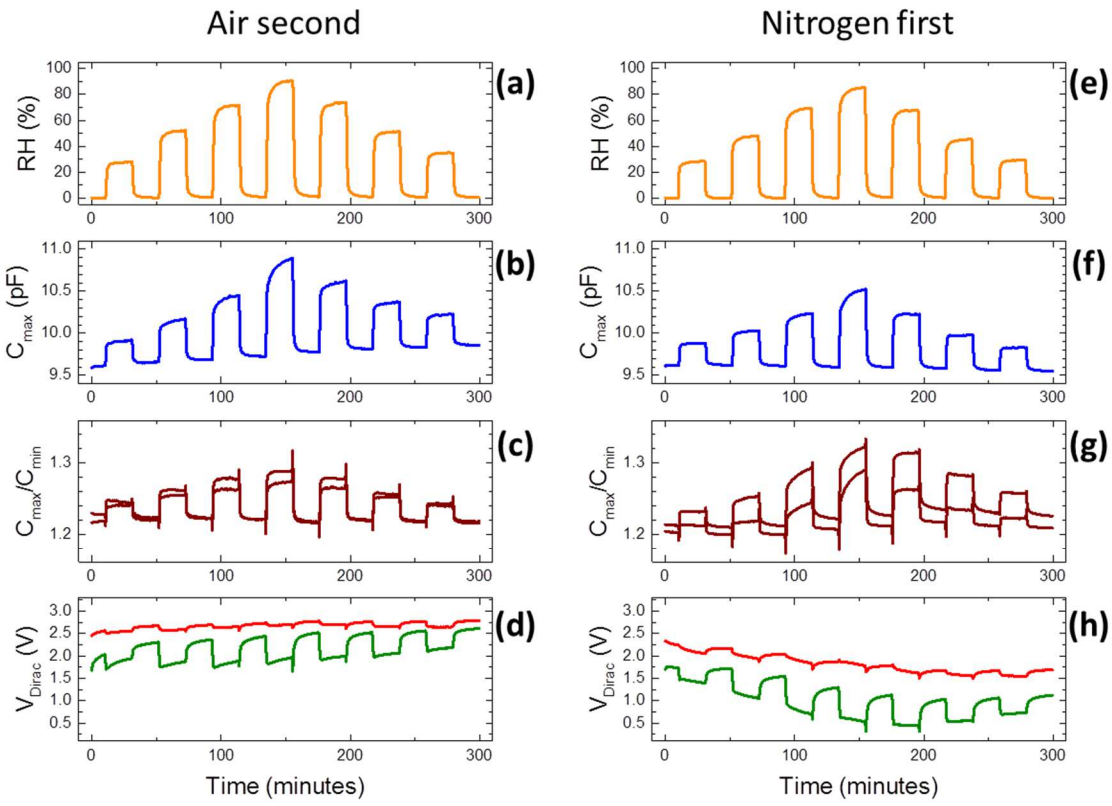


Figure 6-13: Comparison of MOG humidity sensing characteristics with $N_2$ being (first) carrier and air (second). (a) Plot of relative humidity. (b) Maximum capacitance, $C_{max}$. (c) Maximum to minimum capacitance ratio, $C_{max}/C_{min}$. (d) Dirac voltage, $V_{Dirac}$ for increasing (green) and decreasing (red) voltage sweeps vs. time with desiccated air as the carrier gas. (e)-(h) Plot of same parameters as in (a)-(d).

## 6.5 Summary

Graphene-based varactors that utilize the quantum capacitance effect as their operating mechanism have been fabricated and shown to operate promisingly as passive, wireless vapor sensors. Through the quantum capacitance effect, the resonant frequency of the resulting LC circuit shifts in response to the $H_2O$ vapor concentration, as determined using a secondary readout inductor. The shift in resonant frequency was found to be linearly dependent on vapor concentration over a relative humidity range of 1 to 95%. Moreover, the response was shown to be reversible and stable upon repeated concentration cycling. Furthermore, water was found to have a major effect on varactors electrical characteristics. Surprisingly the water intercalation mechanism is a fast mechanism and it does track the RH levels with an adequate accuracy. There is still a degree of drift in the results possibly because the water access points are random and not designed for that purpose. More investigation is needed with more controlled access points. Finally the oxygen has a strong effect on the Dirac point not just because of the oxygen vacancies in the $HfO_2$ but also the oxygen molecules above the graphene that can p-type dope the graphene [138][108].

# Chapter 7 :
# Conclusion and Outlook

*"Graphene is like the 'Philosopher's stone' … 'Whenever you touch any phenomena with graphene, then there is always something new and something unique. It is really a very rich system, which we have not experienced before." Andre Geim - Nobel Lecture, 2004.*

## 7.1 Graphene varactors conclusion

### *7.1.1 Overview*

Graphene is a two-dimensional sheet of carbon that has many unique and interesting properties. One of those properties is the low density of states that is linearly proportional to energy at the K point in the reciprocal lattice. This linearity results in having zero states at the Dirac point. Consequently graphene has a low quantum capacitance that reaches absolute minimum at the Dirac point. Graphene quantum capacitance is a powerful tool to understand the electrical properties of graphene. We have utilized this tool to understand the quality of graphene, and to probe its interface with its surroundings. The quantum capacitance can be observed in MOG structure that acts as a variable capacitor (varactor). As was demonstrated in chapters 3 and 4, the non-idealities in the varactor device are associated with the inherent disorder in the graphene, defects and breakage from the transfer process, and the gate dielectric defects. In order for the varactors to function efficiently as a sensor four criteria must be met: First, graphene surface must be completely exposed to the agent; therefore the inverted geometry (buried gate) is a necessity. Second, the effective dielectric constant has to be small (EOT<4nm) to obtain an acceptable capacitance tuning. Third, there is maximum limit for the disorder ($T_0$ or $\sigma$) in graphene. This level has a maximum limit in order to obtain an acceptable

C-V curve. Figure 7-1 shows the effect of increasing the disorder in terms of random voltage fluctuation that smears the C-V curve around the Dirac point. It is important to notice that once the random potential fluctuation is >100meV, the C-V curve losses its tuning. Therefore the capacitance tuning dramatically drops as in Figure 7-1(b). The sensor level of sensitivity depends on the capacitance tuning. Therefore a sensor with ($\sigma$ > 200meV) will not be adequate for sensing applications [1],[2]. Fourth, a successful wireless sensor should have a high quality factor (>10) at the target resonant frequency. The current devices have not met this criterion due to high resistance, which is likely a result of breakage and tears in the graphene sheet, particularly at the gate edge. Achieving a continuous sheet with minimum defects is important to reduce the resistance of the LRC circuit. The multi-finger geometry also helps in reducing the resistance of the device.

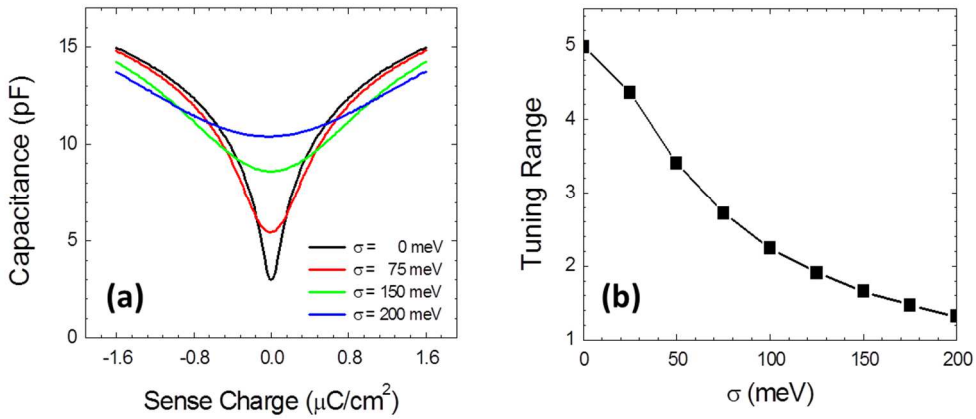


Figure 7-1: The effect of disorder on the capacitance measurements (a) capacitance versus sensing charge at various level of disorder. (b) Tuning range versus random potential fluctuation.

The area efficiency is another concern, since reducing the total area leads to smaller total capacitance. In addition, the small total capacitance will lower the resonant frequency, which leads to a shorter distance between the sensor and the read out device. The defects

and vacancies in the oxide were shown to have an impact on four varactor characteristics: Dirac point, the distance between the graphene and oxide, frequency dispersion, and finally the hysteresis. Though for wireless application both the frequency dispersion and the hysteresis do not have a direct impact on the device characteristic, they are a consequence of traps which affect other important aspects of the device performance such as the Dirac point.

### 7.1.2 Wireless vapor sensors

The revolutionary concept of wireless graphene varactor sensors that was presented theoretically in [23], was the motivation behind studying graphene varactors. This device utilizes the quantum capacitance effect in graphene to realize an ultra-small passive wireless sensor. There are several stages in order to realize this revolutionary concept. First, fabricating CVD graphene varactor in local back gated multi-finger geometry was achieved. Second, measuring the devices electrical characterization, and presenting for the first time the quantum capacitance in such a configuration. The operation of a graphene quantum capacitance varactor devices show capacitance modulation up to 45% over a bias range of 2V. Temperature-dependent measurements and theoretical fitting reveal performance close to the expectations. The device non-idealities that hindered the device performance from reaching the theoretical limit were explored in fair depth. The disorder in graphene was quantitatively modeled with two different but equivalent models. Understanding the effect of the disorder on the device performance is crucial for future applications. Furthermore, the graphene interface with the $HfO_2$ was investigated and our findings determined experimentally the existence of a gap between the graphene and $HfO_2$. The gap thickness depends for the most part on the number of oxygen vacancies in the $HfO_2$. The oxygen vacancies play an important role in the device electrical characterization. In addition to affecting the gap size, they also dope the graphene n-type. Our characterization methodology has investigated both MOG and

MIM devices at a wide range of frequencies (5-500 kHz) and Temperatures (4.2-300 K). Those studies provided us with rich data that reveals different sides of the devices. The frequency measurements allowed us to study the border traps. The temperature study on the other hand provided us with a different set of data. The temperature dependence data helped in improving the fitting procedure and emphasized the difference in the frequency dispersion between the MOG and MIM devices.

Our experimental result was the beginning to the realization of a vapor wireless sensor. All along the previous chapters the goal was to build a fundamental understating of the device operation and its limitations in order to realize a device for in vivo biosensing. The advantages of graphene quantum capacitance wireless sensors include: excellent noise immunity because the analyte concentration is encoded as the resonant frequency of the passive oscillator circuit, thus it is immune to many of the noise sources; and improved size scalability compared to alternative passive sensing approaches. Our results suggest that graphene quantum capacitance wireless sensors can enable a powerful platform for detection of a wide range of chemical and biological targets [49]. The general device concept for any analyte is depicted in Figure 7-2.

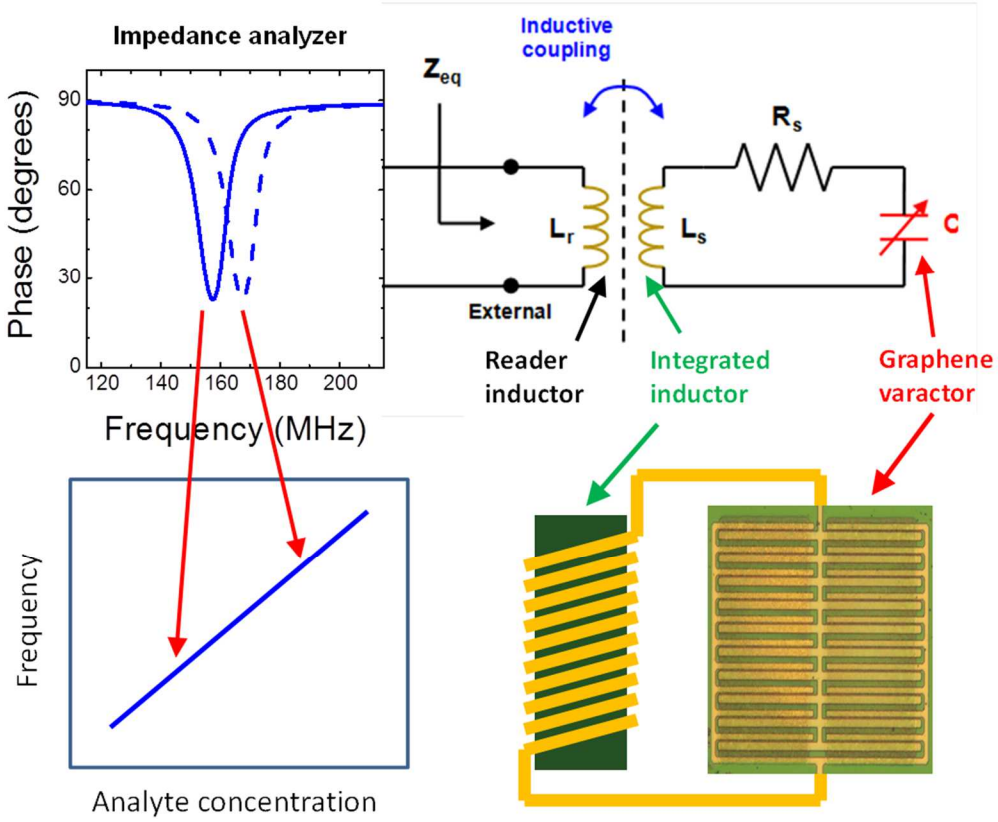


Figure 7-2: Schematic diagram shows the basic concept of t the graphene based wireless sensor.

### 7.1.3 Glucose sensors

Recent studies in diabetes research have shown that real-time monitoring of blood glucose allows for improved controlling of its level, especially if combined with an artificial pancreas device [142]. Unfortunately, current real-time glucose monitoring systems are mainly restricted to subcutaneous, wired devices, thereby preventing long-term usage and displaying slow response time [113]. One of the ultimate goals of this work is to utilize graphene quantum capacitance varactors to produce continuous wireless glucose monitors. As was presented in chapter 5, the sensor can be functionalized by non-covalent attachment of glucose oxidase enzymes to the graphene surface [78]. Glucose

oxidase consumes glucose and oxygen to produce gluconic acid and hydrogen peroxide under physiological conditions. Graphene-based field effect transistors have previously been shown to respond to changes in hydrogen peroxide concentration [115], [116]. In chapter 5 the detection of the immobilized glucose oxidase was confirmed by atomic force microscopy and chemiluminescence of the produced hydrogen peroxide, and the effect of this functionalization scheme on the capacitance measurements was discussed in detail. The sensing side of the experiment, however, was not presented. In chapter 5, only the GOx enzyme based functionalization was discussed. As was described before the glucose sensing with GOx were explained by GFET elsewhere in which it is a resistive based device [115], [116]. However based on our own investigation the sensing is irreversible and can't be used more than once. The exact mechanism of sensing the $H_2O_2$ with graphene is still not fully understood and there is a chance that the $H_2O_2$ does damage the graphene by oxidizing it. $H_2O_2$ is known for being a strong oxidizer and the graphene sheet has many edges and tears, where reactive bonds can be oxidized easily at room temperature. Therefore different functionalization schemes should be further explored to realize a graphene based glucose sensor.

## 7.2 Future outlook

The fundamental work which was presented in this thesis can be considered a building block for future work on graphene sensors. There is still room for improvement and many challenges still need to be overcome. For instance, the area efficiency of the varactor fabrication process is still relatively poor. This problem is likely associated with the non-optimized planarization process for the buried gate, which can cause the graphene to break at the gate edge. This yield could be improved by applying processes such as chemical mechanical polishing (CMP) to more uniformly create a planar buried gate structure. The quality factor should also improve using CMP, as the breaks in the graphene can increase the series resistance. Improving the graphene growth to obtain larger crystal domains could help to minimize disorder and improve the varactors tuning range. Other challenges are related to the characterization techniques, starting with applying different measurement setups to further investigate the border traps. Border traps are spatially distributed in energy. Therefore transient charge pumping measurements could reveal the energy level and the time constant associated with those traps. This will provide a better estimate of their density. Furthermore, the frequency dependence on temperature that was observed only in the MOG devices was speculated to be related to the gap between the graphene and $HfO_2$. The nature of this dependence, however, is still unknown. One suggested experiment is to study the frequency dependence in different controlled environments, such as different levels of humidity or other vapors. Since the gap could be infiltrated by different molecules, then different frequency dispersion is expected at different species. Finally, the disorder model has several free fitting parameters, which has given an adequate picture of the relative trends. A more sophisticated model with less free fitting parameters can lead to more accurate results.

# Bibliography

[1] P. Wallace, “The band theory of graphite,” *Phys. Rev.*, vol. 71, no. 9, pp. 622–634, May 1947.

[2] a K. Geim and K. S. Novoselov, “The rise of graphene.,” *Nat. Mater.*, vol. 6, no. 3, pp. 183–91, Mar. 2007.

[3] A. H. . Castro Neto, N. M. R. . Peres, K. S. . Novoselov, and A. K. . Geim, “The electronic properties of graphene,” *Rev. Mod. Phys.*, vol. 81, no. 1, pp. 109–162, Jan. 2009.

[4] K. S. Novoselov, A. K. Geim, S. V Morozov, D. Jiang, Y. Zhang, S. V Dubonos, I. V Grigorieva, and A. A. Firsov, “Electric field effect in atomically thin carbon films.,” *Science*, vol. 306, no. 5696, pp. 666–9, Oct. 2004.

[5] Y. Hancock, “The 2010 Nobel Prize in physics—ground-breaking experiments on graphene,” *J. Phys. D. Appl. Phys.*, vol. 44, no. 47, p. 473001, Nov. 2011.

[6] Q. Peng, J. Crean, A. K. Dearden, C. Huang, X. Wen, S. P. a. Bordas, and S. De, “Defect Engineering of 2D Monatomic-Layer Materials,” *Mod. Phys. Lett. B*, vol. 27, no. 23, p. 1330017, Sep. 2013.

[7] D. Berdebes, T. Low, Y. Sui, J. Appenzeller, and M. S. Lundstrom, “Substrate Gating of Contact Resistance in Graphene Transistors,” *IEEE Trans. Electron Devices*, vol. 58, no. 11, pp. 3925–3932, Nov. 2011.

[8] S. Reich, J. Maultzsch, C. Thomsen, and P. Ordejón, “Tight-binding description of graphene,” *Phys. Rev. B*, vol. 66, no. 3, p. 035412, Jul. 2002.

[9] K. S. Novoselov, a K. Geim, S. V Morozov, D. Jiang, M. I. Katsnelson, I. V Grigorieva, S. V Dubonos, and a a Firsov, “Two-dimensional gas of massless Dirac fermions in graphene.,” *Nature*, vol. 438, no. 7065, pp. 197–200, Nov. 2005.

[10] L. Britnell, R. Gorbachev, R. Jalil, and B. Belle, “Field-effect tunneling transistor based on vertical graphene heterostructures,” *Science (80-. ).*, vol. 335, no. 6071, pp. 947–50, Feb. 2012.

[11] T. Fang, A. Konar, H. Xing, and D. Jena, "Carrier statistics and quantum capacitance of graphene sheets and ribbons," *Appl. Phys. Lett.*, vol. 91, no. 9, p. 092109, 2007.

[12] W. Li, X. Chen, L. Wang, Y. He, Z. Wu, Y. Cai, M. Zhang, Y. Wang, Y. Han, R. W. Lortz, Z.-Q. Zhang, P. Sheng, and N. Wang, "Density of states and its local fluctuations determined by capacitance of strongly disordered graphene.," *Sci. Rep.*, vol. 3, p. 1772, Jan. 2013.

[13] S. Dröscher, P. Roulleau, F. Molitor, P. Studerus, C. Stampfer, K. Ensslin, and T. Ihn, "Quantum capacitance and density of states of graphene," *Appl. Phys. Lett.*, vol. 96, no. 15, p. 152104, 2010.

[14] L. A. Ponomarenko, R. Yang, R. V. Gorbachev, P. Blake, A. S. Mayorov, K. S. Novoselov, M. I. Katsnelson, and A. K. Geim, "Density of States and Zero Landau Level Probed through Capacitance of Graphene," *Phys. Rev. Lett.*, vol. 105, no. 13, p. 136801, Sep. 2010.

[15] Y. Hanlumyuang and P. Sharma, "Quantum Capacitance: A Perspective from Physics to Nanoelectronics," *Jom*, vol. 66, no. 4, pp. 660–663, Mar. 2014.

[16] H. Xu, Z. Zhang, and L.-M. Peng, "Measurements and microscopic model of quantum capacitance in graphene," *Appl. Phys. Lett.*, vol. 98, no. 13, p. 133122, 2011.

[17] Z. Chen and J. Appenzeller, "Mobility extraction and quantum capacitance impact in high performance graphene field-effect transistor devices," *2008 IEEE Int. Electron Devices Meet.*, no. L, pp. 1–4, Dec. 2008.

[18] J. L. Xia, F. Chen, J. L. Tedesco, D. K. Gaskill, R. L. Myers-Ward, C. R. Eddy, D. K. Ferry, and N. J. Tao, "The transport and quantum capacitance properties of epitaxial graphene," *Appl. Phys. Lett.*, vol. 96, no. 16, p. 162101, 2010.

[19] J. Xia, F. Chen, J. Li, and N. Tao, "Measurement of the quantum capacitance of graphene.," *Nat. Nanotechnol.*, vol. 4, no. 8, pp. 505–9, Aug. 2009.

[20] F. Giannazzo, S. Sonde, V. Raineri, and E. Rimini, "Screening length and quantum capacitance in graphene by scanning probe microscopy," *Nano Lett.*, vol. 9, pp. 23–29, 2008.

[21] K. Takase, S. Tanabe, S. Sasaki, H. Hibino, and K. Muraki, "Impact of graphene quantum capacitance on transport spectroscopy," *Phys. Rev. B*, vol. 86, no. 16, p. 165435, Oct. 2012.

[22] D. A. Deen, E. J. Olson, M. A. Ebrish, and S. J. Koester, "Graphene-Based Quantum Capacitance Wireless Vapor Sensors," *IEEE Sens. J.*, vol. 14, no. 5, pp. 1459–1466, May 2014.

[23] S. J. Koester, "High quality factor graphene varactors for wireless sensing applications," *Appl. Phys. Lett.*, vol. 99, no. 16, p. 163105, 2011.

[24] J. Xia, F. Chen, J. Li, and N. Tao, "Measurement of the quantum capacitance of graphene.," *Nat. Nanotechnol.*, vol. 4, no. 8, pp. 505–9, Aug. 2009.

[25] L. M. Malard, M. a. Pimenta, G. Dresselhaus, and M. S. Dresselhaus, "Raman spectroscopy in graphene," *Phys. Rep.*, vol. 473, no. 5–6, pp. 51–87, Apr. 2009.

[26] C. Casiraghi, A. Hartschuh, H. Qian, S. Piscanec, C. Georgi, A. Fasoli, K. S. Novoselov, D. M. Basko, and A. C. Ferrari, "Raman spectroscopy of graphene edges.," *Nano Lett.*, vol. 9, no. 4, pp. 1433–41, Apr. 2009.

[27] D. Basko and I. Aleiner, "Interplay of Coulomb and electron-phonon interactions in graphene," *Phys. Rev. B*, vol. 77, no. 4, p. 041409, Jan. 2008.

[28] A. Eckmann, J. Park, H. Yang, D. Elias, A. S. Mayorov, G. Yu, R. Jalil, K. S. Novoselov, R. V. Gorbachev, M. Lazzeri, A. K. Geim, and C. Casiraghi, "Raman Fingerprint of Aligned Graphene/h-BN Superlattices," *Nano Lett.*, vol. 13, no. 11, pp. 5242–5246, Nov. 2013.

[29] A. C. Ferrari, J. C. Meyer, V. Scardaci, C. Casiraghi, M. Lazzeri, F. Mauri, S. Piscanec, D. Jiang, K. S. Novoselov, S. Roth, and a. K. Geim, "Raman Spectrum of Graphene and Graphene Layers," *Phys. Rev. Lett.*, vol. 97, no. 18, p. 187401, Oct. 2006.

[30] K. V. Emtsev, F. Speck, T. Seyller, and L. Ley, "Interaction, growth, and ordering of epitaxial graphene on SiC{0001} surfaces: A comparative photoelectron spectroscopy study," *Phys. Rev. B*, vol. 77, no. 15, p. 155303, Apr. 2008.

[31] P. Mallet, F. Varchon, C. Naud, L. Magaud, C. Berger, and J.-Y. Veuillen, "Electron states of mono- and bilayer graphene on SiC probed by scanning-tunneling microscopy," *Phys. Rev. B*, vol. 76, no. 4, p. 041403, Jul. 2007.

[32] P. W. Sutter, J.-I. Flege, and E. a Sutter, “Epitaxial graphene on ruthenium.,” *Nat. Mater.*, vol. 7, no. 5, pp. 406–11, May 2008.

[33] Q. Yu, J. Lian, S. Siriponglert, H. Li, Y. P. Chen, and S.-S. Pei, “Graphene segregated on Ni surfaces and transferred to insulators,” *Appl. Phys. Lett.*, vol. 93, no. 11, p. 113103, 2008.

[34] X. Li, W. Cai, J. An, S. Kim, J. Nah, D. Yang, R. Piner, A. Velamakanni, I. Jung, E. Tutuc, S. K. Banerjee, L. Colombo, and R. S. Ruoff, “Large-area synthesis of high-quality and uniform graphene films on copper foils.,” *Science*, vol. 324, no. 5932, pp. 1312–4, Jun. 2009.

[35] Z. Luo, Y. Lu, D. W. Singer, M. E. Berck, L. A. Somers, B. R. Goldsmith, and A. T. C. Johnson, “Effect of Substrate Roughness and Feedstock Concentration on Growth of Wafer-Scale Graphene at Atmospheric Pressure,” pp. 1441–1447, 2011.

[36] K. K. Kim, A. Hsu, X. Jia, S. M. Kim, Y. Shi, M. Hofmann, D. Nezich, J. F. Rodriguez-Nieva, M. Dresselhaus, T. Palacios, and J. Kong, “Synthesis of monolayer hexagonal boron nitride on Cu foil using chemical vapor deposition.,” *Nano Lett.*, vol. 12, no. 1, pp. 161–6, Jan. 2012.

[37] H. Zhou, W. J. Yu, L. Liu, R. Cheng, Y. Chen, X. Huang, Y. Liu, Y. Wang, Y. Huang, and X. Duan, “Chemical vapour deposition growth of large single crystals of monolayer and bilayer graphene.,” *Nat. Commun.*, vol. 4, p. 2096, Jan. 2013.

[38] F. Schedin, a K. Geim, S. V Morozov, E. W. Hill, P. Blake, M. I. Katsnelson, and K. S. Novoselov, “Detection of individual gas molecules adsorbed on graphene.,” *Nat. Mater.*, vol. 6, no. 9, pp. 652–5, Sep. 2007.

[39] Y. Dan, Y. Lu, N. J. Kybert, Z. Luo, and a T. C. Johnson, “Intrinsic response of graphene vapor sensors.,” *Nano Lett.*, vol. 9, no. 4, pp. 1472–5, Apr. 2009.

[40] R. Stine, S. P. Mulvaney, J. T. Robinson, C. R. Tamanaha, and P. E. Sheehan, “Fabrication, optimization, and use of graphene field effect sensors.,” *Anal. Chem.*, vol. 85, no. 2, pp. 509–21, Jan. 2013.

[41] R. Pearce, T. Iakimov, M. Andersson, L. Hultman, a. L. Spetz, and R. Yakimova, “Epitaxially grown graphene based gas sensors for ultra sensitive NO2 detection,” *Sensors Actuators B Chem.*, vol. 155, no. 2, pp. 451–455, Jul. 2011.

[42] J. D. Fowler, M. J. Allen, V. C. Tung, Y. Yang, R. B. Kaner, and B. H. Weiller, "Practical chemical sensors from chemically derived graphene.," *ACS Nano*, vol. 3, no. 2, pp. 301–6, Feb. 2009.

[43] G. Yang, C. Lee, J. Kim, F. Ren, and S. J. Pearton, "Flexible graphene-based chemical sensors on paper substrates.," *Phys. Chem. Chem. Phys.*, vol. 15, no. 6, pp. 1798–801, Feb. 2013.

[44] T. Kuila, S. Bose, P. Khanra, A. K. Mishra, N. H. Kim, and J. H. Lee, "Recent advances in graphene-based biosensors.," *Biosens. Bioelectron.*, vol. 26, no. 12, pp. 4637–48, Aug. 2011.

[45] E. W. Hill, A. Vijayaragahvan, and K. Novoselov, "Graphene Sensors," *IEEE Sens. J.*, vol. 11, no. 12, pp. 3161–3170, Dec. 2011.

[46] W. Yuan and G. Shi, "Graphene-based gas sensors," *J. Mater. Chem. A*, vol. 1, no. 35, p. 10078, 2013.

[47] B. Kumar, K. Min, and M. Bashirzadeh, "The role of external defects in chemical sensing of graphene field-effect transistors," *Nano …*, vol. 13, no. 5, pp. 1962–8, May 2013.

[48] M. S. Mannoor, H. Tao, J. D. Clayton, A. Sengupta, D. L. Kaplan, R. R. Naik, N. Verma, F. G. Omenetto, and M. C. McAlpine, "Graphene-based wireless bacteria detection on tooth enamel.," *Nat. Commun.*, vol. 3, p. 763, Jan. 2012.

[49] D. A. Deen, E. J. Olson, M. A. Ebrish, S. Member, S. J. Koester, and S. Member, "Graphene-Based Quantum Capacitance Wireless Vapor Sensors," vol. 14, no. 5, pp. 1459–1466, 2014.

[50] M. A. Ebrish, H. Shao, and S. J. Koester, "Operation of multi-finger graphene quantum capacitance varactors using planarized local bottom gate electrodes," *Appl. Phys. Lett.*, vol. 100, no. 14, p. 143102, 2012.

[51] J. Lee, T. Ha, K. N. Parrish, S. Member, and S. F. Chowdhury, "High-Performance Current Saturating Graphene Field-Effect Transistor With Hexagonal Boron Nitride Dielectric on Flexible Polymeric Substrates," vol. 34, no. 2, pp. 172–174, 2013.

[52] S.-J. Han, D. Reddy, G. D. Carpenter, A. D. Franklin, and K. A. Jenkins, "Current Saturation in Submicrometer Graphene Transistors with Thin Gate Dielectric:

Experiment, Simulation, and Theory," *ACS Nano*, vol. 6, no. 6, pp. 5220–5226, Jun. 2012.

[53] M. Suemitsu, "S1-2 Graphene FETs : Issues and Prospects," pp. 59–62.

[54] C. Shih, Q. H. Wang, Z. Jin, G. L. C. Paulus, D. Blankschtein, P. Jarillo-herrero, and M. S. Strano, "Disorder Imposed Limits of Mono- and Bilayer Graphene Electronic Modi fi cation Using Covalent Chemistry," 2013.

[55] X. Wang, S. M. Tabakman, and H. Dai, "Atomic layer deposition of metal oxides on pristine and functionalized graphene.," *J. Am. Chem. Soc.*, vol. 130, no. 26, pp. 8152–3, Jul. 2008.

[56] H. Xu, Z. Zhang, and L.-M. Peng, "Measurements and microscopic model of quantum capacitance in graphene," *Appl. Phys. Lett.*, vol. 98, no. 13, p. 133122, 2011.

[57] A. Pirkle, R. M. Wallace, and L. Colombo, "In situ studies of $Al_2O_3$ and $HfO_2$ dielectrics on graphite," *Appl. Phys. Lett.*, vol. 95, no. 13, p. 133106, 2009.

[58] H. Kim, P. C. McIntyre, and K. C. Saraswat, "Effects of crystallization on the electrical properties of ultrathin $HfO_2$ dielectrics grown by atomic layer deposition," *Appl. Phys. Lett.*, vol. 82, no. 1, p. 106, 2003.

[59] D. M. Hausmann, E. Kim, J. Becker, and R. G. Gordon, "Atomic Layer Deposition of Hafnium and Zirconium Oxides Using Metal Amide Precursors," *Chem. Mater.*, vol. 14, no. 10, pp. 4350–4358, Oct. 2002.

[60] L. Wang, Z. Chen, C. R. Dean, T. Taniguchi, K. Watanabe, L. E. Brus, and J. Hone, "Negligible environmental sensitivity of graphene in a hexagonal boron nitride/graphene/h-BN sandwich structure.," *ACS Nano*, vol. 6, no. 10, pp. 9314–9, Oct. 2012.

[61] M. Yankowitz, J. Xue, and B. J. LeRoy, "Graphene on hexagonal boron nitride.," *J. Phys. Condens. Matter*, vol. 26, no. 30, p. 303201, Jul. 2014.

[62] J. W. Suk, A. Kitt, C. W. Magnuson, Y. Hao, S. Ahmed, J. An, A. K. Swan, B. B. Goldberg, and R. S. Ruoff, "Transfer of CVD-grown monolayer graphene onto arbitrary substrates.," *ACS Nano*, vol. 5, no. 9, pp. 6916–24, Sep. 2011.

[63] Y. Wang, Y. Zheng, X. Xu, E. Dubuisson, Q. Bao, J. Lu, K. P. Loh, and W. E. T. Al, "Electrochemical Delamination of CVD- Grown Graphene Film : Toward the Recyclable Use of Copper Catalyst," no. 12, pp. 9927–9933, 2011.

[64] J. T. Smith, A. D. Franklin, D. B. Farmer, and C. D. Dimitrakopoulos, "Reducing contact resistance in graphene devices through contact area patterning.," *ACS Nano*, vol. 7, no. 4, pp. 3661–7, Apr. 2013.

[65] F. Xia, V. Perebeinos, Y. Lin, Y. Wu, and P. Avouris, "The origins and limits of metal-graphene junction resistance.," *Nat. Nanotechnol.*, vol. 6, no. 3, pp. 179–84, Mar. 2011.

[66] L. Wang, I. Meric, P. Y. Huang, Q. Gao, Y. Gao, H. Tran, T. Taniguchi, K. Watanabe, L. M. Campos, D. a. Muller, J. Guo, P. Kim, J. Hone, K. L. Shepard, and C. R. Dean, "One-dimensional electrical contact to a two-dimensional material.," *Science*, vol. 342, no. 6158, pp. 614–7, Nov. 2013.

[67] A. Hsu, H. Wang, K. K. Kim, J. Kong, and T. Palacios, "Impact of Graphene Interface Quality on Contact Resistance and RF Device Performance," *IEEE Electron Device Lett.*, vol. 32, no. 8, pp. 1008–1010, Aug. 2011.

[68] E. J. H. Lee, K. Balasubramanian, R. T. Weitz, M. Burghard, and K. Kern, "Contact and edge effects in graphene devices.," *Nat. Nanotechnol.*, vol. 3, no. 8, pp. 486–90, Aug. 2008.

[69] W. Liu, J. Wei, X. Sun, and H. Yu, "A Study on Graphene—Metal Contact," *Crystals*, vol. 3, no. 1, pp. 257–274, Mar. 2013.

[70] W. Li, C. Hacker, and Y. Liang, "Highly reproducible metal/graphene contacts and stable electrical performance by UV-Ozone treatment," *arXiv Prepr. arXiv …*, Mar. 2013.

[71] A. Pirkle, J. Chan, a. Venugopal, D. Hinojos, C. W. Magnuson, S. McDonnell, L. Colombo, E. M. Vogel, R. S. Ruoff, and R. M. Wallace, "The effect of chemical residues on the physical and electrical properties of chemical vapor deposited graphene transferred to SiO2," *Appl. Phys. Lett.*, vol. 99, no. 12, p. 122108, 2011.

[72] J. D. Jones, K. K. Mahajan, W. H. Williams, P. a. Ecton, Y. Mo, and J. M. Perez, "Formation of graphane and partially hydrogenated graphene by electron irradiation of adsorbates on graphene," *Carbon N. Y.*, vol. 48, no. 8, pp. 2335–2340, Jul. 2010.

[73] J. Martin, N. Akerman, G. Ulbricht, T. Lohmann, J. H. Smet, K. von Klitzing, and a. Yacoby, "Observation of electron–hole puddles in graphene using a scanning single-electron transistor," *Nat. Phys.*, vol. 4, no. 2, pp. 144–148, Nov. 2007.

[74] B. Hu, E. Hwang, and S. Das Sarma, "Density of states of disordered graphene," *Phys. Rev. B*, vol. 78, no. 16, p. 165411, Oct. 2008.

[75] K. I. Bolotin, K. J. Sikes, J. Hone, H. L. Stormer, and P. Kim, "Temperature-Dependent Transport in Suspended Graphene," *Phys. Rev. Lett.*, vol. 101, no. 9, p. 096802, Aug. 2008.

[76] W. Cai, A. L. Moore, Y. Zhu, X. Li, S. Chen, L. Shi, and R. S. Ruoff, "Thermal transport in suspended and supported monolayer graphene grown by chemical vapor deposition.," *Nano Lett.*, vol. 10, no. 5, pp. 1645–51, May 2010.

[77] M. A. Ebrish and S. J. Koester, "Dielectric thickness dependence of quantum capacitance in graphene varactors with local metal back gates," in *70th Device Research Conference*, 2012, pp. 105–106.

[78] M. A. Ebrish, E. J. Olson, and S. J. Koester, "Effect of noncovalent basal plane functionalization on the quantum capacitance in graphene.," *ACS Appl. Mater. Interfaces*, vol. 6, no. 13, pp. 10296–303, Jul. 2014.

[79] A. Nag, K. Raidongia, K. P. S. S. Hembram, R. Datta, U. V Waghmare, and C. N. R. Rao, "Graphene analogues of BN: novel synthesis and properties.," *ACS Nano*, vol. 4, no. 3, pp. 1539–44, Mar. 2010.

[80] K. K. Kim, A. Hsu, X. Jia, S. M. Kim, Y. Shi, M. Dresselhaus, T. Palacios, and J. Kong, "Synthesis and characterization of hexagonal boron nitride film as a dielectric layer for graphene devices.," *ACS Nano*, vol. 6, no. 10, pp. 8583–90, Oct. 2012.

[81] H. Xu, J. Wu, Y. Chen, H. Zhang, and J. Zhang, "Substrate Engineering by Hexagonal Boron Nitride/$SiO_2$ for Hysteresis-Free Graphene FETs and Large-Scale Graphene p-n Junctions.," *Chem. Asian J.*, vol. 8, no. 10, pp. 2446–52, Oct. 2013.

[82] C. H. Lui, L. Liu, K. F. Mak, G. W. Flynn, and T. F. Heinz, "Ultraflat graphene.," *Nature*, vol. 462, no. 7271, pp. 339–41, Nov. 2009.

[83] B. Dóra, K. Ziegler, and P. Thalmeier, "Effect of weak disorder on the density of states in graphene," *Phys. Rev. B*, vol. 77, no. 11, p. 115422, Mar. 2008.

[84] K. Ziegler, B. Dóra, and P. Thalmeier, "Density of states in disordered graphene," *Phys. Rev. B*, vol. 79, no. 23, p. 235431, Jun. 2009.

[85] A. C. Ferrari and D. M. Basko, "Raman spectroscopy as a versatile tool for studying the properties of graphene.," *Nat. Nanotechnol.*, vol. 8, no. 4, pp. 235–46, Apr. 2013.

[86] M. Ishigami, J. Chen, and W. Cullen, "Atomic structure of graphene on $SiO_2$," *Nano …*, vol. 7, no. 6, pp. 1643–8, Jun. 2007.

[87] W. L. Scopel, a. Fazzio, R. H. Miwa, and T. M. Schmidt, "Graphene on amorphous $HfO_2$ surface: An ab initio investigation," *Phys. Rev. B*, vol. 87, no. 16, p. 165307, Apr. 2013.

[88] V. Galitski, S. Adam, and S. Das Sarma, "Statistics of random voltage fluctuations and the low-density residual conductivity of graphene," *Phys. Rev. B*, vol. 76, no. 24, p. 245405, Dec. 2007.

[89] C. S. Lai, W. C. Wu, K. M. Fan, J. C. Wang, and S. J. Lin, "Effects of Post CF 4 Plasma Treatment on the HfO 2 Thin Film," *Jpn. J. Appl. Phys.*, vol. 44, no. 4B, pp. 2307–2310, Apr. 2005.

[90] D. Estrada, S. Dutta, A. Liao, and E. Pop, "Reduction of hysteresis for carbon nanotube mobility measurements using pulsed characterization.," *Nanotechnology*, vol. 21, no. 8, p. 85702, Feb. 2010.

[91] H. J. Oh, A. B. Sumarlina, and S. Lee, "High-k Integration and Interface Engineering for III-V MOSFETs," in *ECS Transactions*, 2011, vol. 35, no. 4, pp. 481–495.

[92] R. V. Galatage, D. M. Zhernokletov, H. Dong, B. Brennan, C. L. Hinkle, R. M. Wallace, and E. M. Vogel, "Accumulation capacitance frequency dispersion of III-V metal-insulator-semiconductor devices due to disorder induced gap states," *J. Appl. Phys.*, vol. 116, no. 1, p. 014504, Jul. 2014.

[93] V. Chobpattana, J. Son, J. J. M. Law, R. Engel-Herbert, C.-Y. Huang, and S. Stemmer, "Nitrogen-passivated dielectric/InGaAs interfaces with sub-nm

equivalent oxide thickness and low interface trap densities," *Appl. Phys. Lett.*, vol. 102, no. 2, p. 022907, 2013.

[94] G. Jiao, C. Yao, Y. Xuan, D. Huang, P. D. Ye, and M. Li, "Experimental Investigation of Border Trap Generation in InGaAs nMOSFETs With Gate Dielectric Under PBTI Stress," *IEEE Trans. Electron Devices*, vol. 59, no. 6, pp. 1661–1667, 2012.

[95] Y. J. Wei-Hao Wu, Bing-Yue Tsui, Mao-Chieh Chen, Yong-Tian Hou and and M.-S. L. Hun-Jan Tao, Shih-Chang Chen, "Transient Charging and Discharging Behaviors of Border Traps in the Dual-Layer $HfO_2/SiO_2$ High-κ Gate Stack Observed by Using Low-Frequency Charge Pumping Method," *IEEE Trans. Electron Devices*, vol. 54, no. 6, pp. 1330–1337, Jun. 2007.

[96] G. Brammertz, A. Alian, D. H. Lin, M. Meuris, M. Caymax, and W.-E. Wang, "A Combined Interface and Border Trap Model for High-Mobility Substrate Metal–Oxide–Semiconductor Devices Applied to and InP Capacitors.," *IEEE Trans. Electron Devices*, vol. 58, no. 11, pp. 3890–3897, Nov. 2011.

[97] E. Cartier, M. Hopstaken, and M. Copel, "Oxygen passivation of vacancy defects in metal-nitride gated $HfO_2/SiO_2$/Si devices," *Appl. Phys. Lett.*, vol. 95, no. 4, p. 042901, 2009.

[98] H. Madan, M. J. Hollander, J. A. Robinson, and S. Datta, "Extraction of near interface trap density in top gated graphene transistor using high frequency current voltage characteristics," in *70th Device Research Conference*, 2012, pp. 181–182.

[99] R. Engel-Herbert, Y. Hwang, and S. Stemmer, "Comparison of methods to quantify interface trap densities at dielectric/III-V semiconductor interfaces," *J. Appl. Phys.*, vol. 108, no. 12, p. 124101, Dec. 2010.

[100] G. Zebrev, E. Melnik, and A. Tselykovskiy, "Interface traps in graphene field effect devices: extraction methods and influence on characteristics," *arXiv Prepr. arXiv1405.5766*, pp. 1–45, 2014.

[101] F. Heiman and G. Warfield, "The effects of oxide traps on the MOS capacitance," *IEEE Trans. Electron Devices*, vol. 12, no. 4, pp. 167–178, Apr. 1965.

[102] D. K. Schroder and L. G. Rubin, "Semiconductor Material and Device Characterization," *Phys. Today*, vol. 44, no. 4, p. 107, 1991.

[103] S. M. Sze and K. K. Ng, *Physics of Semiconductor Devices*. Hoboken, NJ, USA: John Wiley & Sons, Inc., 2006.

[104] W.-H. Wu, B.-Y. Tsui, M.-C. Chen, Y.-T. Hou, Y. Jin, H.-J. Tao, S.-C. Chen, and M.-S. Liang, "Spatial and energetic distribution of border traps in the dual-layer $HfO_2/SiO_2$ high-k gate stack by low-frequency capacitance-voltage measurement," *Appl. Phys. Lett.*, vol. 89, no. 16, p. 162911, 2006.

[105] D. Heh, C. D. Young, G. a. Brown, P. Y. Hung, A. Diebold, G. Bersuker, E. M. Vogel, and J. B. Bernstein, "Spatial distributions of trapping centers in $HfO_2/SiO_2$ gate stacks," *Appl. Phys. Lett.*, vol. 88, no. 15, p. 152907, 2006.

[106] Y. Yuan, L. Wang, B. Yu, B. Shin, J. Ahn, P. C. McIntyre, P. M. Asbeck, M. J. W. Rodwell, and Y. Taur, "A Distributed Model for Border Traps in $Al_2O_3$ −InGaAs MOS Devices," *IEEE Electron Device Lett.*, vol. 32, no. 4, pp. 485–487, Apr. 2011.

[107] M. A. Ebrish, D. A. Deen, and S. J. Koester, "Border trap characterization in metal-oxide-graphene capacitors with HfO2 dielectrics," in *71st Device Research Conference*, 2013, pp. 37–38.

[108] E. J. Olson, R. Ma, T. Sun, M. A. Ebrish, N. Haratipour, K. Min, N. R. Aluru, and S. J. Koester. "Capacitive Sensing of Intercalated Molecules Using Graphene," *Submitted*, 2015.

[109] S. Mosfets, D. Maji, S. P. Duttagupta, V. R. Rao, S. Member, C. C. Yeo, B. Cho, and A. D. Fabrication, "Border-Trap Characterization in High- κ," *Electronic Device letters* , vol. 28, no. 8, pp. 731–733, 2007.

[110] K. Xiong, J. Robertson, M. C. Gibson, and S. J. Clark, "Defect energy levels in HfO 2 high-dielectric-constant gate oxide," vol. 183505, pp. 10–13, 2005.

[111] W. J. Maeng and H. Kim, "Electrical Properties of Atomic Layer Deposition $HfO_2$ and $HfO_x$ $N_y$ on Si Substrates with Various Crystal Orientations," *J. Electrochem. Soc.*, vol. 155, no. 4, p. H267, 2008.

[112] X. Chen, L. Wang, W. Li, Y. Wang, Z. Wu, M. Zhang, Y. Han, Y. He, and N. Wang, "Electron-electron interactions in monolayer graphene quantum capacitors," *Nano Res.*, vol. 6, no. 8, pp. 619–626, Jun. 2013.

[113] E. Olson, D. Deen, M. Ebrish, and A. Basu, "Wireless Graphene-Based Quantum Capacitance Sensors for Continuous Glucose Monitoring," in *nsti.org*.

[114] L. Yan, Y. B. Zheng, F. Zhao, S. Li, X. Gao, B. Xu, P. S. Weiss, and Y. Zhao, "Chemistry and physics of a single atomic layer: strategies and challenges for functionalization of graphene and graphene-based materials.," *Chem. Soc. Rev.*, vol. 41, no. 1, pp. 97–114, Jan. 2012.

[115] Y. Huang, X. Dong, Y. Shi, C. M. Li, L.-J. Li, and P. Chen, "Nanoelectronic biosensors based on CVD grown graphene.," *Nanoscale*, vol. 2, no. 8, pp. 1485–8, Aug. 2010.

[116] Y. H. Kwak, D. S. Choi, Y. N. Kim, H. Kim, D. H. Yoon, S.-S. Ahn, J.-W. Yang, W. S. Yang, and S. Seo, "Flexible glucose sensor using CVD-grown graphene-based field effect transistor.," *Biosens. Bioelectron.*, vol. 37, no. 1, pp. 82–7, 2012.

[117] A. Bonanni, A. Ambrosi, and M. Pumera, "Nucleic acid functionalized graphene for biosensing.," *Chemistry*, vol. 18, no. 6, pp. 1668–73, Feb. 2012.

[118] D. T. Bostick and D. M. Hercules, "Quantitative Determination of Blood Glucose Using Enzyme induced Chemiluminescence of Luminsl," vol. 479, no. 3, pp. 447–452, 1975.

[119] S. Libertino, V. Aiello, A. Scandurra, M. Renis, and F. Sinatra, "Immobilization of the Enzyme Glucose Oxidase on Both Bulk and Porous $SiO_2$ Surfaces," *Sensors*, vol. 8, no. 9, pp. 5637–5648, Sep. 2008.

[120] T. Kuila, S. Bose, A. K. Mishra, P. Khanra, N. H. Kim, and J. H. Lee, "Chemical functionalization of graphene and its applications," *Prog. Mater. Sci.*, vol. 57, no. 7, pp. 1061–1105, Sep. 2012.

[121] M. J. Lee, J. S. Choi, J.-S. Kim, I.-S. Byun, D. H. Lee, S. Ryu, C. Lee, and B. H. Park, "Characteristics and effects of diffused water between graphene and a $SiO_2$ substrate," *Nano Res.*, vol. 5, no. 10, pp. 710–717, Sep. 2012.

[122] K. Xu, P. Cao, and J. R. Heath, "Graphene visualizes the first water adlayers on mica at ambient conditions.," *Science*, vol. 329, no. 5996, pp. 1188–91, Sep. 2010.

[123] S. V Ushakov and A. Navrotsky, "Direct measurements of water adsorption enthalpy on hafnia and zirconia Direct measurements of water adsorption enthalpy on hafnia and zirconia," vol. 164103, no. 2005, pp. 2012–2015, 2014.

[124] X. Du, I. Skachko, A. Barker, and E. Y. Andrei, "Approaching ballistic transport in suspended graphene.," *Nat. Nanotechnol.*, vol. 3, no. 8, pp. 491–5, Aug. 2008.

[125] B. Fallahazad, S. Kim, L. Colombo, and E. Tutuc, "Dielectric thickness dependence of carrier mobility in graphene with $HfO_2$ top dielectric," *Appl. Phys. Lett.*, vol. 97, no. 12, p. 123105, 2010.

[126] C. Jang, S. Adam, J.-H. Chen, E. D. Williams, S. Das Sarma, and M. S. Fuhrer, "Tuning the Effective Fine Structure Constant in Graphene: Opposing Effects of Dielectric Screening on Short- and Long-Range Potential Scattering," *Phys. Rev. Lett.*, vol. 101, no. 14, p. 146805, Oct. 2008.

[127] T. Ha, J. Lee, S. Member, and D. A. Member, "The Restorative Effect of Fluoropolymer Coating on Electrical Characteristics of Graphene Field-Effect Transistors," vol. 34, no. 4, pp. 559–561, 2013.

[128] D. a Cherepanov, B. a Feniouk, W. Junge, and A. Y. Mulkidjanian, "Low dielectric permittivity of water at the membrane interface: effect on the energy coupling mechanism in biological membranes.," *Biophys. J.*, vol. 85, no. 2, pp. 1307–16, Aug. 2003.

[129] A. Veligura, P. J. Zomer, I. J. Vera-Marun, C. Józsa, P. I. Gordiichuk, and B. J. van Wees, "Relating hysteresis and electrochemistry in graphene field effect transistors," *J. Appl. Phys.*, vol. 110, no. 11, p. 113708, 2011.

[130] M. Lafkioti, B. Krauss, T. Lohmann, U. Zschieschang, H. Klauk, K. V Klitzing, and J. H. Smet, "Graphene on a hydrophobic substrate: doping reduction and hysteresis suppression under ambient conditions.," *Nano Lett.*, vol. 10, no. 4, pp. 1149–53, Apr. 2010.

[131] B. Rezania, M. Dorn, N. Severin, and J. P. Rabe, "Influence of graphene exfoliation on the properties of water-containing adlayers visualized by graphenes and scanning force microscopy.," *J. Colloid Interface Sci.*, vol. 407, pp. 500–4, Oct. 2013.

[132] H. Guang, M. Aoki, S. Tanaka, and M. Kohyama, "Hole doping by adsorption of oxygen on a Stone–Thrower–Wales defect in graphene," *Solid State Commun.*, vol. 174, pp. 10–15, Nov. 2013.

[133] R. K. Joshi, H. Gomez, F. Alvi, and A. Kumar, "Graphene Films and Ribbons for Sensing of $O_2$ , and 100 ppm of CO and $NO_2$ in Practical Conditions," *J. Phys. Chem. C*, vol. 114, no. 14, pp. 6610–6613, Apr. 2010.

[134] R. Nopper, R. Niekrawietz, and L. Reindl, "Wireless Readout of Passive LC Sensors," *IEEE Trans. Instrum. Meas.*, vol. 59, no. 9, pp. 2450–2457, Sep. 2010.

[135] K. Xu, P. Cao, and J. R. Heath, "Graphene visualizes the first water adlayers on mica at ambient conditions.," *Science*, vol. 329, no. 5996, pp. 1188–91, Sep. 2010.

[136] C. G. Low, Q. Zhang, Y. Hao, and R. S. Ruoff, "Graphene Field Effect Transistors with Mica as Gate Dielectric Layers.," *Small*, pp. 1–6, Jul. 2014.

[137] M. Rinkiö, M. Y. Zavodchikova, P. Törmä, and A. Johansson, "Effect of humidity on the hysteresis of single walled carbon nanotube field-effect transistors," *Phys. Status Solidi*, vol. 245, no. 10, pp. 2315–2318, Oct. 2008.

[138] J. Shim, C. H. Lui, T. Y. Ko, Y.-J. Yu, P. Kim, T. F. Heinz, and S. Ryu, "Water-gated charge doping of graphene induced by mica substrates.," *Nano Lett.*, vol. 12, no. 2, pp. 648–54, Feb. 2012.

[139] C. H. Lui, L. Liu, K. F. Mak, G. W. Flynn, and T. F. Heinz, "Ultraflat graphene.," *Nature*, vol. 462, no. 7271, pp. 339–341, 2009.

[140] S. Ryu, L. Liu, S. Berciaud, Y.-J. Yu, H. Liu, P. Kim, G. W. Flynn, and L. E. Brus, "Atmospheric oxygen binding and hole doping in deformed graphene on a $SiO_2$ substrate.," *Nano Lett.*, vol. 10, no. 12, pp. 4944–51, Dec. 2010.

[141] S. J. Koester, "Graphene Quantum Capacitance Varactors for Wireless Sensing Applications," no. 612, pp. 2010–2011, 2011.

[142] D. Elleri, J. M. Allen, K. Kumareswaran, L. Leelarathna, M. Nodale, K. Caldwell, P. Cheng, C. Kollman, A. Haidar, H. R. Murphy, M. E. Wilinska, C. L. Acerini, D. B. Dunger, and R. Hovorka, "Closed-loop basal insulin delivery over 36 hours in adolescents with type 1 diabetes: randomized clinical trial.," *Diabetes Care*, vol. 36, no. 4, pp. 838–44, Apr. 2013.

# Appendix A:

# Fabrication Methods and Recipes

This appendix outlines fabrication processing detailed, procedures, and recipes. Varactors fabrication steps for $Si/SiO_2$ substrates are listed from the bottom-up as:

### *Gate Level*

1. Solvent clean: Acetone, Methanol, IPA, DI $H_2O$, and blow dry.
2. Dehydration bake at 120 ºC on hotplate for 1 min.
3. Spin on s1813 at 4500RPM for 45 seconds.
4. Soft bake on hotplate at 105 C for 1 minute.
5. Align the sample to the appropriate (Gate-level-mask) and expose for 5 sec.
6. Bake in Ammonia image reversal oven for the designated time (1.5 hour process).
7. Flood expose under the Oriel for 4 minutes, rotate 90º, and expose for an additional 4 minutes.
8. Develop in 351 developer (351:DI $H_2O$, 1:5) for 3.5 minutes.
9. $O_2$ descum in STS RIE (recipe: \O2clean.set") for 45 seconds.
10. Recess etches in STS RIE ( Typ-Test program for 70 Sec ), then dip in BOE for 20 seconds ($SiO_2$ etch rate in BOE is 50 nm/min).

### *Metal Deposition/Lift-off:*

1. Load sample into e-beam evaporator and deposit: Ti/Pd (10/40 nm).
2. Lift off gate-metal by soaking the sample in Acetone for 15 minutes.
3. Sonication the sample in Acetone again for additional 15 minutes.
4. Clean with Methanol, IPA, DI $H_2O$, and $N_2$ blow dry.

### *Gate Oxide Deposition:*

1. Solvent clean: Acetone, Methanol, IPA, DI $H_2O$, and blow dry.
2. Dehydration bake at 120 ºC on hotplate for 1 min.
3. Deposit gate dielectric at the ALD system under 300 ºC for the desired thickness.
4. Anneal the sample in RTA (recipe: $HfO_2$ anneal) for 5 minutes, in Ar.

### *Via Level (This step is applied only for the sensor mask-design):*

1. Solvent clean: Acetone, Methanol, IPA, DI $H_2O$, and blow dry.
2. Dehydration bake at 120 ºC on hotplate for 1 min.
3. Spin on s1813 at 4000 RPM for 30 minute.
4. Soft bake on hotplate at 105_C for 1 minute.
5. Align sample (Via-level-mask) and expose for 5 sec.
6. Bake in Ammonia image reversal oven for the designated time (1.5 hour process).
7. Flood expose under the Oriel for 4 minutes, rotate 90º, and expose for an additional 4 minutes.
8. Develop in 351 developer (351:DI $H_2O$, 1:5) for 3.5 minutes.

9. $O_2$ descum in STS RIE (recipe: $O_2$clean.set) for 30 seconds.
10. Etch in STS for appropriate time ($HfO_2$ etch rate in SF6 - 14 nm/min by recipe $HfO_2$ etch.set") in STS RIE.
11. Solvent clean: Acetone, Methanol, IPA, DI $H_2O$, and $N_2$ blow dry.

### *Graphene Transfer*

The following process pertains to the CVD-grown graphene on Cu foil.

1. Spin on PMMA 495 A4 at 1500 RPM for 1 minute.
2. Bake at 180 ºC for 2 minutes.
3. Etch bottom side in the STS RIE for 20 sec to remove graphene.
4. Float sample (graphene faced up) on Ammonium per sulfate (at least 3 hours).
5. Transfer graphene to oat on DI $H_2O$ for 10 minutes.
6. Transfer graphene to oat on fresh DI $H_2O$ for 10 - 15 minutes.
7. Transfer graphene onto substrate and [delicately] blow dry with $N_2$.
8. Hot-plate bake at 65ºC for 15-20 minutes or until dry.
9. Spin on PMMA 495 A4 at 1500 RPM for 1 minutes.
10. Bake at 180 ºC for 2 minutes.
11. Submerge in Acetone overnight.
12. Solvent clean: Methanol, IPA, DI $H_2O$, and $N_2$ blow dry.

### *Mesa Level:*

1. Dehydration bake substrate at 120ºC for 1 minute on hotplate.
2. Spin 1813 at 5000 rpm for 30 seconds.
3. Soft-bake substrate at 105ºC for 1 min. on hotplate.
4. Align the sample to the appropriate (Mesa-level-mask) and expose for 5 sec.
5. Develop in 351 developer (351:DI $H_2O$, 1:5) for 30 seconds.

### *Mesa Dry Etch*

1. Load sample in STS etcher.
2. Run the $O_2$clean.set recipe in the STS RIE etcher and etch for 30 seconds.
3. Remove sample from STS and solvent clean in Acetone, Methanol, IPA, DI $H_2O$, and $N_2$ blow dry.

### *Contact-level*

1. Hard bake sample at 120 ºC for 1 minute on hotplate.
2. Spin 1813 on the sample at 4500 rpm for 45 seconds.
3. Soft bake sample at 105ºC for 1 minute on hotplate.
4. Align the sample to the appropriate (Contact-level-mask) and expose for 5 seconds.
5. Load sample on upper shelf in Ammonia oven for image reversal. (90 minute process).
6. UV flood expose sample for 4 minutes under Oriel, rotate 90º and flood expose again for 4 minutes.

7. Develop PR for 3.5 minutes in 351 developer (351 developer: DI $H_2O$ (1:5)).
8. Rinse sample in DI $H_2O$ and $N_2$ blow dry.

### *Pads Level*

9. Solvent clean: Acetone, Methanol, IPA, DI $H_2O$, and blow dry.
10. Dehydration bake at 120ºC on hotplate for 1 minute.
11. Spin on s1813 at 3000 RPM for 30 seconds.
12. Soft bake on hotplate at 105ºC for 1 minute.
13. Align sample (Pads-level-mask) and expose for 5 seconds.
14. Bake in Ammonia image reversal oven for the designated time (1.5 hour process).
15. Flood expose under the Oriel for 4 minutes, rotate 90º, and expose for an additional 4 minutes.
16. Develop in 351 developer (351:DI $H_2O$, 1:5) for 3.5 minutes.
17. $O_2$ clean in STS RIE for 30 seconds.
18. Oxide removal etched in BOE for 15 seconds.

### *Metal Deposition and Lift-off*

1. Load sample into e-beam evaporator and deposit: Ti/Al (10/300 nm).
2. Lift of metal in Acetone for 20 minutes.
3. Clean with Methanol, IPA, DI $H_2O$, and $N_2$ blow dry.

### *The quartz substrate:*

Some of the devices were prepared on quartz substrate instead of $Si/SiO_2$

1. Solvent clean: Acetone, Methanol, IPA, DI $H_2O$, and blow dry.
2. Dehydration bake at 120 ºC on hotplate for 1 min.
3. ALD $Al_2O_3$ is deposited on the quartz wafer at 300 º (262 loops).
4. Spin on s1813 at 4500RPM for 45 seconds.
5. Soft bake on hotplate at 105 ºC for 1 minute.
6. Align sample (Gate-level-mask) and expose for 5 sec.
7. Bake in Ammonia image reversal oven for the designated time (1.5 hour process).
8. Flood expose under the Oriel for 4 minutes, rotate 90º, and expose for an additional 4 minutes.
9. Develop in 351 developer (351:DI $H_2O$, 1:5) for 3.5 minutes.
10. $O_2$ descum in STS RIE (recipe: \O2clean.set") for 45 seconds.
11. The Recess etch in this case is different from the previous recess etch as in here the material is $Al_2O_3$ instead of $SiO_2$. The etching is still a combination of dry and wet etch.
12. Reactive ion etching system (Oxford etcher) for 1 minute at "N-$Al_2O_3$ Etch-low power"), then dip in BOE for 1 minute in BOE. The rest of the process after this point is the same as $Si/SiO_2$ substrate.

# Appendix B:

# GOx functionalization recipe and detection

This appendix outlines the details related to the surface functionalization process and the Chemiluminescence experiment to detect the glucose oxidase on the graphene surface.

### *Materials used:*

Luminol, sodium carbonate, sodium bicarbonate, potassium ferricyanide and glucose oxidase type II (from Aspergillus niger) were purchased from Sigma Aldrich. Glucose was purchased from Alfa Aesar. 1-pyrenebutanoic acid succinimidyl ester (1-PASE) was purchased from AnaSpec, Inc. All materials were used as purchased without further purification.

### *Functionalization procedure*

First, the sample was fully submerged into 5 mL of a solution of 1.93 mg/mL 1-PASE in N,N-dimethylformamide (DMF) for approximately 2 hours. The sample was then rinsed by immersion in DMF, was washed in deionized water and dried under a dry nitrogen. The sample was measured immediately after drying. Second, to attach the glucose oxidase enzyme, the sample was placed in 5mL of 10 mg/mL GOx in pH 10 sodium carbonate buffer and refrigerated at 4 °C over-night (>12hrs). The sample was then rinsed by immersion in deionized water, dried under a stream of nitrogen, and measured. Finally, to deactivate remaining unreacted linker, the sample was immersed in a 0.5 M ethanolamine in a pH 10 sodium carbonate buffer solution for approximately 40 minutes,

rinsed by immersion in deionized water, dried under a stream of nitrogen, and again measured.

### *Determination of GOx viability using Luminol*

This experiment was designed and performed by Eric Olson. In this experiment, ~1 $cm^2$ pieces of graphene were transferred to a $Si/SiO_2$ substrate using the same method as for the electronic devices and functionalized according to the above procedure. The functionalized graphene surface was then incubated in an approximately 2.5 mL aliquot of 5 mM glucose in 1X phosphate buffered saline (PBS) for 1 hour under static conditions. As controls, approximately 5 mg GOx was dissolved directly into a 5 mL aliquot of 5 mM glucose solution in PBS as a positive control and GOx was omitted from the glucose sample for a negative control. The remainder of the procedure was identical. A 1 mL aliquot of the sample fluid was then mixed with an equal volume of a 50 mM pH 10 carbonate buffer containing 2 mM luminol and 5 mM potassium ferricyanide. The emission spectrum of this solution was then immediately measured on a JASCO FP-6200 spectrofluorometer with the excitation shutter closed.